AN EMBEDDED, WIRELESS-ENERGY-HARVESTING PLATFORM (E-WEHP) FOR POWERING SENSORS USING EXISTING, AMBIENT, WIRELESS SIGNALS PRESENT IN THE AIR

A Dissertation
Presented to
The Academic Faculty

by

Rushi Vyas

In Partial Fulfillment
of the Requirements for the Degree
Doctor of Philosophy
in
Electrical and Computer Engineering

School of Electrical and Computer Engineering
Georgia Institute of Technology
August 2014

AN EMBEDDED, WIRELESS-ENERGY-HARVESTING PLATFORM (E-WEHP) FOR POWERING SENSORS USING EXISTING, AMBIENT, WIRELESS SIGNALS PRESENT IN THE AIR

Approved by:

Dr. Manos Tentzeris, Advisor
School of Electrical and Computer Engineering
Georgia Institute of Technology

Dr. Gregory Durgin
School of Electrical and Computer Engineering
Georgia Institute of Technology

Dr. Andrew Peterson
School of Electrical and Computer Engineering
Georgia Institute of Technology

Dr. Shyh-Chiang Shen
School of Electrical and Computer Engineering
Georgia Institute of Technology

Dr. Yang Wang
School of Civil and Environmental Engineering
Georgia Institute of Technology

Dr. Hervé Aubert
Laboratoire d'Analyse et d'Architecture des Systèmes
Centre National de la Recherche Scientifique

Date Approved: May 28, 2014

To my family and friends,

Whose love, blessings and support made this work possible

ACKNOWLEDGEMENTS

It has been a long journey here at Georgia Tech. I came to Tech first as an undergraduate student. Never had I imagined of taking my education all the way to a Ph.D., and here I am. It has been a very enlightening and rewarding journey, which has been enriched by many people here on-campus and beyond.

First, I would like to acknowledge the support and advice from my research advisor, Professor Manos M. Tentzeris. His encouragement and ever-enthusiastic support for trying novel things is what has made this doctorate degree possible, and for which I shall remain grateful.

Special thanks also goes to Professor Yoshihiro Kawahara and Dr. Tohru Asami from University of Tokyo for their active interest and funding support especially related to wireless power.

I want to thank my proposal and defense committee members Dr. Durgin, Dr. Peterson, Dr. Wang, Dr. Shen and Dr. Aubert for shepherding the final Ph.D. process, and for their time and suggestions. I would like to thank all my colleagues and friends from the ATHENA research group in particular Vasileios Lakafosis, Jong-hoon, Li Yang, Amin Rida, Napol Chaisilwattana, Cathy Kruesi, Jo Bito, Jonathan Pan, Scott Travis, and Dr. Ronglin Li for their support and friendship.

Special thanks also goes to Dr. Daniela Staiculescu for her help and advice regarding research and academia. I also want to thank the GEDC crew including Ms. Joi Adams, Ms. DeeDee Bennett, Ms. Lisa Gardner and Ryan for help on the administration side.

On the fabrication and prototyping side, I would like to thank Mr. James Steinberg from the ECE senior design lab and Mr. Kyle French and Mr. Vladimir Bortkevich from the M.E Electronics lab for their generous use of parts and machine tools.

Special thanks also goes to Anu Naik for all her help, understanding and affection during these testing times.

Finally to my parents Jyoti and Janak Vyas and sister Suchita: I shall be ever-grateful for your endless love, understanding and unwavering support. I cannot find any single word to express my deepest gratitude for your love, faith, patience and support.

Table of Contents

LIST OF TABLES

LIST OF FIGURES

LIST OF SYMBOLS AND ABBREVIATIONS

°	degrees
ADS	Advanced Design System
BW	Bandwidth
CPW	Coplanar Waveguide
CPWG	Grounded Coplanar Waveguide
CTE	Coefficient of Thermal Expansion
dB	decibels
dBi	dB isotropic
EM	Electromagnetics
E-WEHP	Embedded, Wireless-Energy-harvesting prototype
ε_r	Dielectric constant
ε_e	Effective dielectric
Gbps	Giga bits per second
GHz	Giga Hertz
LCP	Liquid Crystal Polymer
λ	wavelength (Greek lambda)
LTCC	Low-Temperature co-fired Ceramic
LNA	Low Noise Amplifier
Mbps	Megabits per section
MCU	Microcontroller unit
MHz	Mega hertz

mm	millimeter
μm	micrometer
μF	micro-Farad
NF	Noise Figure
Ω	Ohms
PNA	Power Network Analyzer
PCB	Printed Circuit Board
RF	Radio Frequency
RFID	Radio Frequency Identification
RTSA	Real Time Spectrum Analyzer
SBA	Side Band Antenna
Scope	Oscilloscope
SiGe	Silicon Germanium
SMD	Surface Mount Device
Tx/Rx	Transmit/Receive
TRL	Thru-Reflect-Line
tanδ	loss tangent
TV	Television
U.S	United States
UWB	Ultra Wide band
UHF	Ultra high frequency
VNA	Vector Network Analyzer
VCO	Voltage Controlled Oscillator

WSN	Wireless Sensor Network
WLAN	Wireless Local Area Network

SUMMARY

The objective of this research is to develop an embedded, wireless-energy-harvesting prototype (E-WEHP) that can power on and sustain embedded sensing functions using the power present in ambient wireless signals in urban areas. This research is part of a bigger effort towards greening RF circuits and applications in order to reduce their polluting foot print. Pollution due to modern electronics is primarily caused by non-biodegradable packaging waste and batteries that form a big part of most electronics, and can be a nuisance in RFIDS and wireless sensors that are used in consumer items, buildings, industries, agriculture and transportation. The first part of this research effort addresses the issue of electronic packaging waste by characterizing substrates made out of biodegradable paper and perfluoropolymer (PFA) material for potential use as a dielectric material in RF circuits. Towards this goal, the first of its kind active wireless sensor module made of biodegradable paper substrate using a novel inkjet printing technology is developed.

The second and third part of this research effort addresses the issue of battery waste by investigating the use of ambient solar and wireless waves for powering RF electronics for wireless localization and sensing applications, respectively, without the use of batteries. The second part of this thesis presents a unique solar-powered tag called SOLTAG that combines ambient sunlight along with an RFID-type powering mechanism to implement a very low-cost and battery-less semi-passive-wireless tag but with a much longer range than passive RFID tags. SOLTAG offers a battery-less and a much more economical alternative than conventional GPS receivers for a GPS-like application to track vehicles in a parking lot.

The third and main part of this research work presents another novel way of powering embedded sensors over a range in excess of 6 km using existing wireless infrastructure currently

found in most urban areas without the aid of batteries. An in-depth analysis of the ambient wireless signals present in 2 major urban cities due to digital-TV broadcasts along with an optimized E-WEHP platform that can power and sustain embedded sensing functions using just the power present in these TV signals in the air is covered in this this part of the research effort.

CHAPTER 1. INTRODUCTION

Energy harvesting is the practice of generating energy from natural occurrences taking place in an ambient setting. The harvested energy is a free source of energy from non-fossil fuels that exploits naturally occurring phenomena, such as moving wind or water, sunlight, temperature differences, naturally occurring kinetic motion, and salinity difference to generate power. Energy densities of energy-harvesting technologies tend to be lower than those of fossil fuels and conventional batteries. In the developing world, energy harvested from solar and kinetic motion is used as the main source of power. Important uses of energy-harvesting technologies in the developed world are for powering wearable electronics, and wireless sensor networks (WSNs). Energy harvesting is useful in applications where replacement of batteries is inaccessible or logistically expensive, and being tethered to power mains tends to be impractical. Biomechanical energy harvesting, which is the generation of energy by body movements, can prove to be useful in powering biomedical devices and some consumer electronics such as MP-3 players and cell phones [*1*] [*2*]. Wireless sensor networks are useful in a large number of applications and industries, such as smart-grid and home-environment monitoring; structural-health monitoring; agricultural sensing; environmental sensing of air, water, forests, and natural disasters; industrial monitoring and data logging; and logistics [*3*]. Energy is the scarcest resource of WSN nodes. Component and system-level developers of WSN motes have been working towards maximizing the mote's operating life through improvements in power efficiency of the hardware and software protocols used to carry out sensing and ad-hoc communication of sensed data in a network.

A number of different energy-harvesting technologies using photovoltaic cells, micro-electromechanical systems (MEMS), pyro-electrics, and magneto-static devices are proving

useful in maximizing the operating lifetime of WSN motes in a number of sensing and machine-to-machine (M2M) applications. One of the goals of this research effort is to measure and characterize ambient wireless signals present in urban areas. The second goal of this work is to develop the means to harvest energy from wireless signals that are present in the ambience for battery-less operation of WSN motes.

The dissertation thesis is organized as follows:

- An introduction to green RF technologies that involve biodegradable electronics and energy harvesting sources is presented in Chapter 2.
- Background information on different energy harvesting techniques, and latest efforts in the areas of wireless energy harvesting is presented in Chapter 2.
- Research work in the design and development of biodegradable wireless sensor systems is presented in Chapter 3.
- Research work in the design and development of a solar-powered, RFID tag (SOLTAG) for remote tracking of automobile vehicles is presented in Chapter 4.
- Research work performed to realize a battery-less platform that is capable of powering embedded sensing functions from harvested, ambient wireless TV signals is presented in Chapter 5.

CHAPTER 2. ORIGIN AND HISTORY OF THE PROBLEM

2.1 Electronic Waste (E-Waste)

Nearly 3,140,000 tons of electronic waste was generated in the United States and Canada in 2011 [*4*] [*5*]. Close to 50% of the electronic waste in most electronics is from the packaging material or substrate used, which is made up of silica, glass, or plastics (see **Figure 1**). Glass-reinforced and epoxy-laminated ceramics are known in the electronics industry as FR-4. FR-4 is the most commonly used substrate material in printed circuit board designs [*6*]. FR-4 ceramics used in electronics take decades to biodegrade, and are one of the main sources of increasing electronic waste in landfills and waste dumps around the World. Toxic chemicals and heavy metals in batteries in waste dumps are responsible for contamination of soil and water in the vicinity of dump sites and landfills [*7*].

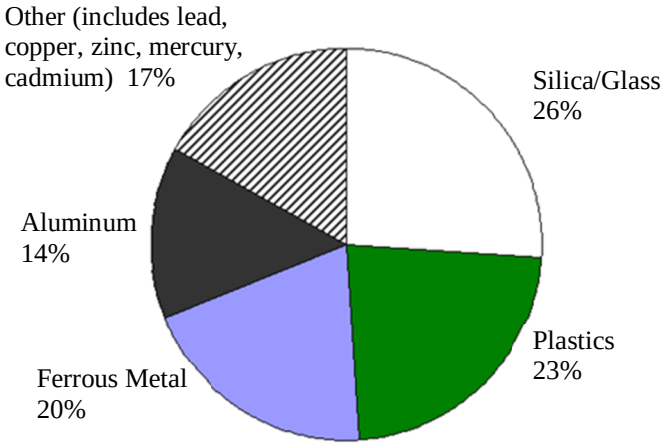

Figure 1. Make up of personal computers and smart phones [*8*]**.**

Electronic waste can be a particular problem in widely deployed radio-frequency identification (RFID) and wireless-sensor network applications, where the logistics of replacing

and recycling batteries for the large number of devices deployed can prove to be cumbersome and expensive. The use of organic substrates, such as paper and liquid-crystal polymer using direct write methodologies for RFID and mm-wave identification (mm-ID) applications can cut material and fabrication waste as shown by Vyas et al. and Rida et al. in [*9*], [*10*], [*11*] and [*12*].

2.2 Kinetic Energy Harvesting

Modern consumer electronics and household electrical appliances, which are continuously operated for extended periods of time, will require the energy density of a battery or a tethered power supply. Widely deployed RFID and wireless-mesh networks on the other hand draw peak power for limited duty cycles only, and can be powered using ambient, energy-harvesting techniques. Windmills, invented around the year 1 AD by the Greek engineer Heron of Alexandria, are the earliest known example of an energy-harvesting device [*13*]. Originally invented for milling grains and powering machines for irrigation, wind turbines are being increasingly used to power homes and industries. Wind power had a global output capacity of close to 40 gigawatts by the end of 2011 [*14*]. A wind turbine scaled down to a centimeter in size, and capable of generating between 80 microwatts and 2.5 milliwatts, has been developed by Howey et al. for monitoring fluid flow in pipes and ducts used in HVAC systems [*15*]. Electromagnetic means of power generation, which are common in the generation of hydro-electric and wind-power are increasingly being used in a smaller scale to supply power to WSN motes and some consumer electronics. Electromagnetic power is generated by physical displacement of magnetic structures that are intertwined in a coil [*15*] [*16*]. Portable, electromagnetic, power-generating mechanisms are capable of having power densities between tens of microwatts and one watt range from external acceleration amplitudes of between 0.1g and

50g, which occur at low vibration frequencies of 80 Hz or less using devices with dimensions ranging from a few square mm to a few square feet [*16*] [*17*]. Compared to electromagnetic energy harvesters, piezo-electric films and cantilever-based mechanisms commonly use micro-electromechanical system based fabrication methods, and tend to be smaller in the micron or millimeter size range with higher resonant frequencies in the 10 to 1500 Hz range. The smaller sizes however cause piezo-electric devices to give out only between 0.64 and 64 microwatts of output power [*18*] [*19*]. Shoe-mounted power harvesters in recent years that make use of an electromagnetic or eletrostaic discharge have shown to generate 0.25W and close to 1mJ [*20*] [*21*].

2.3 Thermal Gradient based Energy Harvesting

In addition to kinetic motion, energy harvesters using thermal gradients across multiple surfaces to generate a usable output voltage potential are also an ongoing research topic. Metallic and semiconductor surfaces at different temperatures are being used to induce charge flow and a voltage potential across two junctions using Seebeck or Peltier effect. Micro-thermal generators measuring 59 by 10 mm are capable of generating 15.7 microwatts of power from temperature differences of 85K [*22*]. A comparison of power densities offered by different power harvesting technologies is shown in Table 1 below [*23*].

Table 1. Energy-harvesting sources [*23*].

Energy Source	Harvested Power
Vibration Motion	
Human	4 uW/cm^2
Industry	100 uW/cm^2
Temperature Difference	
Human	25 uW/cm^2
Industry	1-10 mw/cm^2
Light	
Indoor	10 uW/cm^2
Outdoor	10 mW/cm^2
Ambient RF	
Cellular	0.1 uW/cm^2
WiFi	0.001 mW/cm^2
UHF TV	0.012-0.17 uW/cm^2

While kinetic and thermal based energy harvesters do show preliminary capability to power wireless sensor modules, the power source is largely localized to a host that is either vibrating or at elevated temperatures. Also, differences in temperature or displacement have to be large enough for the energy harvester to generate substantial output power levels.

2.4 Solar based Energy Harvesting

Compared to kinetic motion and thermo-electric harvesters, Solar power is far more pervasive with higher power density as shown in Table 1. Wireless sensor networks operated by solar power have been proposed for a number of applications. Heliomote is the first implementation of a wireless platform operated by solar power [*24*] [*25*]. Another solar powered platform called EnHANT uses an organic, semiconductor based solar cell, which is suitable for indoor use and ultra-low power communication enabled by ultra-wideband impulse radio [*26*].

2.5 Wireless Energy Harvesting

In addition to Solar, wireless power is also becoming more pervasive due to the expansion of wireless infrastructure in most urban areas because of expanding cellular and digital TV broadcasts. Depending on the number of users in the case of cellular or the number of TV channel offerings in an urban area, wireless power in the air can be present day and night unlike solar power. Also, wireless power in the ultra-high frequency bands offer more penetration depth through opaque objects unlike solar power.

The use of radio wave as a means to transfer electricity was first attempted by Nicola Tesla in the early 20th century [*27*]. Since then wireless power transmission techniques are known to be near field or far field technologies. Near field methods use magnetic induction between two coils to transfer power. Smart Locator system proposed by NEC Corporation makes use of magnetic induction to harvest hundred milliwatts of power from the electromagnetic noise radiated from illuminating fluorescent tubes [*28*]. Since the power transferring coil is in direct contact with the fluorescent tube, it is not suitable for wide area deployment. Electrical and Magnetic coupling resonance based wireless transmissions can help increase the range of near field based power telemetry systems but only up to several times the radius of the coils, which still curtails the range [*29*] [*30*].

Far-field wireless power transmission techniques make use of higher RF frequencies where electric fields can be radiated out more efficiently from antennas at longer range from a wireless power source. Passive EPC Gen-2 based radio frequency identification systems (RFID) used in the logistics industry and Satellite Solar Power System (SSPS) are well known examples of far field wireless power transfer systems [*31*] [*32*]. EPC Gen-2 RFID system uses between 2 and 4 watts of wireless power transmitted from a reader to activate battery-less RFID tags, which

convey back the tag identification number (GUID) by backscattering the wireless field of the reader. Attenuation suffered by the wireless power as a function of the inverse square of the distance, combined with losses in the RFID tag's wireless RF-DC mechanism, restrict the range of RFID system that operate in the 860-915 MHz range to 10 meters [*33*]. Addition of extra embedded and sensing capabilities atop the RFID as used in the Wireless Identification and Sensing Platform (WISP) system restrict the range of the passive power transfer scheme even further down to 3 meters [*34*]. There are also several RFID based sensing systems that perform sensing functions without a battery but cannot sense or relay the sensed data independent of the power from a dedicated wireless power source, which is a reader [*35*] [*36*]. Paint et al. have proposed an RF energy harvesting wireless sensor network node, which receives energy from 2.45GHz transmitter. Similar, wireless powered telemetry systems requiring a dedicated wireless power sourcing transmitter has also been commercialized by Powercast [*37*].

SSPS is an idea mentioned by Glaser et al. to use photovoltaic cells to convert un-attenuated solar power in space and beam it down to earth using wireless telemetry [*32*] [*38*]. An efficient rectifier and an antenna (rectenna) have been developed for SSPS [*38*] . Sample et al. have showed a feasibility of exploiting ambient RF signals to operate a commercially available low power temperature and humidity sensor consuming between 25 and 50 microamperes of current [*39*]. Due to the inverse square of the distance relationship in wireless propagation, peak wireless power densities at long range from a wireless power source are expected to be low in the fractions of a microwatt as shown in Table 1. The low ambient power levels make sustained powering of embedded and wireless link capabilities consuming 10mA or higher continuously using just the ambient wireless power impossible at long ranges.

In summary, a number of technologies have been developed or in development that use wireless power transfer mechanism for relatively short ranges. One of the tasks of this work is to carry out a systematic and quantitative analysis of the make-up of ambient wireless signals that are used in modern communication standards for cellular and TV broadcasts in urban areas, and evaluate its feasibility for battery-less sustenance of embedded and wireless sensing applications. **The main objective of this research is the design and development of a unique embedded wireless energy harvesting platform (E-WEHP) that can power and sustain autonomous sensing and machine to machine (M2M) applications without batteries but using only the ambient wireless power from existing wireless infrastructure present in most urban areas.**

CHAPTER 3. BIODEGRADABLE SYSTEMS FOR WIRELESS SENSING APPLICATIONS

3.1 Biodegradable Electronics for E-Waste Reduction

3.1.1 Material considerations

Use of any material as a dielectric substrate requires it to be characterized for its dielectric permittivity and loss to the oscillating fields propagating through any waveguide fabricated on it. A number of different materials, organic and ceramic, were considered for use as a dielectric substrate for waveguide structures and antennas for RF frequencies starting from UHF and extending potentially up to mm-wave frequencies.

A special perfluoropolymer material (PFA) manufactured by ASAHI glass company was considered for potential use as a substrate from UHF right upto the mm-wave frequency range. Potential benefits of using perfluoropolymer are its biodegradability compared to FR-4 glass based ceramics [*40*]. PFA also retains many inherent characteristics and similar properties of PTFE but can be processed using conventional thermoplastic techniques, such as extrusion molding, injection molding, blow molding, or electrostatic powder coating. On the RF circuit design side, PFA offers better adhesion to copper foil with a very smooth surface without any surface treatment, that helps minimize surface roughness and hence potentially surface resistance to high frequency charged carriers flowing through microwave structures fabricated with it [*41*]. Copper etched surface profile of the PFA yields surface roughness of 1.96 microns compared to 6.3 microns for PTFE/Glass laminate as shown in **Figure 2** [*41*]. PFA can be used in a wide range of temperatures from extremely low to high temperatures (260°C at the maximum) without losing its superior properties [*41*].

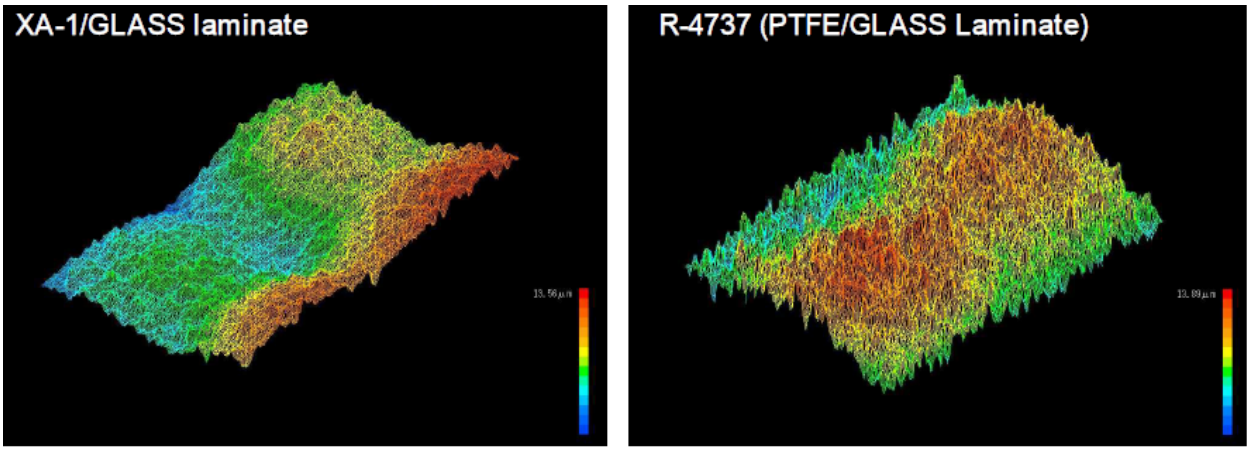

i ii

Figure 2. (i) Surface roughness profile of copper etched XA-1 PFA/ Glass based laminate (ii) Surface roughness profile of copper etched PTFE/Glass laminate [*41*].

The Dielectric permittivity of the PFA substrate was characterized by designing microstrip lines in the form of ring resonators to resonate around 10 GHz in the fundamental mode with an assumed dielectric permittivity of between 2.7 based on lower frequency analysis provided by ASAHI glass company. The rings were fabricated on a PFA substrate 275 microns thick metallized with copper of thickness 12 microns, and with a mean radius of 2.906 mm. The ring resonators were fed with 50 ohms CPW lines that were probe fed as shown in **Figure 3**. The fabricated ring resonators are shown in **Figure 4**. The insertion loss (S_{21}) across the ring resonators were measured using an Agilent 8350A vector network analyzer (VNA) up to 100 GHz. The effects of the cables and feed were de-embedded out using a Through-Reflect-Line Calibration using quarter wavelength transmission lines also fabricated on the same substrate as shown in **Figure 4**.

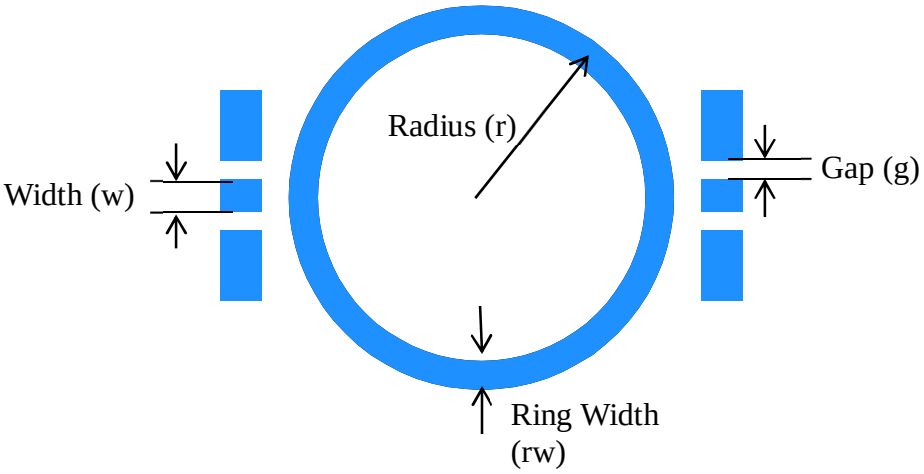

Figure 3. Ring resonator dimensions. Radius (r) = 2.906 mm, Ring Width (rw) = 0.73mm, Width (w) =0.73 , Gap (g) = 0.44mm

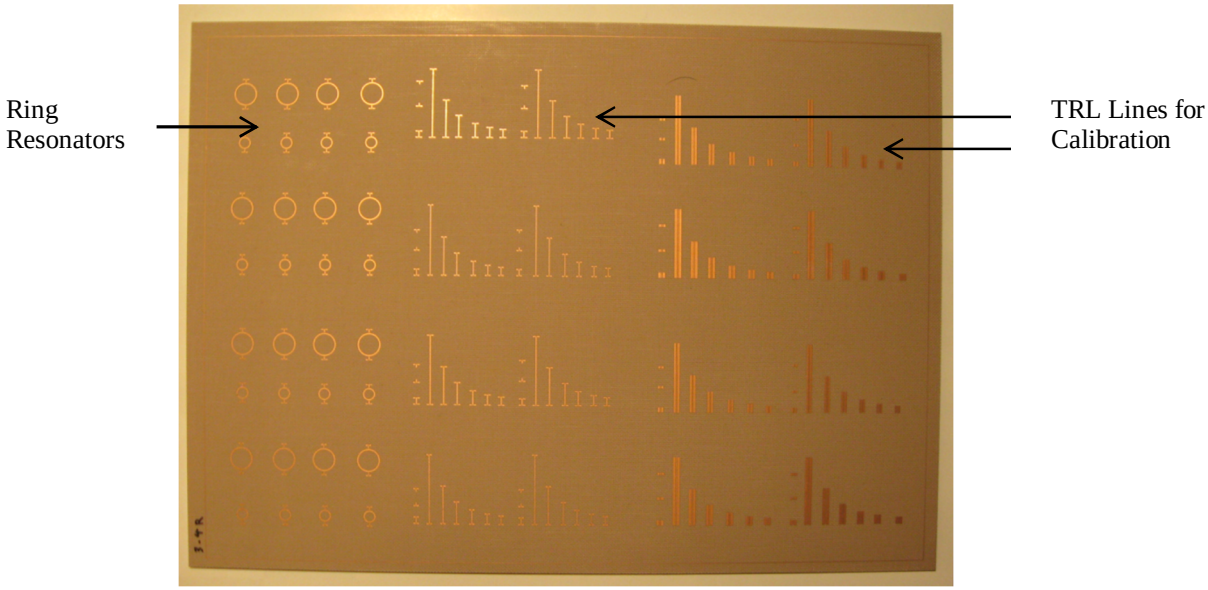

Figure 4. Fabricated ring resonators on XA1 Glass laminated perfluoropolymer substrate.

The ring resonator produces insertion loss (S_{21}) resonances at even harmonics (n). The relative dielectric constant (ε_r) for the PFA substrate can be extracted from the location of these

resonances, while loss tangent (tanδ) is extracted from the quality factor of the resonance peaks along for each of the four ring resonators shown in **Figure 4**. The relative dielectric constant (ε_r) can be extracted from the effective dielectric constant (ε_{eff}) and the dimensions of the microstrip lines used in the ring resonator by using (1) [*42*] [*43*]. The effective dielectric constant is a function of the ring radius (r), the n_{th} resonant frequency (f_o) obtained from measurement of the insertion loss (S_{21}), and the speed of light in vacuum (c), as defined in (2). The parameter 'M' in (1) is extracted from the physical dimensions of the microstrip lines used in the ring resonator, namely the height of the substrate (h), the conductor thickness (t) and width (w) as in (3) [*44*] [*45*].

$$\varepsilon_r = \frac{2 \times \varepsilon_{eff} + M - 1}{M + 1} \tag{1}$$

$$\varepsilon_{eff} = \left(\frac{n \times c}{2 \times \pi \times r \times f_0} \right)^2 \tag{2}$$

$$M = \left(1 + \frac{12 \times h}{w + \frac{1.25 \times t}{\pi} \left(1 + \ln\left(\frac{2h}{t} \right) \right)} \right)^{-0.5} \tag{3}$$

The loss in the rings occurs mainly due to the conductors, lossy dielectrics and radiation. The loss tangent of the paper substrate is a function of only the attenuation due to the dielectric (α_d) at the resonant frequency and is computed using (4). The attenuation due to the dielectric was

extracted by subtracting the attenuation due to conductor (α_c) and radiation (α_r) losses from the total attenuation (α_{total}) experienced by the resonator. The total attenuation experienced by the resonators is obtained from its quality factor (Q_0), which is a function of the half power bandwidth (BW) and the magnitude of the insertion loss resonance as in (6) and (7). The effective wavelength (λ_{eff}) of the fields propagating through the resonators is obtained from the effective dielectric constant and free space wavelength (λ_0) as in (8). The conductor losses in the resonators were extracted using (9) which is a function of the AC resistance (R_{ss}) and dimensions of the ring conductor. The AC resistance is determined from the skin depth (d) of the conductor offered to the propagating RF signal that is a function of the metal conductivity (σ_{Cu}) and surface roughness (Δ) and the permeability of the substrate (μ_0) as in (10) and (11).

$$\tan\delta = \frac{\alpha_d \times \lambda_0 \times \sqrt{\varepsilon_{eff}}\left(\varepsilon_r - 1\right)}{8.686 \times \pi \times \varepsilon_r \left(\varepsilon_{eff} - 1\right)} \tag{4}$$

$$\alpha_d = \alpha_{total} - \alpha_c - \alpha_r \tag{5}$$

$$\alpha_{total} = \frac{\pi}{Q_0 \lambda_{eff}} \tag{6}$$

$$Q_0 = \frac{f_0}{BW \times \left(1 - 10^{|S_{21}|/20}\right)} \tag{7}$$

$$\lambda_{eff} = \frac{\lambda_0}{\sqrt{\varepsilon_{eff}}}$$

(8)

$$\alpha_c = \frac{R_{ss}}{Z_0 * h} \times \frac{8.686}{\left(\frac{w_{eff}}{h} + \frac{2}{\pi} \ln\left(2\pi \times e\left(\frac{w_{eff}}{2h} + 0.94 \right) \right) \right)^2} \times \left(\frac{w_{eff}}{h} + \frac{\frac{w_{eff}}{\pi h}}{\frac{w_{eff}}{2h} + 0.94} \right) \times \left(1 + \frac{h}{w_{eff}} + \frac{h}{\pi \times w_{eff}} \left(\ln\left(\frac{2h}{t} + 1 \right) - \frac{\left(1 - \frac{t}{h} \right)}{\left(1 + \frac{t}{2h} \right)} \right) \right)$$

(9)

$$R_{ss} = \sqrt{\frac{\pi \mu_0 f_0}{\sigma_{Cu}}} \times \left(1 + \frac{2}{\pi} \tan^{-1}\left(1.4 \times \left(\frac{\Delta}{d} \right)^2 \right) \right)$$

(10)

$$d = \sqrt{\frac{1}{\pi \mu_0 \sigma_{Cu} f_0}}$$

(11)

The dielectric permittivity for the four different ring resonators fabricated was found to vary between 2.5 and 3.2 as a function of frequency as shown in **Figure 5**. The loss tangent for the same resonators varied from 0.0029 to a maximum of 0.11 in the same frequency range as shown in Figure 6. While results obtained using ring resonance methods are accurate for permittivity extraction, the loss tangent results are expected to be inaccurate. The inaccuracy is due to a lack of accurate numerical techniques to extract radiation losses from the total losses in (5). The dielectric permittivity and loss tangent for organic substrates namely PFA and a commercially available organic Kodak photo-paper are shown in **Table 2**. The numbers in **Table 2** show that it is feasible to develop RF electronics on organic substrates spanning frequencies form the low UHF to mm-wave frequencies.

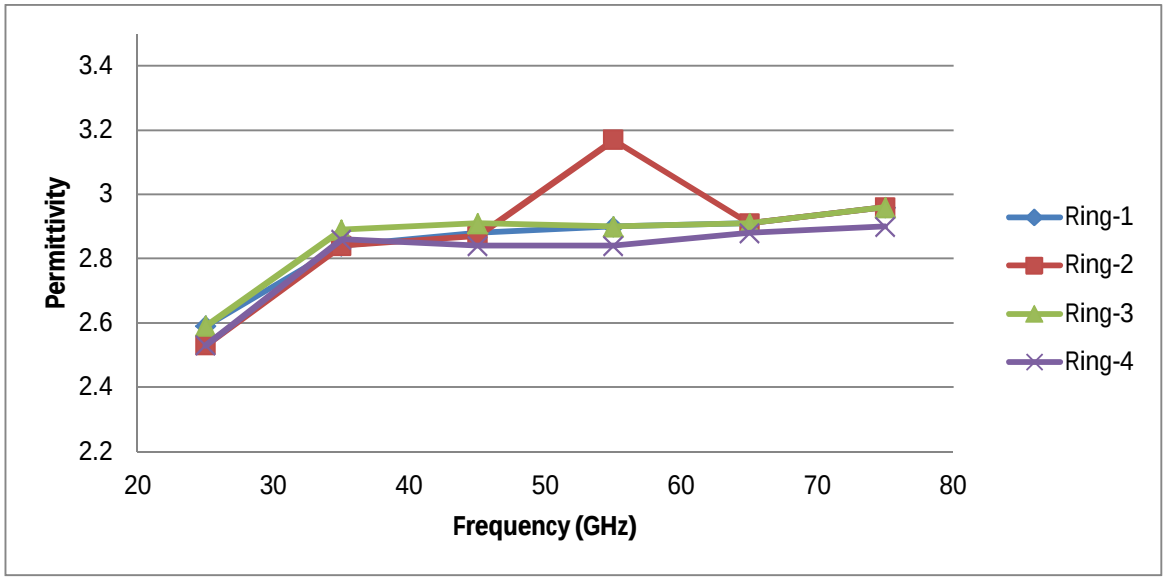

Figure 5. Dielectric Permittivity of perfluoropolymer material substrate (PFA) extracted using ring resonance method.

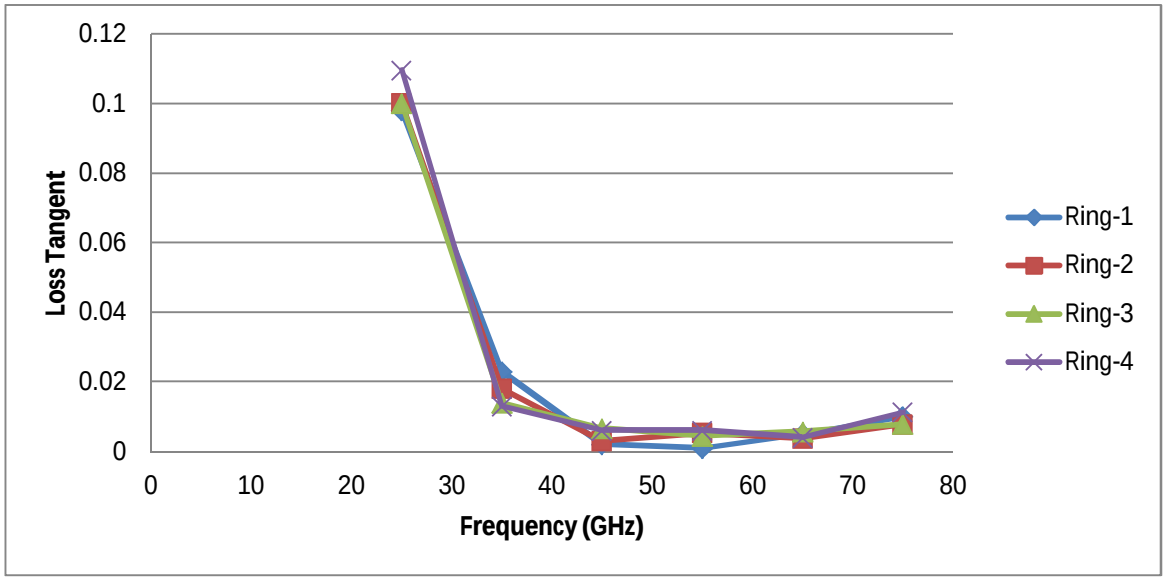

Figure 6. Loss Tangent of perfluoropolymer material substrate (PFA) extracted using ring resonance method.

Table 2. Electromagnetic propagation characteristics of PFA and Paper based Organic substrates.

Organic Substrate	Frequency	Dielectric Permittivity	Loss Tangent
Kodak Photopaper [*43*]	0.2-1.6 GHz	3.2-3.5	0.065-0.08
ASAHI Perfluoropolymer (PFA)	25-75 GHz	2.5-3.2	0.0029-0.11

3.1.2 Inkjet-printed Wireless Systems

Material characterization of organic PFA and Paper based substrates in the preceding section demonstrates the feasibility of their use as dielectric substrates for high frequency circuits operating at ultra-high frequency bands (UHF) up to mm-wave frequencies. Biodegradable substrates, especially paper based ones, are typically more pervious to moisture that allows for organic growth, which causes the material breakdown required for biodegradation. While organic photo paper tends to be more impervious to moisture in the environment that is required for RF performance, corrosive acidic etchants could still eat into its outer coating causing material breakdown or dielectric property change. A relatively clean inkjet printing process was developed and used to deposit metals onto organic substrates such as photo paper. The Inkjet printing process for fabricating electronics offer substantial advantages over competing metallization processes such as milling or wet etching.

Traditional wet etching techniques that form the backbone of the conventional PCB fabrication process involve complete metallization of substrate laminates and subsequent selective etching of portions of the metal layer on top of the substrate using etchants as shown in **Figure 7**. Common wet etchants are solvents containing de-ionized water mixed with highly

corrosive acids, such as Nitric acid, Sulfuric acid and hydrofluoric acid. In addition to being hazardous to their handlers in cleanrooms, the washed out etchants combined with the discarded metal particles constitute a significant amount of waste in the circuit fabrication process, that require special treatment pre-disposal. Milling machines are also used to realize circuits on metal laminated substrates. They operate like plotting machines with milling bits that that selectively rub out unwanted metal off PCB boards. While they do have the advantage of not generating any etchant waste, they do generate metal files that are milled out of the board. A drawback of these machines is that they use a combination of servo motors not just to move the plotting arms but also push down and rotate the milling bits as they rub out the metal, which makes them very power hungry. In addition, their minimum pitch is 100um in contrast to below 50um for inkjet printing and wet etching methods making printing relatively more imprecise for frequencies beyond UHF. Laser milling machines have precisions comparable to inkjet printing (~50 um) but require high amounts of power of the order of kW and are unsuitable for metal cutting on thinner and flexible substrates such as paper and PET [*46*] [*47*].

i ii. iii.

Figure 7. (i) Copper Laminated Liquid Crystal Polymer Substrate (LCP) (ii) Single RFID tag fabricated on LCP by etching away laminated copper (iii) Array of RFID tags fabricated on LCP sheet by etching away large areas of laminated copper [*48*].

Inkjet printing of conductive material over a substrate offers substantial benefits over the previous methods in terms of reduced waste and ease of functionality. It typically uses an electrostatic potential (5-12V) difference between a charged electrode attached to the ink cartridge and the base plate on which the substrate is mounted [*46*] [*49*]. This results in the charged ink particles to ooze out of the nozzle and deposit on the substrate. The ink once printed is sintered on the substrate solidifies and forms the conductive layer on the substrate. The ink cartridge is mounted on a mechanical arm that is servo controlled to move in the x-direction and the base plate on which the substrate is mounted moves in the y-direction. This allows the inkjet printing process to selectively metalize the substrate causing no material waste as shown in **Figure 8** [*46*]. The frugal and "green" nature of inkjet printing for fabricating substrates on low cost organic flexible substrates such as paper make it ideal for large scale reel-to-reel processing with very high repeatability. This process is particularly ideal for large area circuits which do not contain large metal areas, such as wireless sensors and 3D RF communication and control modules [*46*].

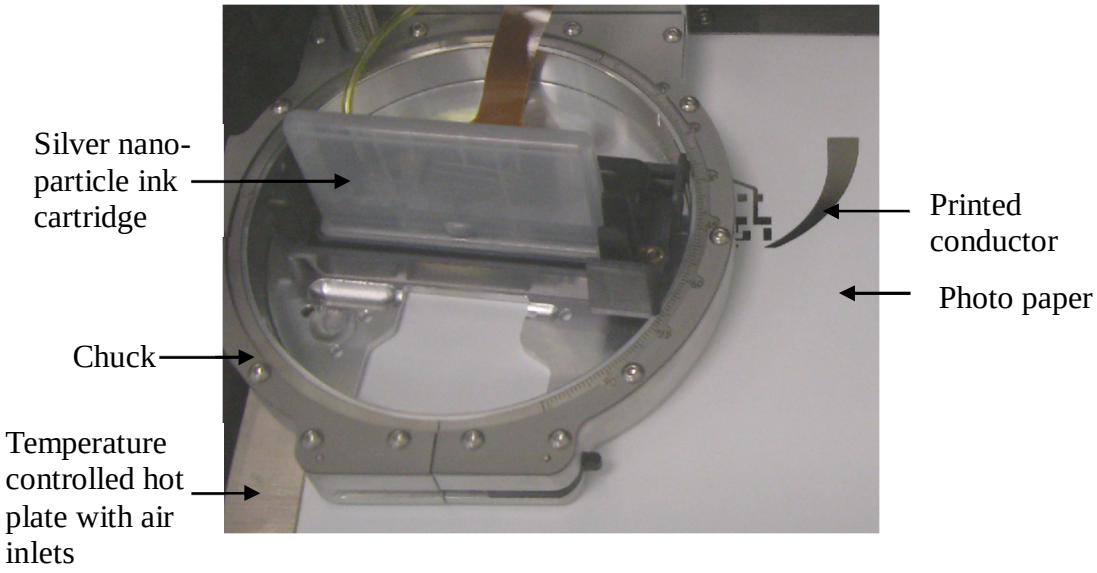

Figure 8. Inkjet-printed conductor on paper based substrate.

In addition to creating zero material waste through its selective ink spraying ability, inkjet printing also offers a unique versatility with regards to material deposition. Conventional cleanroom processes use different equipment for variable material deposition on substrates, such as different DC sputtering machines to shoot different metals in plasma form onto substrates typically at very low pressure. Non-metallic materials are typically deposited using RF sputterers or ion deposition, which have to be etched out as a 2nd step to get the desired material pattern on the substrate. Unlike bombarding substrates with plasma or ion vapor, inkjet printing uses electrostatic potential to deposit charged ink solvents in inkjet cartridges onto a substrate [*46*]. The print head sprays out controlled amounts of ink on it through multiple microscopic nozzles 254 um apart each about 21.5um in diameter as shown in **Figure 9** [*49*]. The print head temperature can be user-controlled (up to 70 C) in order to lower the viscosity of the ink solvents to between 10-12 cPs. The series of nozzles also have a filter to leave out large particles from the deposited ink size around 0.2 um. Solvents containing the desired deposits can be easily

formulated by combining material to be deposited with agents they are soluble in. The versatility of inkjet printing with regards to material deposition make it ideal for embedding sensing elements as well as functionalized nanostructures (such as Carbon Nanotubes – CNTs) onto circuit platforms for wireless or near- field sensor telemetry constituting an extremely low-cost alternative to conventional material deposition technologies for the rapid and large-scale prototyping of low-power/zero-power RFID-enabled wireless sensors [*46*].

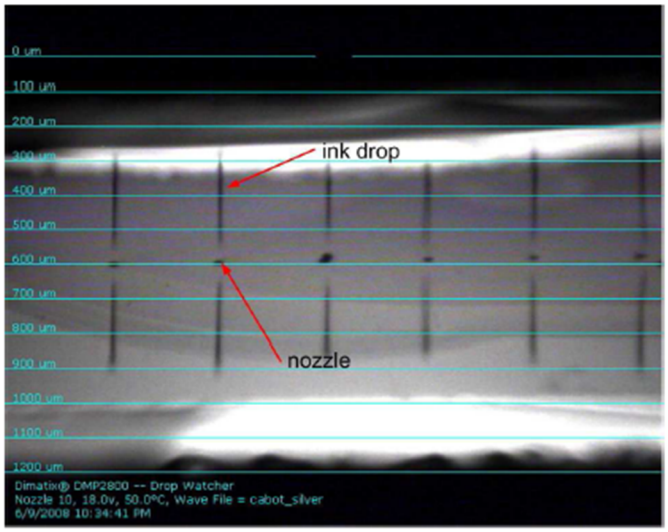

Figure 9. Ink printed out of series of nozzles on print head of inkjet printer.

In addition to cutting down on waste and providing an all-in–one alternative to cleanroom deposition technologies, inkjet-printing attributes with regards to accuracy and form make it a very good contender for RF circuits. While the feasibility of inkjet printing for applications at UHF frequencies has been well covered under [*10*], [*43*], [*50*] [*51*] [*52*] [*53*], its usability for application at even higher frequencies have not been investigated thoroughly. Operating at even

higher frequencies in the SHF range (3GHz – 30 GHz) require metallization that have relatively higher conductivities, low surface roughness and with even smaller dimensions. The ink is sprayed in the x-direction while the base plate with the substrate on moves in the y-direction to print an area. Due to this the resistance of the sprayed ink could be different in the x-direction from the y-direction. Ensuring uniform conductivity over the printed structure especially at microwave frequencies requires that the sprayed ink once treated has uniform distribution in both the x and y directions. Getting such a uniform surface profile with inkjet printing requires choosing the correct ink, the correct spray volume, printer settings, and ink treatment after it has been printed on the substrate. Using a print head capable of spraying out ink at a higher volume ensures a better overlap between adjacently sprayed conductive ink particles as they blot a little once being deposited on the substrate surface. This helps increase conductivity in both x and y directions. Figure 10 (a) and (b) shows the surface profile of an RFID antenna printed using cartridges spraying out ink droplets with volumes of 1pL and 10pL. In the former case, the striations along the antenna in the y-direction lead to an increased resistance in that direction compared to the latter case where a higher print volume ensure an overlap between each successively printed layer in the y-direction. The resulting range of the RFID in the latter case was increased almost by a factor of 100 as shown in [*10*] and [*54*]. The resistance of the printed structure can also be further reduced by using a higher print resolution setting on the printer. RF circuits printed and tested using this technique have shown a printing resolution of 1000 dpi suitable for frequencies in the UHF range [*46*].

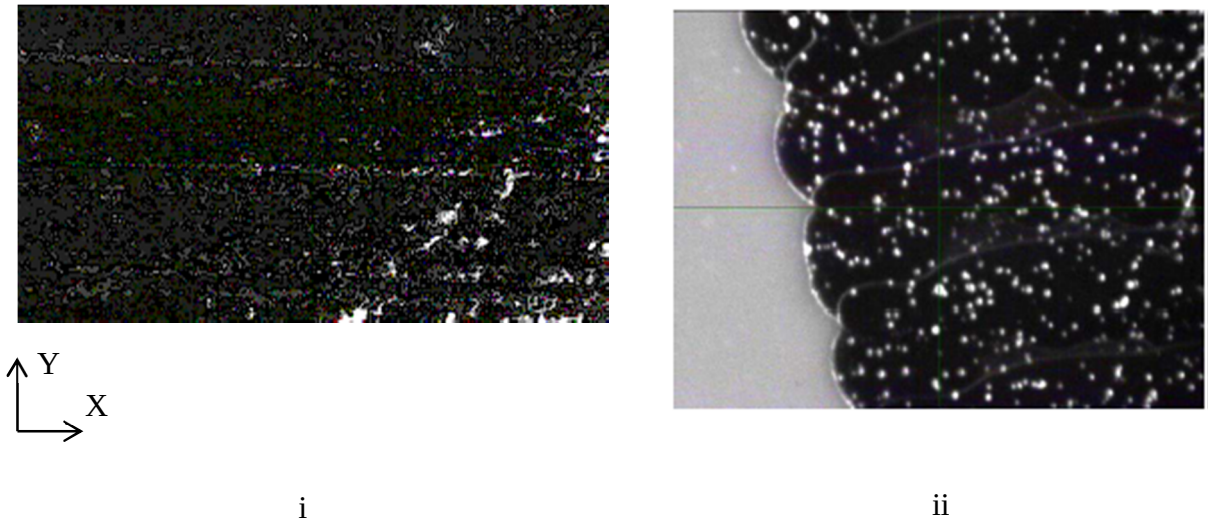

i ii

Figure 10. (i) Printed conductive ink layer with a volume of 1pL. (ii) Printed conductive ink layer with a volume of 10pL.

After printing, the deposited ink also needs to be annealed under the right conditions to ensure adjacent silver nano-particles in the sprayed ink to gel with it neighbors allowing for a more uniform path for electron flow especially at microwave frequencies. The pre-annealing and post-annealing effects on the conductive silver nano particles in the printed ink, as observed under an SEM, are shown in Figure 11 [*43*]. Structures with very good conductivity and fine pitches suitable for frequencies well above UHF can be very accurately fabricated using the inkjet printing process as shown by the close-up of a printed transmission line in **Figure 12** [*46*].

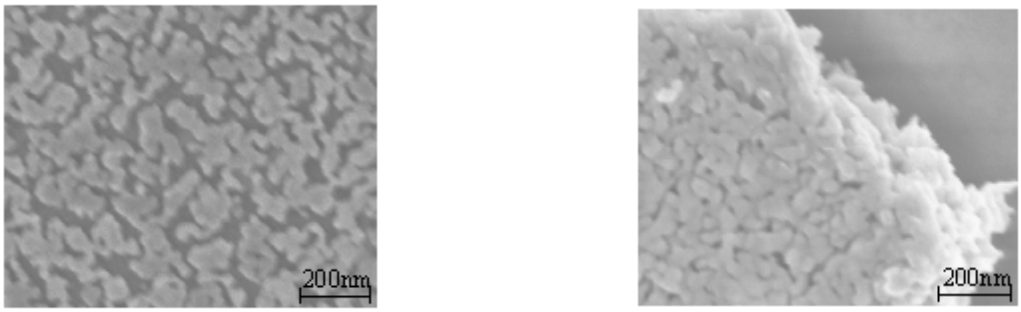

i ii

Figure 11. SEM images of a layer of printed silver nano-particle ink, after 15 minutes cure at: (i) 100C (ii) 150C

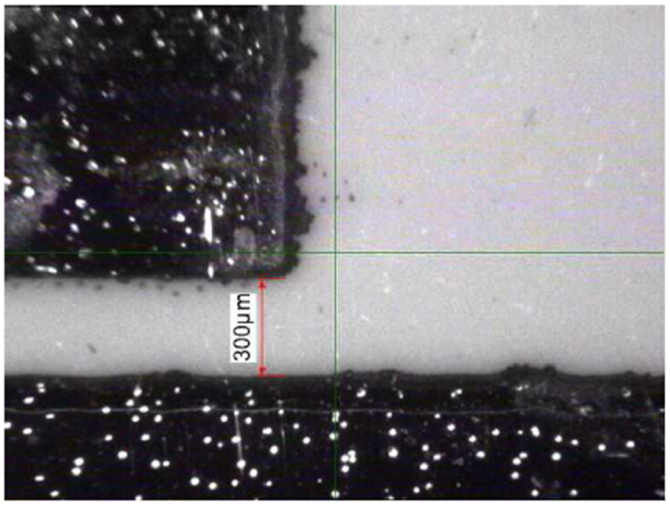

Figure 12. Fiducial image of a Coplanar Waveguide (CPW) line inkjet printed for microwave frequencies with resolution of 300 microns. [*46*]

With a dielectric permittivity of 3.1, that is very stable well into the UHF range (variation between 3.05-3.15 up to 15 GHz), paper offers a bio-friendly/eco-friendly alternative to ceramic based substrates such as FR-4 (dielectric permittivity = 3.2), which are also operable up to the UHF range, as well as to current wasteful PCB and PET circuit fabrication techniques. The low temperature tolerance of the paper (150-170 deg. C), however, does make soldering discrete

components on it unfeasible. Nevertheless, highly conductive silver epoxy does provide a very reliable solution given its relatively low temperature curing requirement. At room temperatures, silver epoxies tend to be free flowing but harden and attach themselves to the printed silver pads when cured at higher temperatures between 120 and 160 degrees Celsius for a certain period of time. In detail, discrete IC components can be mounted on the inkjet printed circuit layout using a 2-step process as shown in **Figure 13** (i). The first step involves holding the components in place on the printed silver pads with the use of a very small amount of adhesive between the component terminals and printed silver pads. Once in place, conductive silver epoxy can be afterwards applied on the terminals of the components to establish a conductive path between the terminals and printed silver pads [*10*]. A close-up of the free flowing silver based epoxy manufactured by epo-tek on a printed Coplanar Waveguide pads (CPW) is shown in **Figure 13** (ii). The viscosity of the epo-tek epoxy (50-50% mixture of resin and hardener) was low enough for it to percolate through via holes drilled through paper [*10*] [*46*].

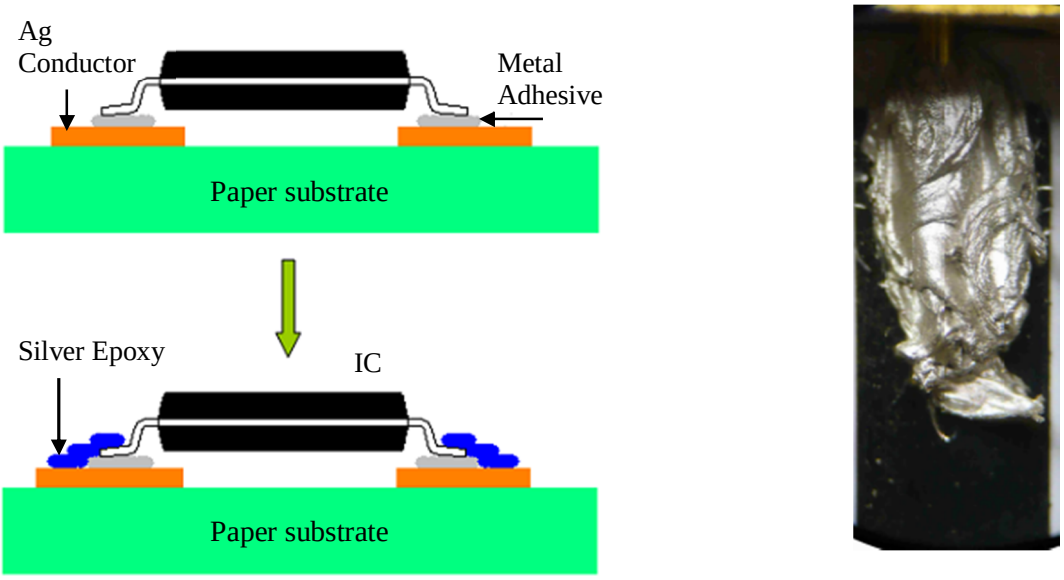

Figure 13. (i) I.C. component mounting process on inkjet-printed silver pads. (ii) Conductive Silver Epoxy.

While the use of inkjet printing technology as a packaging material for passive structures liks antennas has been well demonstrated in [*10*], [*35*], [*43*], [*46*], [*50*], [*51*], [*52*], [*54*], [*55*], [*56*], [*57*], [*58*], its use as a packaging material for complete wireless sensor modules that incorporate active and passive electronics is covered in this section. In addition to quasi transverse electromagnetic signals at RF frequencies, wireless and RFID based sensor modules also include high speed digital and low frequency analog signals generated by embedded processors. Also, conductive epoxies have to be used instead of solder since organic paper based substrates cannot handle the temperature hotspots generated by a soldering iron as in Figure 3.1.2f of the preceding section. The feasibility of the inkjet-printed, silver nanoparticle laced conductive traces along with its silver epoxy interconnects to interface between active and passive circuitry is covered in this section.

To investigate the feasibility of paper as an RF frequency substrate and packaging material, two microcontroller-enabled wireless sensor modules were realized on a photo-paper substrate for the first time. The first wireless sensor module prototype using a dipole antenna was printed on a 2-D (single layer) paper module, and the second prototype using a monopole antenna was printed on a 3-D (multilayer) paper module that is covered in the subsequent section. The system level design for the wireless transmitters can be seen in **Figure 14**.

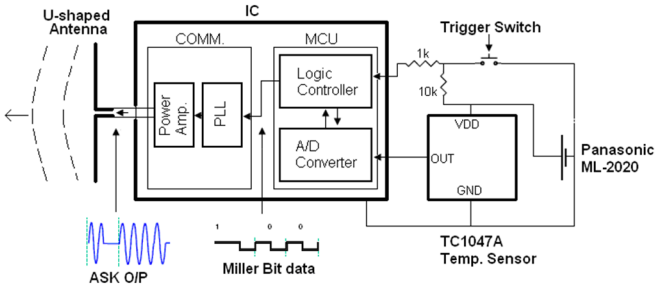

Figure 14. System Level Diagram of the Dipole and Monopole based Wireless Sensor Modules. [*10*]

The RFPIC12F675H wireless IC (RFPIC) made by Microchip comprising of an integrated 8-bit microcontroller unit (MCU) and a UHF ASK/FSK transmitter in a single integrated circuit chip (IC) was the primary controlling mechanism of the wireless sensor module. Using a Reduced Instruction Set Computing (RISC) architecture and assembly code, the MCU was programmed to operate the wireless sensor module in 3 different modes namely SLEEP, SENSE and COMM. The MCU was programmed to stay in a low power sleep mode (SLEEP) as its default state, which was an extremely low power state consuming only ~1.8 microwatts from the CR2032 Li-ion battery [*54*], [*10*]. A software encoded external interrupt generated by the trigger switch was used to wake up the MCU at which point its internal clock

was ramped up to 4 MHz to enter the SENSE mode by firmware control. In SENSE mode, the MCU was programmed to sample and digitize analog temperature readings from an external Microchip TC1047 temperature sensor using its in-built 10 bit analog to digital converter module (ADC) [*59*]. The digitized temperature readings were sampled 4 times and averaged, which was then stored in the MCU's program memory. The average temperature readings were then bit encoded by the MCU using a complete 2 sub-carrier cycle Miller bit encoding in order to transmit them asynchronously while conserving bandwidth in the Communication mode (COMM) as is typical with most mid-range UHF communication standards [*54*] [*60*], [*10*]. In COMM mode, the MCU was programmed to enable the in-built UHF ASK/FSK transmitter module in the RFPIC, which takes in a reference frequency generated by the RF crystal oscillator and generates an output signal locked in at 32 times the reference frequency at around 905 MHz as in **Figure 15**.

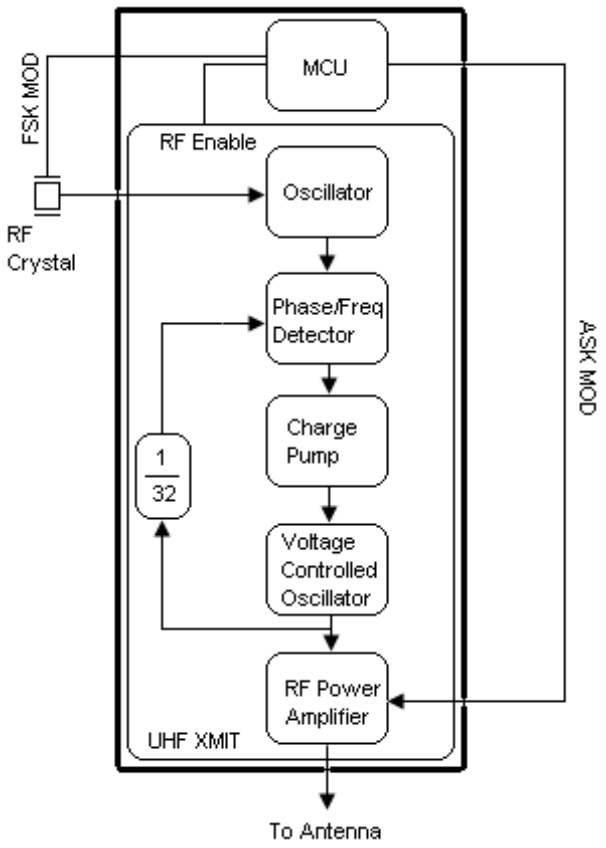

Figure 15. System Level Diagram of Wireless transmitter.

The MCU was programmed to produce a clock delay of 600 micro-seconds upon enabling the transmitter module to allow the RF crystal oscillator input to stabilize and the PLL to lock onto an output frequency is equal to 32 times the reference frequency of the RF crystal oscillator [*54*], [*10*], [*61*], [*62*]. The MCU was programmed to control the wireless communication by modulating the Power amplifier in the transmitter at calculated intervals thereby producing an amplitude shift keyed (ASK) modulated signal at the output of the RF Power Amplifier (PA) with the required data rate [*62*].The modulation by the MCU was carried out in the same sequence as the miller bit encoded sensor data that was sampled and averaged during the previously described SENSE mode. The output data rate was generated by using the internal clock of the MCU to toggle the RF power amplifier. With a 4 MHz internal clock, the

time to execute one instruction was 4 times the clock period, which was 1 microsecond by the MCU [*62*] [*63*]. This clock delay was used to control the time duration between the enabling and disabling of the PA thereby controlling the modulated RF output waveform and by it the data rate as shown in **Figure 16**.

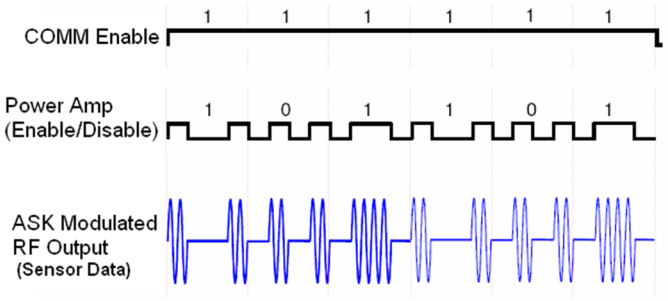

Figure 16. COMM Module Inputs and Output (time axis not per scale).

The number of program instructions 'n' required by the MCU to produce the correct delay between the toggling of the PA that would generate a desired data rate 'DataRate' can be determined from (12) where 'x' is the cycles-per-clock delay in implementing a single instruction by the MCU CPU, which for the RFPIC is 4 clock cycles per instruction. The clock frequency of the MCU '$f_{MCU\text{-}CLK}$' was set by software to be 4 MHz. The parameter 'n' in (12) is the user controlled time delay in the MCU software to generate the desired output baud rate, and which is set to 146 to generate 6.8kbps output as verified by the wireless link measurement from the wireless sensor module captured by a Tektronics RSA30408A real time spectrum analyzer as shown in Figure 3.1.3d. The data rate is the reciprocal of the measured bit duration shown in **Figure 17** [*10*].

$$DataRate = \left(n \times x \times \frac{1}{f_{MCU-CLK}} \right)^{-1} \tag{12}$$

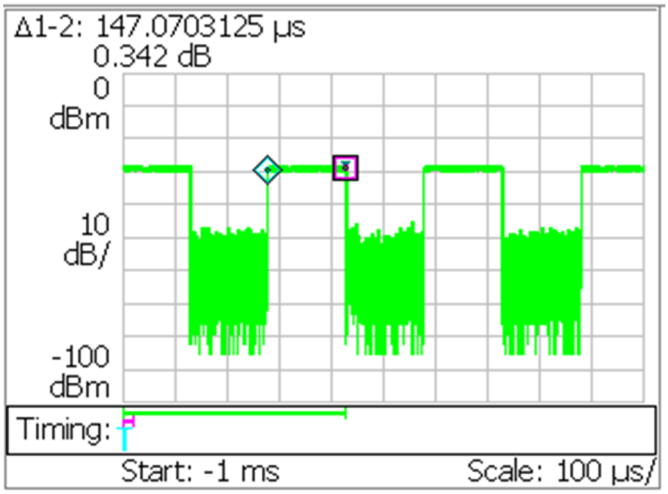

Figure 17. RTSA Measured ASK modulated signal with 50% duty cycle. (Power vs. Time)

The range of the wireless transfer is directly proportional to the amount of power transferred from the amplifier in the transmitter front end to the antenna. Any impedance mismatch between the two can lead to increased power reflection co-efficient, which is the reflection of a part of the power intended to radiate out of the PA plus its bias circuit into the antenna, thereby minimizing range. Kurokawa describes the concept of powered waves traveling between a generator and a load, and introduces the definition of power reflection co-efficient as shown in (13) [*64*]. The amount of power transfer from the PA to the antenna is given by 14. In order to maximize the power transfer co-efficient, the numerator in 13 needs to be minimized by ensuring that antenna impedance (Z_{ANT}) is as close as possible in value to the impedance looking into the combined Power amplifier and its bias circuit (Z_{PA}) in the RFPIC transmitter as shown in **Figure 18**.

$$|S|^2 = \left| \frac{Z_{PA} - Z_{ANT}^*}{Z_{PA} + Z_{ANT}} \right|^2 \qquad 0 \le |S|^2 \le 1 \tag{13}$$

$$\tau = 1 - |S|^2 \tag{14}$$

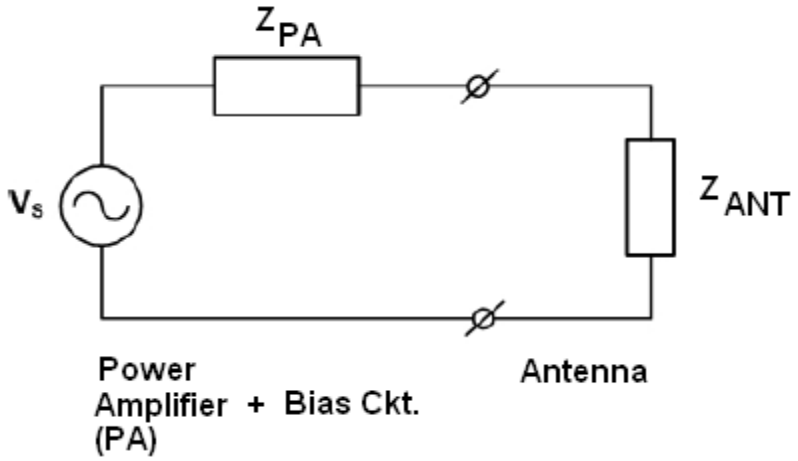

Figure 18. Equivalent Circuit Wireless Front end of Wireless sensor module comprising of Antenna and Power Amplifier (PA).

All power amplifiers have an optimum load impedance at which it gives out the most amount of output RF power for a fixed DC power supply [*65*]. To determine the optimum load impedance of the PA, a load-pull analysis was performed on it at 3 different frequencies of 860, 904.4 and 925 MHz, all of which fall within the unlicensed UHF frequency bands in the US and Europe used for RFID communication [*60*]. The analysis was carried out for a stable-bias point voltage of 3V provided by the Panasonic CR2020 Li-Ion battery with an RF choke in-between to

maximize the PA drain collector efficiency at 50% as typical for a PA in class-A mode of operation [*65*] [*66*].

The test setup and test board used for the load pull analysis is shown in **Figure 19** and **Figure 20**, respectively. For the load-pull analysis, the MCU was programmed to keep the wireless sensor module in COMM mode, and enable the PA to give out a constant un-modulated RF signal that is fed into the load pull tuner in **Figure 20**. The load-pull tuner was tuned to different impedances to locate its impedance value at which the PA gave out maximum power [*65*], which was read off the series power meter as shown in **Figure 19**. The loss in the measurement setup i.e. the RF tuner, the -20dB coupler and the cables, was measured separately at each one of the three measurement frequencies and added to the power output measured with the power meter to get the optimum output power shown in **Table 3**. An Agilent E4438C VSG was used to generate the input RF signal, while the output power was measured using the Agilent E4419B RPM power meter. A portion of the output power was coupled to an Agilent E4404B spectrum analyzer to ensure that the power meter was measuring the output power at the correct output RF frequency. The load-pull tuner used was a Maury model 1643-N. The effects of the SMA connector, CPW feed, the series capacitor and bias circuitry were de-embedded at various points along the output of the circuit to determine the optimum impedance referenced at the IC output after accounting for the impedance of the bias circuit. The impedance of the bias circuit was determined by measuring the S-parameters of the RF choke and bias coupling capacitors from which their respective impedances were determined at 860, 904.4 and 925 MHz, that were then modeled in the bias circuitry using Agilent's Advanced Design System (ADS) software. The results of the Load-pull analysis are shown in **Table 3** [*10*].

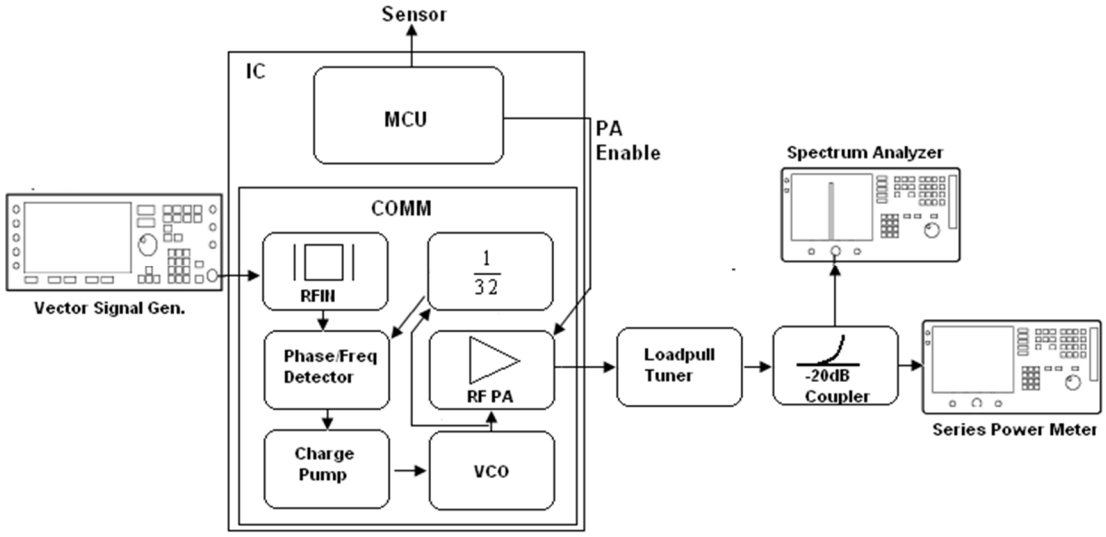

Figure 19. Measurement setup for Load-pull characterization of integrated Power Amplifier (PA).

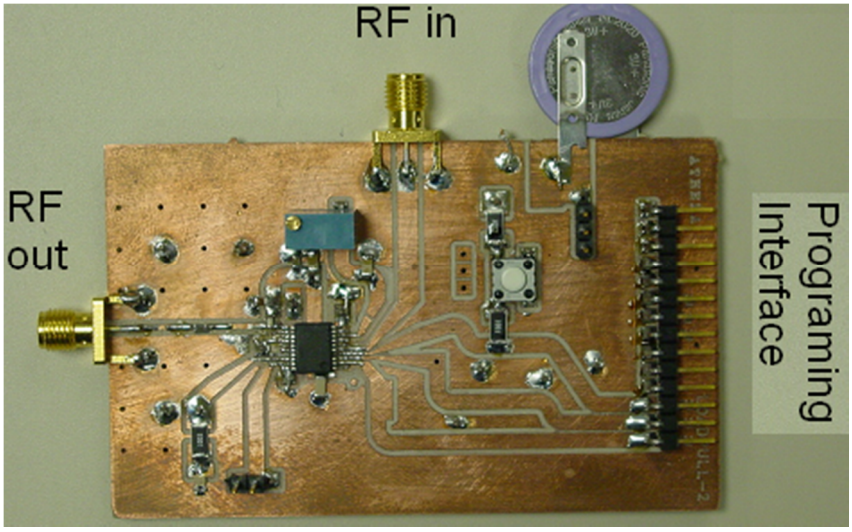

Figure 20. Prototyping Board for Load-pull analysis and in-circuit programming [*10*]**.**

Table 3. Load-Pull results of the RFPIC 12F675H Wireless Transmitter.

RF-IN Frequency	860 MHz	904.4 MHz	925 MHz
Z_{PA} (ohms)	275.9-j61.67	37.31+j65.96	32.1+j18.88
Output Power (Measured) (dBm)	6.1	7.43	7.72
Output Power (Manufacturer) (dBm)	7.5	7.5	7.5

A tapering, compact U-shaped, half-wavelength dipole antenna was designed with an impedance equal to the conjugate of the load-pull characterized optimum PA impedance at which the PA gave out maximum RF output power around a center resonating frequency of 904.4 MHz [*65*] [*10*]. The antenna and the wireless sensor module circuitry were printed on a single layer of organic photo-paper using the inkjet printing fabrication method outlined in the previous section. The wireless sensor circuitry was laid out in the space within the U-shaped dipole antenna to miniaturize the overall module size. The tapering width of the dipole arms help in increasing the impedance bandwidth of the antenna. Since metallic circuit traces of the wireless sensor module within half a wavelength of the dipole antenna causes a change in its mutual impedance, the antenna was optimized so that its impedance was still equal to the optimum PA plus bias circuit impedance conjugate (37.31-j65.96ohms) at 904.4 MHz with the circuitry connected to it within the space between its arms. RF chokes (L1, L2) were used at several points in the circuit to minimize RF signals, meant to travel between the antenna and PA, from creeping into the positive power supply trace of the battery that was used to bias the PA (antenna terminals) and power up the MCU as shown in **Figure 21**. An RF choke (L3) was placed between the RF crystal and the negative power supply of the battery to isolate it from RF signals from the antenna. The entire structure of the module including the antenna and the circuit

layout was built using Ansoft's HFSS 3-D EM solver, which was also used to optimize the antenna. Lumped RLC (Resistor /Inductor/ Capacitor) boundaries with values equal to the measured values of inductors L1, L2 and L3 at the 904.4 MHz were used to simulate the RF chokes in the circuit as shown in **Figure 21**. A lumped port was used as the RF power source in place of the PA to excite the antenna. The final dipole antenna design along with the circuit in between had a dimension of 9.5 by 5 sq. cm. The simulated return loss or S_{11} for the antenna with respect to the PA's optimum load impedance (37.31-j65.96 ohms) is shown in **Figure 22**, and shows a good impedance match at the design frequency of 904.4 MHz with a -10 dB bandwidth of 60 MHz. The maximum simulated directivity obtained was of 1.54 dB for the U-shaped dipole antenna with the wireless sensor circuitry in between. The final dipole based wireless sensor module prototype fabricated and assembled as per the steps outlined in the preceding section is shown in **Figure 23**. The simulated and measured dipole antenna radiation pattern is shown in **Figure 24** [*10*].

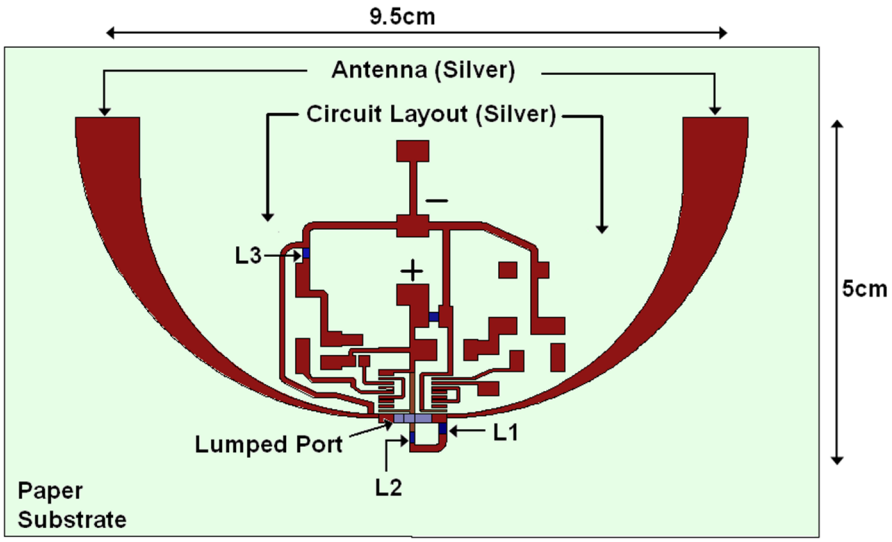

Figure 21. Inkjet Printed Dipole based wireless sensor module topology.

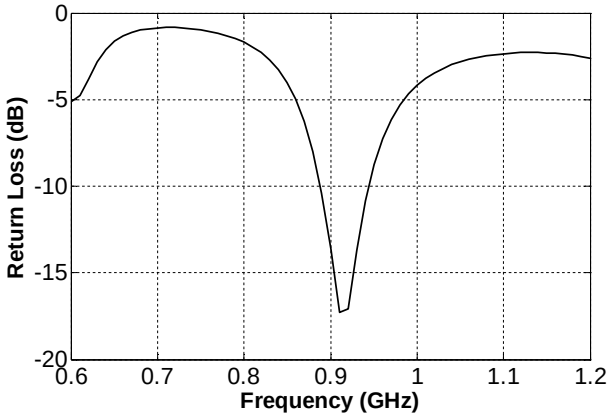

Figure 22. Simulated Return loss of the Dipole antenna with respect to the combined PA and Bias circuit impedance (37.31-j65.96ohms).

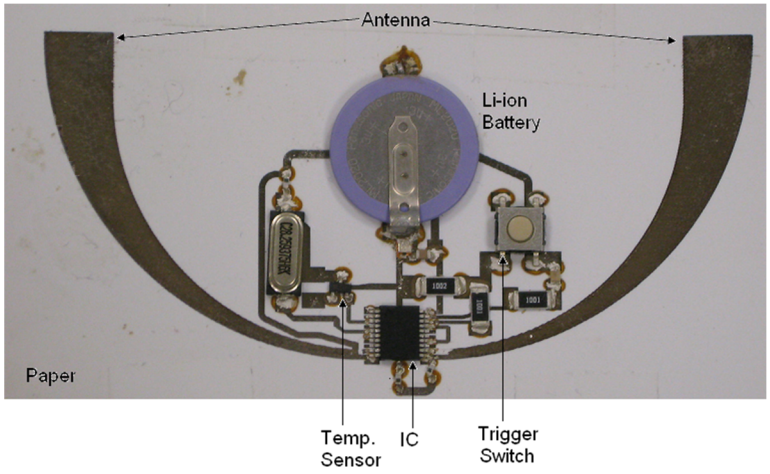

Figure 23. Inkjet Printed Dipole based wireless sensor module.

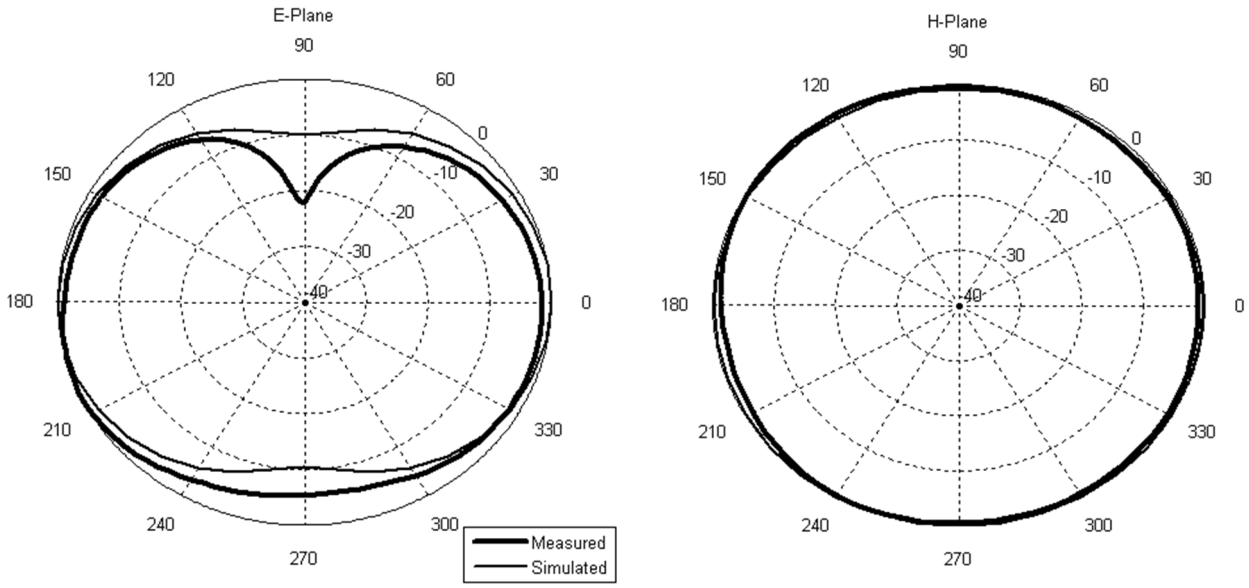

i ii

Figure 24. Normalized 2-D far field radiation plots of simulation and chamber measurement of inkjet-printed dipole based wireless sensor module in: (i) E-Plane (ii) H-Plane

Many of the drawbacks with the dipole based module can be eliminated by using a monopole based structure. The monopole uses its ground planes as a radiating surface, which can also be used to shield any circuitry behind it. The monopole antenna also does not require a differentially fed input signal like the dipole, which was ideal for the PA since its output was single-ended. The circuit for the monopole was laid out on 2 layers, which helped minimize the size of the circuit topology by avoiding the long power supply traces that had to be used on the single layer dipole based module. The top layer contained the printed antenna and most of the circuit components for the module. The bottom layer contained a Li-ion cell and the power supply traces, which were routed to the top layer through drilled vias. The monopole antenna had a planar coplanar waveguide (CPW-G)-fed wideband structure with a rectangular radiator to achieve a more compact and wideband design that could be easily printed [*67*] [*68*]. A CPW-G

i.e. CPW with a ground plane on the top and bottom layers is extremely suitable at shielding the antenna and the sensor data bus from interfering noise that may have coupled into the shared power supply traces in the bottom layer and also due to the digital switching within the MCU on the top layer [*69*] [23]. In addition, the CPW-G feed line could also allow a matching network to be implemented between the PA and antenna in the event of a possible mismatch between the two. The monopole based sensor module topology is shown in **Figure 25**.

The entire topology shown in Figure 25 was also simulated using Ansoft's HFSS 3D EM tool. Multipoint grounds for RF and low frequency signals were used for this design for better isolation between the digital switching occurring in the MCU and the RF transmission [*69*]. RF chokes (L1 and L2) simulated as lumped RLC boundaries were once again used to isolate the two signal grounds as shown in Figure 25. A lumped port was used as the RF source to replicate the PA for the simulation. The antenna was matched to an impedance of 60.1-j73.51 ohms ($Z_{L\text{-}opt}$), which is the reference at the PA output at the design frequency of 904.4 MHz. The simulated return loss for the entire structure showed good wideband resonance of about 220 MHz around the design frequency of 904.4 MHz as shown in **Figure 26**. The maximum simulated directivity obtained was 2.6 dB. The measured and simulated radiation patterns are shown in **Figure 27**.

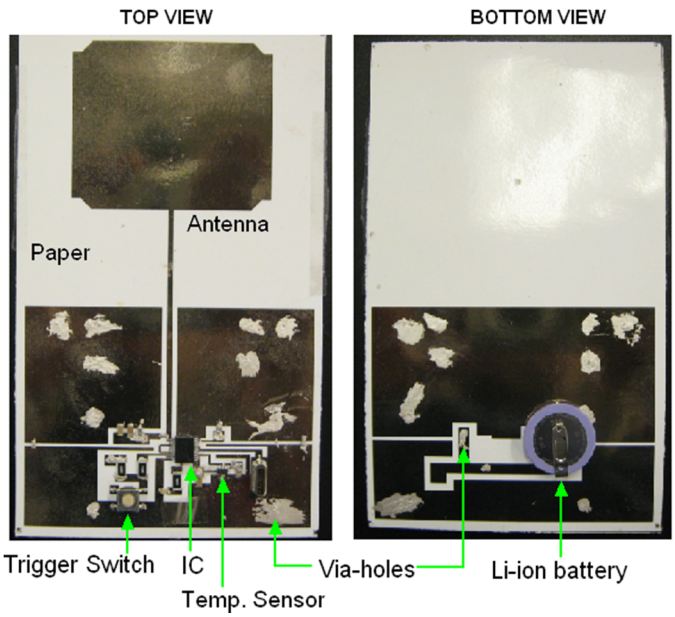

(i)

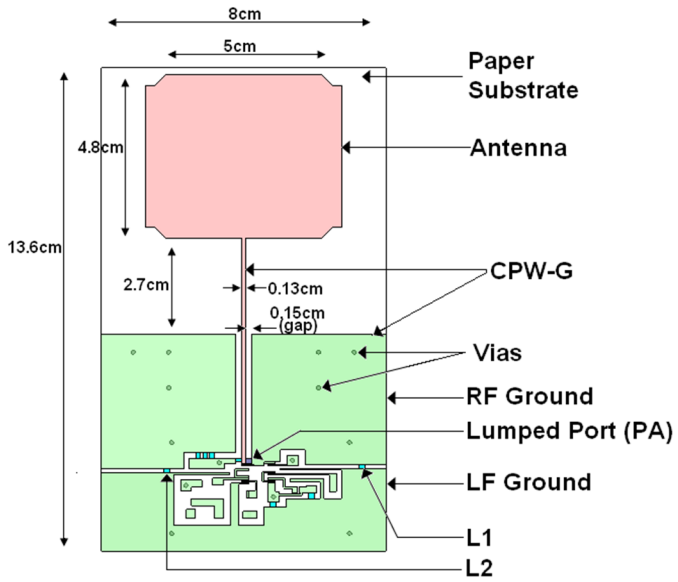

(ii)

Figure 25. Monopole based wireless sensor module (2 layer). [*10*]

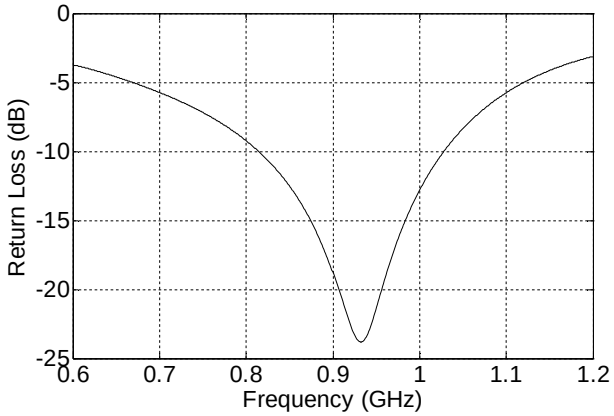

Figure 26. Simulated Return loss of the Monopole antenna connected to the circuit. [*10*]

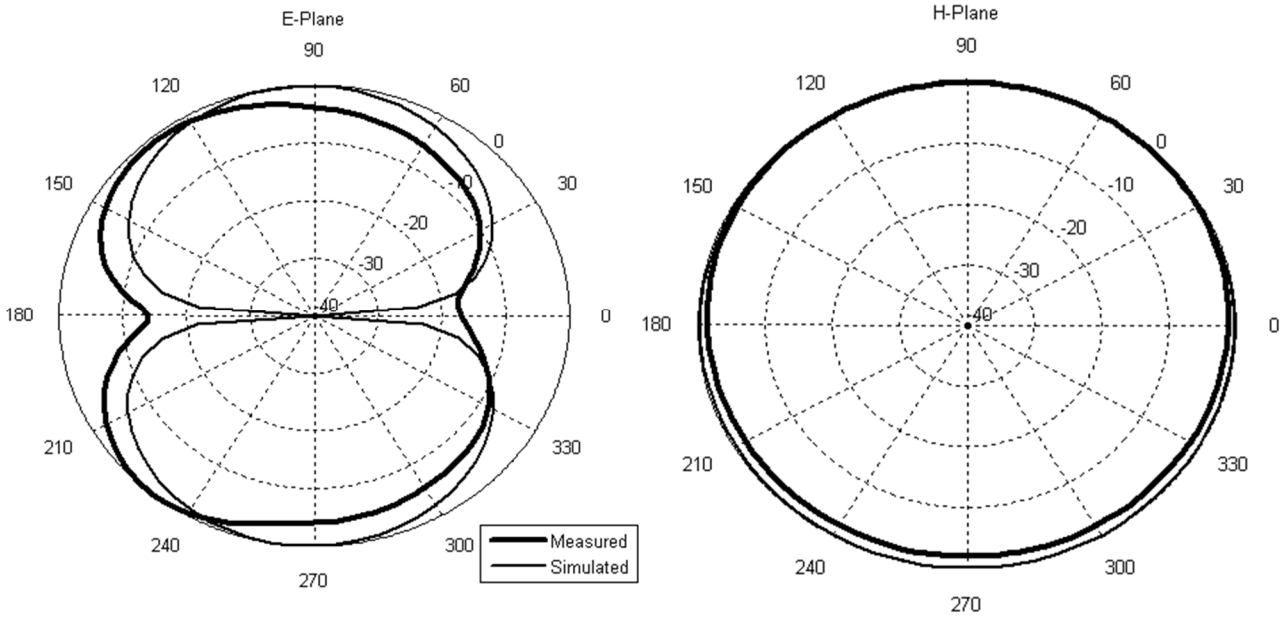

(i) (ii)

Figure 27. Normalized 2-D far field radiation plots of simulation and chamber measurement of inkjet-printed monopole based wireless sensor module in: (i) E-Plane (ii) H-Plane

Wireless link measurements were then performed with the assembled modules to verify their system level performance. The wireless link measurements were carried out by placing the modules at different temperatures within an oven or refrigerator, and triggering them to transmit in the SENSE mode. On the receiver side, the ASK modulated wireless sensor information was captured using a wideband AN-400 RFID reader antenna connected to a Tektronix RSA 3408A Real Time Spectrum Analyzer (RTSA). The transmitter was kept at a distance greater than its far-field boundary from the receiver. The far-field boundary of the dipole and monopole based modules were determined to be 3.8 and 5.4 cm using Fraunhofer's far-field equation shown in (15) below [*10*]. In (15), 'R' is the distance from the transmitter at which its far field region starts, D, is the largest dimension of the antenna and 'λ' is the free space wavelength at the transmit frequency of 904.4 MHz. The wireless sensor data captured by the RTSA were decoded and compared to the temperature obtained from a commercial, non-contact infrared thermometer. The results have been summarized in this section.

$$R = \frac{2D^2}{\lambda} \tag{15}$$

Improving the overlap of adjacently printed conductive layers and the matching in the dipole-based modules increases the overall gain significantly as shown in **Figure 28** (i) and (ii). The transmitted signal measured from the dipole based module sprayed with a 10pL volume was measured by the RTSA from a distance of 4.26 meters, and was observed to be -48.07 dBm. This transmitted signal obtained was significantly better than the -69 dBm that was measured from the dipole-based module that was sprayed with conductive ink using a 1pL spray volume [*10*] [*54*].

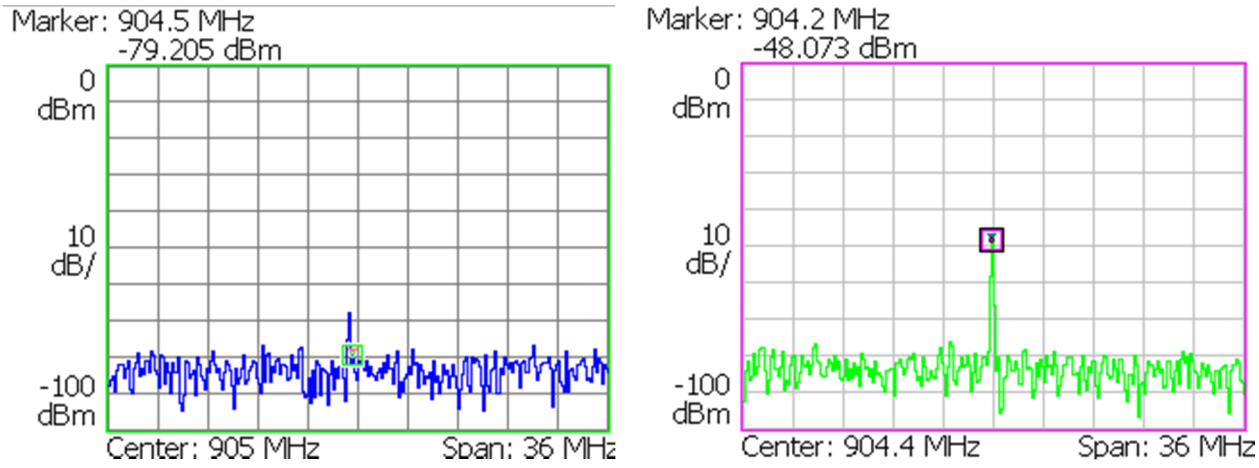

(i) (ii)

Figure 28. Real Time Spectrum Analyzer wireless link measurements of dipole-based module:
(i) RTSA measured ASK modulated signal for the Dipole-based module metallized using a 1pL spray volume. (Power vs. frequency). [*54*]
(ii) RTSA measured ASK modulated signal for the Dipole based module metallized using a 10pL spray volume from a distance of 4.26 meters. (Power vs. frequency). [*10*]

Efforts to ensure an impedance matching between the dipole and the RF PA with the circuit close to its feed, and reduce RF leakage from the RF to the non-RF digital side of the circuit, did improve the performance of the dipole based module. In addition the use of a low-precision high-volume cartridge to increase conductivity of the antenna structure also helped in increasing the amount of power being transmitter by over 20 dB from its predecessor with a simulated directivity of 1.54 dB.

By comparison, the monopole through the use of its grounded structure offered a significantly convenient way of integrating the antenna with the module circuitry with a better matching and isolation. The transmitted signal measured by the RTSA from the monopole-based module was observed to be -26 dBm at a frequency of 904.4 MHz, and is shown in **Figure 29**. The measured wireless signals from the monopole based module translates into a significantly

higher EIRP of 4.91 dBm, which also translates into a longer range compared to the dipole-based module as can be seen by the comparison in **Table 4** [*10*]. The monopole based structure also offered more wideband performance compared the dipole based module since the antenna is parasitically less immune to the effects of the wireless sensor circuit layout. The return losses of the dipole and monopole based modules are show in **Figure 22** and **Figure 26**. The -10 dB return loss of the monopole covers all three frequency bands, 860, 904.4 and 925 MHz at which the RF PA in the transmitter could optimally operate. The dipole bandwidth was limited to only frequencies at 904.4 and 925 MHz [*10*].

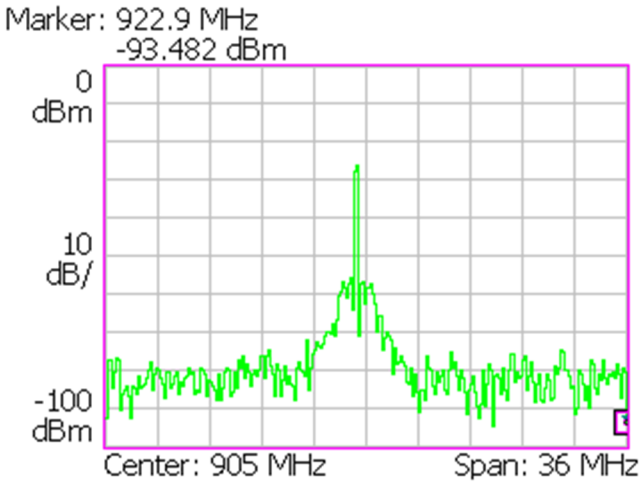

Figure 29. RTSA measured ASK modulated signal for the Monopole based module (Power vs. frequency).

In order to verify the correct operation of the sensors in the dipole and monopole-based wireless sensor modules, the modules were placed at different temperatures while triggered to operate in the SENSING mode. The ASK modulated sensor information sent out by the modules at different temperatures was measured by the RTSA in a power versus time plot, and is shown in **Figure 30** and **Figure 31** for the dipole and monopole based modules, respectively. The

transmitted sensor data shows good agreement with the measurements carried out with the digital infrared thermometer. The digital infrared thermometer has an accuracy of ±2.5 Degree Celsius and the TC1047A temperature sensor used in the modules has an accuracy of ±2 Degrees Celsius [31].

Table 4. Performance comparison between dipole and monopole-based wireless sensor modules.

		Dipole	Monopole
Layers		1	2
Resonant Frequency		904.2 MHz	904.4 MHz
-10 dB Return Loss Bandwidth		60 MHz	210 MHz
EIRP		-9.9 dBm	4.91 dBm
Range (Free Space Loss Model)	-65 dBm	15 m	82.6 m
	-85 dBm	150 m	826.6 m
	-95 dBm	475 m	2613.4 m
	-111 dBm	2995 m	-
Range (2-Ray Beam tracing model)	-65 dBm	25.32 m	51.1 m
	-85 dBm	80.1 m	161.5 m
	-95 dBm	142.36 m	287.3 m
	-111 dBm	357.65 m	722 m
Temperature Digital IR	-2 Deg. C	-	-1.75 Deg. C
	6.9 Deg. C	-	7.7 Deg. C
	19.8 Deg. C	-	20.5 Deg. C
	22.6 Deg. C	21	-
	28 Deg. C	-	28.85 Deg. C
	34 Deg. C	-	33.86 Deg. C
	42.4 Deg. C	-	44.15 Deg. C

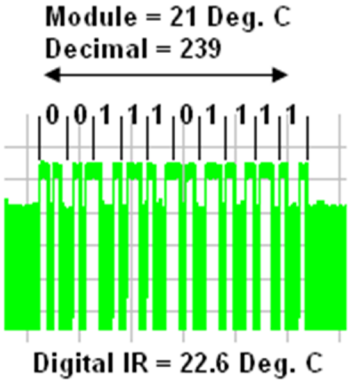

Figure 30. ASK modulated temperature sensor data captured by the RTSA at room temperature (Power vs. Time).

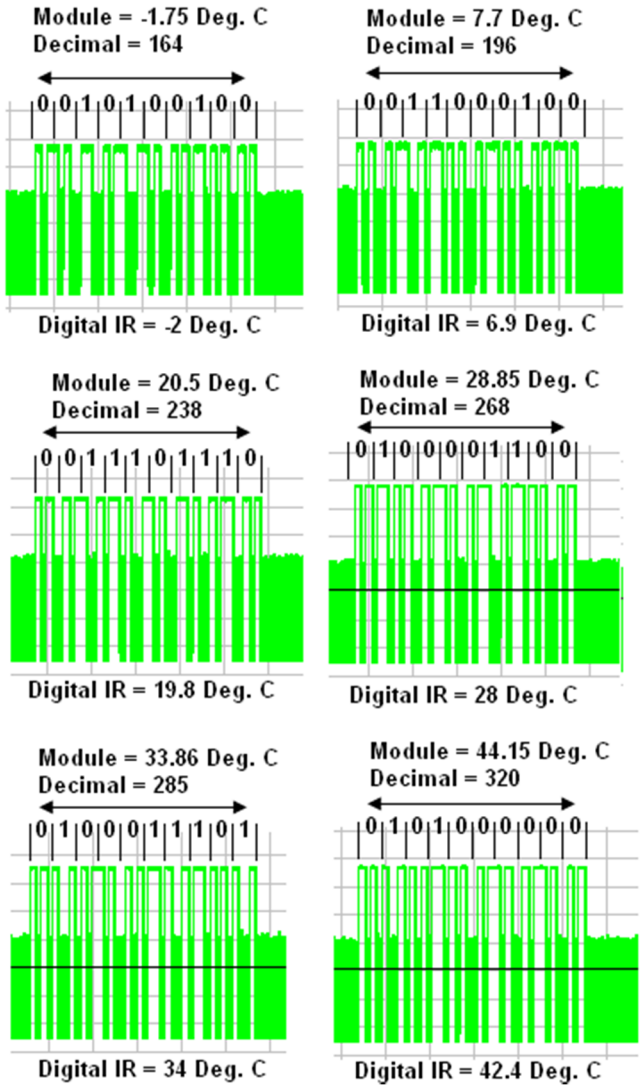

Figure 31. ASK modulated temperature sensor data captured by the RTSA from -2 to 42.4 Degrees C. (Power vs. Time).
Module: Sensed Temperature transmitted from module & captured by RTSA
Digital IR: Temperature measured by the Digital Infrared Thermometer

CHAPTER 4. BATTERY-LESS, SOLAR POWERED AND ACTIVATED, LONG-RANGE RFID TAG (SOLTAG) FOR REMOTE LOCALIZATION AND ITEM TRACKING APPLICATIONS

4.1 Localization Setup

Ambient solar and wireless energy harvesters offer the advantage of a more pervasive and perpetually-on power source compared to other energy harvesters. For daytime and outdoor operations, solar power offers higher power densities compared to other energy harvesters (see Table 1). Barcodes and conventional RFIDs that use ISO-18000 and ISO-15693 standards currently offer range of between 0.01 and 10 meters. By incorporating elements of energy harvesting and RFID-type communication, limitations in range of existing barcodes and RFID systems is overcome to offer a low-cost, RFID-type solution for vehicle tracking application. Use of solar power eliminates the need for periodic battery replacement, and provides the same range as active tags [*70*]. The use of RFID-like communication reduces the size of the solar cell, and the number of electronic components used as compared to conventional, solar-powered radios [*71*] [*72*]. The tracking system was designed to remotely track the position of a solar-powered, battery-less, semi-passive, RFID tag (SOLTAG) placed in vehicles using a lateration technique.

Lateration is the method of estimating the position of the SOLTAG through the relative comparison of the strength of the SOLTAG-transmitted signal, which is measured and recorded at three or more of the surrounding anchor points. The anchor points form a wireless sensor network (WSN) made up of Crossbow's MICA-2 wireless nodes (WSN motes) that are mounted on lamp posts at a height of 3.5 meters from the ground around the parking lot over which the position of the SOLTAG is triangulated. The distance of the SOLTAG from the surrounding

WSN motes is estimated using the received signal strength indicator (RSSI), which is integrated into the Texas Instruments cc-1000 transceivers in the WSN motes that are present within line of sight [*73*]. The RSSI recordings from the WSN motes are pooled together on a central computer using the mote's Wi-Fi interface, and selectively parsed and post processed to compute the SOLTAG's location. The position of the lampposts and parking spaces where the SOLTAG is remotely tracked is illustrated in Figure 32 and Figure 33. The size of the localization infrastructure is optimized to provide coverage over the entire parking lot shown in Figure 33 while at the same using as few WSN motes to reduce deployment costs [*74*] [*75*].

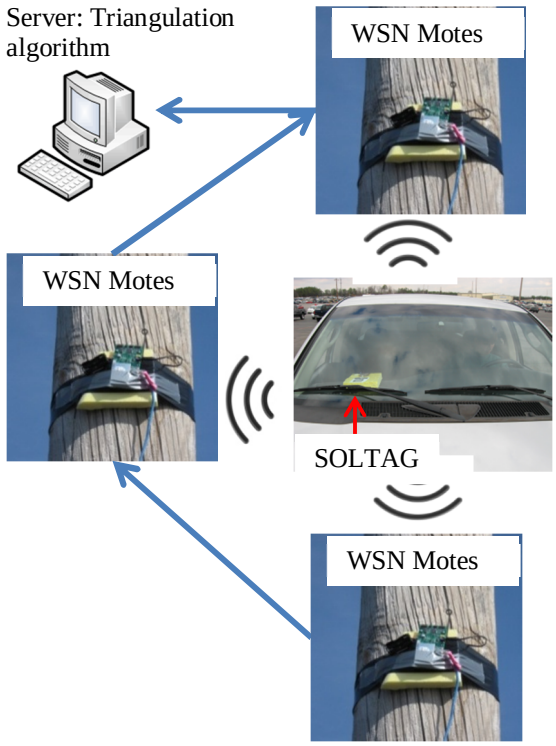

Figure 32. Localization setup for tracking of SOLTAGs in vehicle by three or more WSN motes mounted on lampposts.

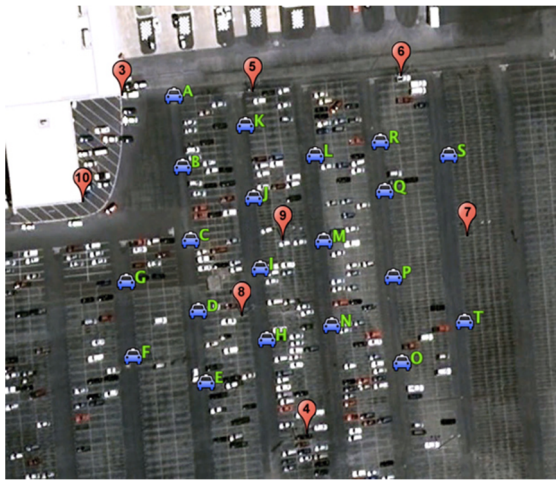

Figure 33. Localization coverage.
Red dots: Lamp posts mounted with WSN motes.
Blue dots: Vehicle position [*74*] [*75*]**.**

4.2 Localization requirements of SOLTAG System

The SOLTAG design is optimized to meet three requirements important for the intended localization application. The three requirements are low bill-of-material (BOM) costs; maximum number of broadcasts of the tag GUID to the surrounding WSNs per operating duty cycle; minimum time interval between consecutive broadcasts; and maximum range between the SOLTAG and the WSN infrastructure. The SOLTAG is designed using off-the-shelf discrete components as illustrated by the schematic and prototype in Figure 34 and Figure 35 [*74*] [*75*].

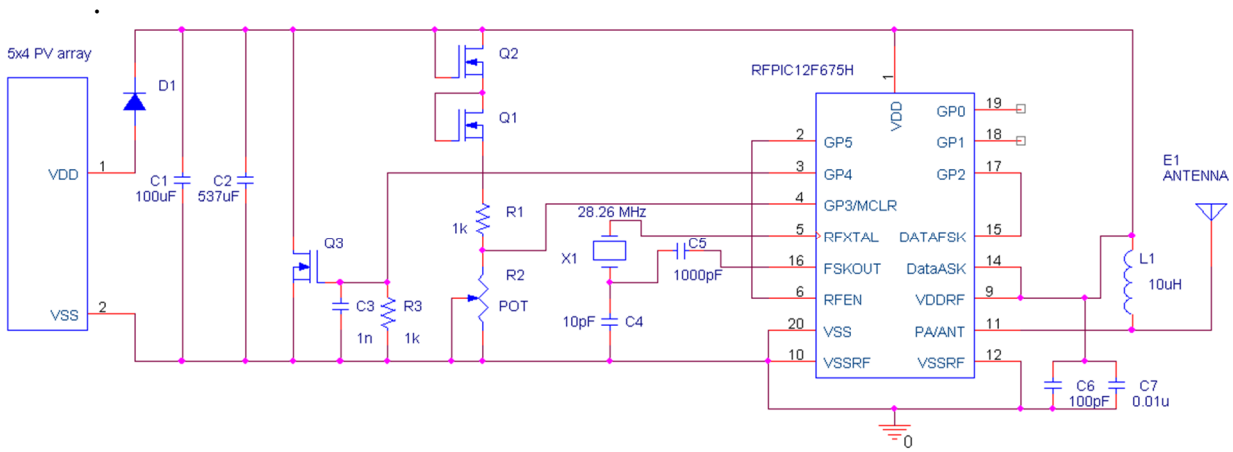

Figure 34. Circuit schematic of SOLTAG.

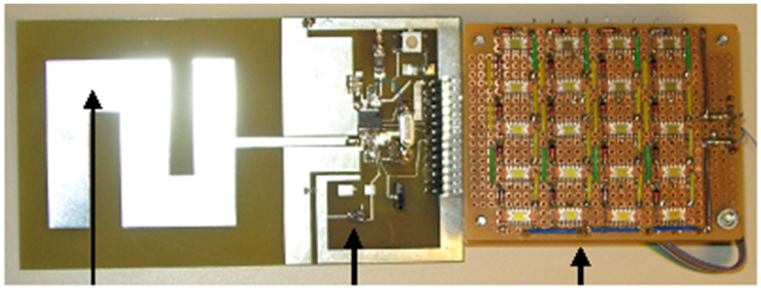

Figure 35. SOLTAG development prototype [*46*]**.**

The power source of the SOLTAG is an array of CPC1832 solar cells manufactured by IXSYS Semiconductors, which are connected in parallel to maximize current output. Each cell is capable of supplying 8V and 40 microamperes of current under light intensities of 4000 lux into the charge-tank capacitors connected in parallel (C1 and C2) [*74*] [*75*] [*76*] [*77*]. With measured light intensities of between 4,000 and 60,000 lux in Atlanta, the solar cell array ensured enough supply to charge the 637 µF charge tank to over 3V, and supply the 0.6 microamperes of leakage current consumed by the RFPIC12F675H microcontroller/transmitter chip in SLEEP or CHARGE mode [*76*] [*62*]. The charge in the charge tank is stored for later use during the TRANSMIT mode when the SOLTAG is communicating with the WSN motes.

The power management unit (PMU) of the SOLTAG comprises of the RFPIC's firmware, discrete mosfets (Q1, Q2 and Q3), and resistors (R1 and R2). The PMU controls the charging and discharging of the charge-tank voltage to between 1.8V and 3.8V, which is the operating voltage range of the RFPIC. When the charge tanks (C1 and C2) charge up to 3.8V using solar power, the mosfets (Q1 and Q2), and resistors (R1 and R2) trigger an external interrupt in the RFPIC's firmware. The external interrupt wakes up the RFPIC's microcontroller core (MCU) from SLEEP/CHARGE mode into ACTIVE/DISCHARGE mode. In ACTIVE/DISHARGE mode, the RFPIC's MCU enables the RFPIC's built-in wireless transmitter by pulling the input 'RFEN' high, which powers on the built-in phase-locked-loop (PLL), and RF Power amplifier (PA) (see Figure 34). After idling for 600 microseconds to allow the external crystal oscillator (X1) and the PLL to lock to an output frequency of 904.4 MHz, the SOLTAG communicates with the WSN motes using frequency-shift- key modulation (FSK) and Manchester encoding of the broadcasted data bits. The transmitted RF output is modulated using FSK by loading the PLL's input crystal with extra capacitance of 1000 pF (C5) through the

'FSKOUT' pin that causes the crystal's resonance of 28.259375 MHz to shift by 15.60 kHz. This shift is multiplied by a factor of 32 through the PLL to produce an output shift of close to 500 kHz from a transmit frequency of 904.4 MHz only when the 'DATAFSK' pin is modulated by the RFPIC's MCU (see Figure 34). The optimum values for 'C4' and 'C5' are determined to be 10 and 1000 pF, respectively, through empirical measurements, which tunes the PLL to align the SOLTAG's modulation profile closely to the TI cc1000 receiver in the WSN motes (see Figure 36) [*74*] [*75*] [*76*]. The identical modulation profiles reduce the number of needed preamble bits, and wireless data packets that are dropped during communication between the SOLTAG and the WSN motes per ACTIVE/DISCHARGE cycle [*74*] [*75*] [*76*].

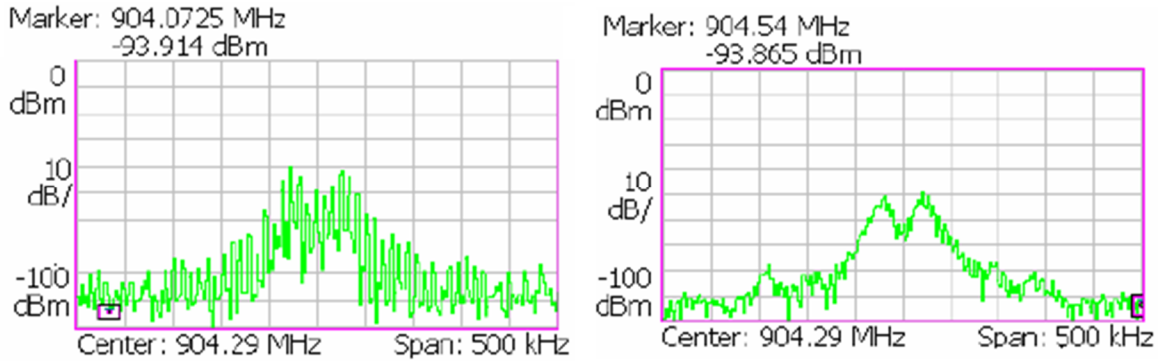

(i) (ii)

Figure 36. (i) Real time spectrum analyzer (RTSA) captured FSK modulation profile of SOLTAG. (ii) RTSA captured FSK modulation profile of WSN TI cc1000 motes [*74*] [*75*] [*76*]**.**

4.3 SOLTAG Wireless Power Amplifier (PA) and Antenna Design

Optimizing the performance of the integrated wireless power amplifier (PA) of the RFPIC and antenna in the SOLTAG for power efficiency is critical for maximizing range of the SOLTAG to the WSN motes, which reduces the size and cost of the WSN infrastructure. As the most power hungry component of the SOLTAG, the PA's efficiency also determines the number

of packets that can be transmitted per duty cycle or per charge tank discharge of the SOLTAG. The optimum impedance looking out of the PA in the RFPIC12F675H for which the PA gives out maximum RF output power is determined using load-pull analysis. For a transmit frequency of 904.4 MHz, the PA gives out maximum power of 4.5dBm with an output impedance (Z_{PA}^{*}) of 37.31-j65.96 Ω [*75*] [*76*] with the bias circuitry included. To ensure that the bulk of the PA's output power is radiated out with maximum efficiency, a conjugately matched monopole antenna is designed and optimized for the SOLTAG using Ansoft's High Frequency Structure simulator (HFSS). The antenna's simulated gain, measured resistance and reactance are shown in **Figure 37** (i), (ii) and (iii), respectively.

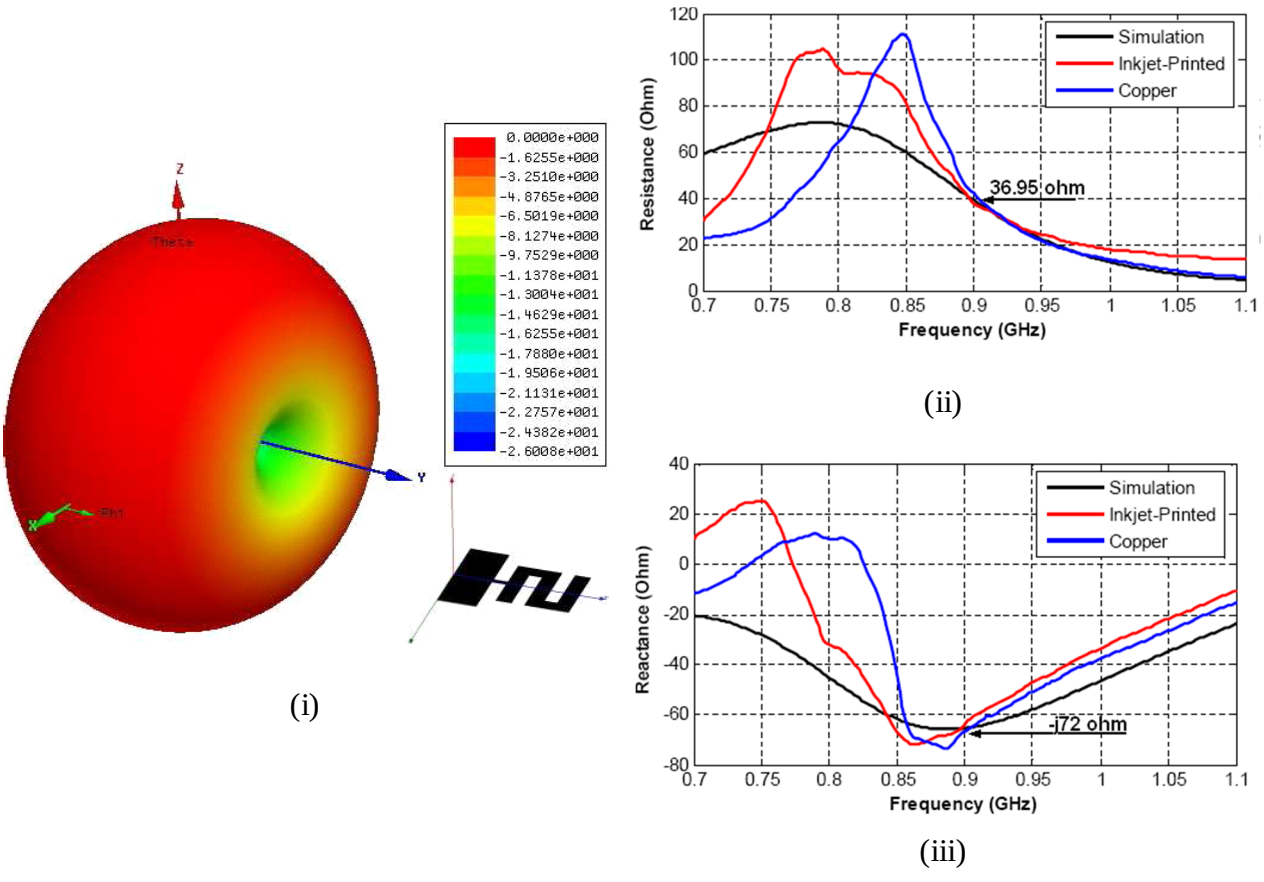

(i)

(ii)

(iii)

Figure 37. SOLTAG antenna parameters [*75*]**. (i) Simulated antenna radiation pattern in HFSS. (ii) Measured antenna resistance. (iii) Measured antenna reactance.**

Monopoles use a single ended ground feed, which offers electromagnetic shielding against metallic objects in the vehicle and electronic components including the solar cell array mounted behind the ground plane. In addition, monopoles have a wide input bandwidth and an omni-directional radiation pattern in the H-plane, which is useful for the tag's triangulation by the WSN [*78*]. The proposed monopole antenna design is fabricated on FR-4 ceramic substrate, and also a paper based substrate using inkjet-printed technology as shown in **Figure 35** [*75*] [*10*]. The antenna has measured impedance (Z_{ANT}) of 36.95-j72 ohms, which results in 95% of PA output power to be transmitted through the antenna as determined by the power transfer co-efficient (τ) using (16) and (17).

$$\Gamma = \frac{Z_{ANT} - Z_{PA}^*}{Z_{ANT} + Z_{PA}^*} \tag{16}$$

$$\tau = 1 - |\Gamma|^2 \tag{17}$$

The peak current consumed by the SOLTAG's wireless front-end during the wireless transmission to the WSN is between 15.37 and 15.65 mA, which exceeds the solar cell supply. The extra charge is supplied by the charge tank capacitor, which discharges in the process of supplying power to the SOLTAG's power load of 194 ohms (R) for limited duty cycle. The transmitting duty cycle of the SOLTAG for the 637 µF charge tank (C_{TANK}) as it discharges from 3.8V to the turn off voltage of the RFPIC's optimized wireless front end voltage of 2.7V is determined to be 42.23ms using (18) [*76*].

$$T_{XMIT} = -\ln\left(\frac{V_{OFF}}{V_{TH}}\right)(R \times C_{TANK}) \tag{18}$$

The solar powered transmission profile of the SOLTAG is tested in the lab using a wide-spectrum halogen lamp to emulate daylight as shown in **Figure 38**. The wireless transmit time of the SOLTAG per operating duty cycle for the 637 µF charge tank is measured using a Tektronics RSA30408A real time spectrum analyzer (RTSA), and shows a close to predicted transmit time of 43.25ms as shown in **Figure 39**.

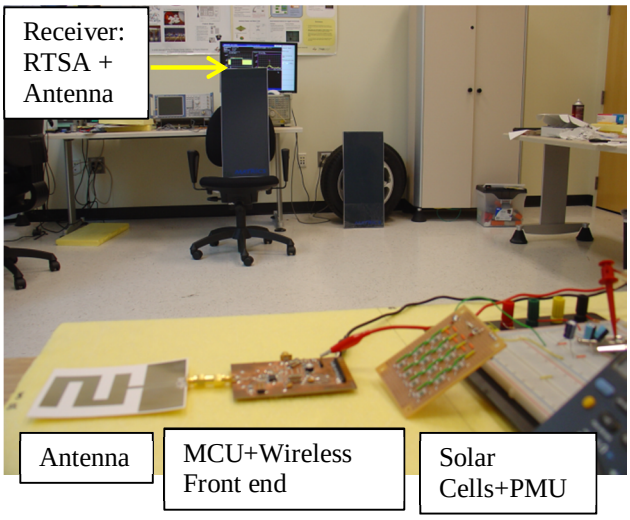

Figure 38. Wireless transmission profile test of SOLTAG.

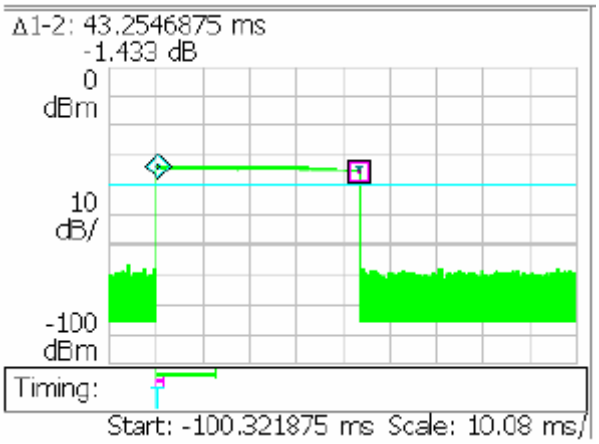

Figure 39. Un-modulated wireless transmission profile of SOLTAG captured by real time spectrum analyzer in power versus time plot [*75*] [*76*]**.**

The RFPIC's MCU is programmed to frequency modulate (FSK) the transmitter by toggling the transmitter's DATAFSK input in sequence with the desired wireless data packets recognizable by the WSN motes, which comprises of PREAMBLE, SYNC, ADDR, TYPE, GROUP, LENGTH, DATA and CRC fields. The first two fields are used for synchronization of the receiver's clock to the incoming bit rate, and the Cyclic Redundancy Check fields help eliminate bit errors occurring within the sent bit sequence by successfully recognizing a

corrupted packet and discarding it [*75*]. The Data bits of the packets convey the tag identification of the SOLTAG in order to help the WSNs distinguish between one or more of the SOLTAGS. The wireless data sequence sent out by the SOLTAG as measured by the RTSA is shown in **Figure 40**. The time to transmit one set of data packets is about 9 milliseconds, which given the total transmit time available for a charge tank capacitance of 637 µF (43.23 milliseconds) allows for transmission of three set of data packets per energy duty cycle.

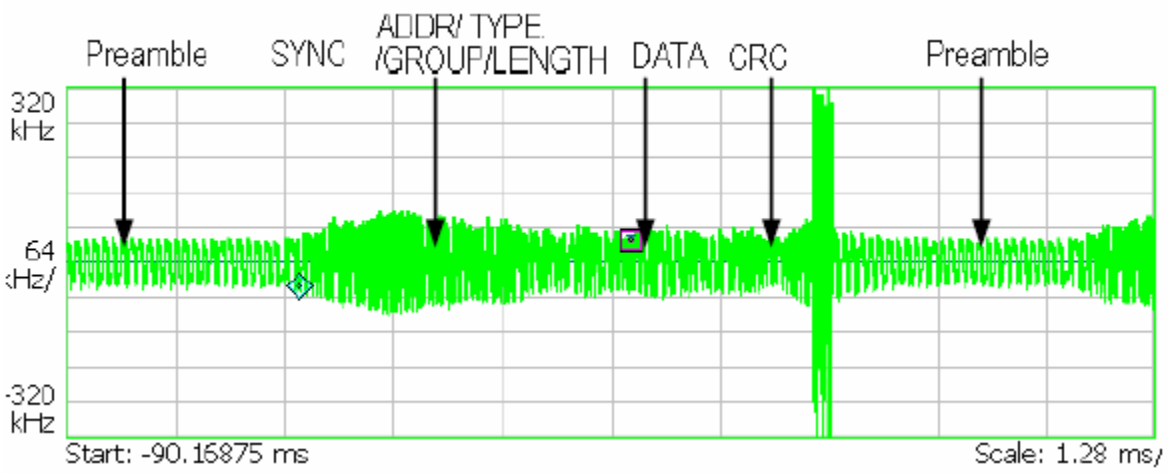

Figure 40. RTSA measurement showing wireless data sequence (RFID) sent out by SOLTAG [*75*] [*76*]**.**

The time interval between adjacent transmits for different light intensities in Atlanta is measured by observing the MCU controlled charge tank voltage in SLEEP/CHARGE and ACTIVE/DISCHARGE modes as shown in Figure 41 [*76*]. Transmit time intervals vary from 1.4 seconds on a sunny day with 70 kilo-lux of light intensity to 4.4 sec on a cloudy day with 10.5 kilo-lux of light intensity as verified by the SOLTAG's performance with a Mastech light intensity Lux meter [*79*].

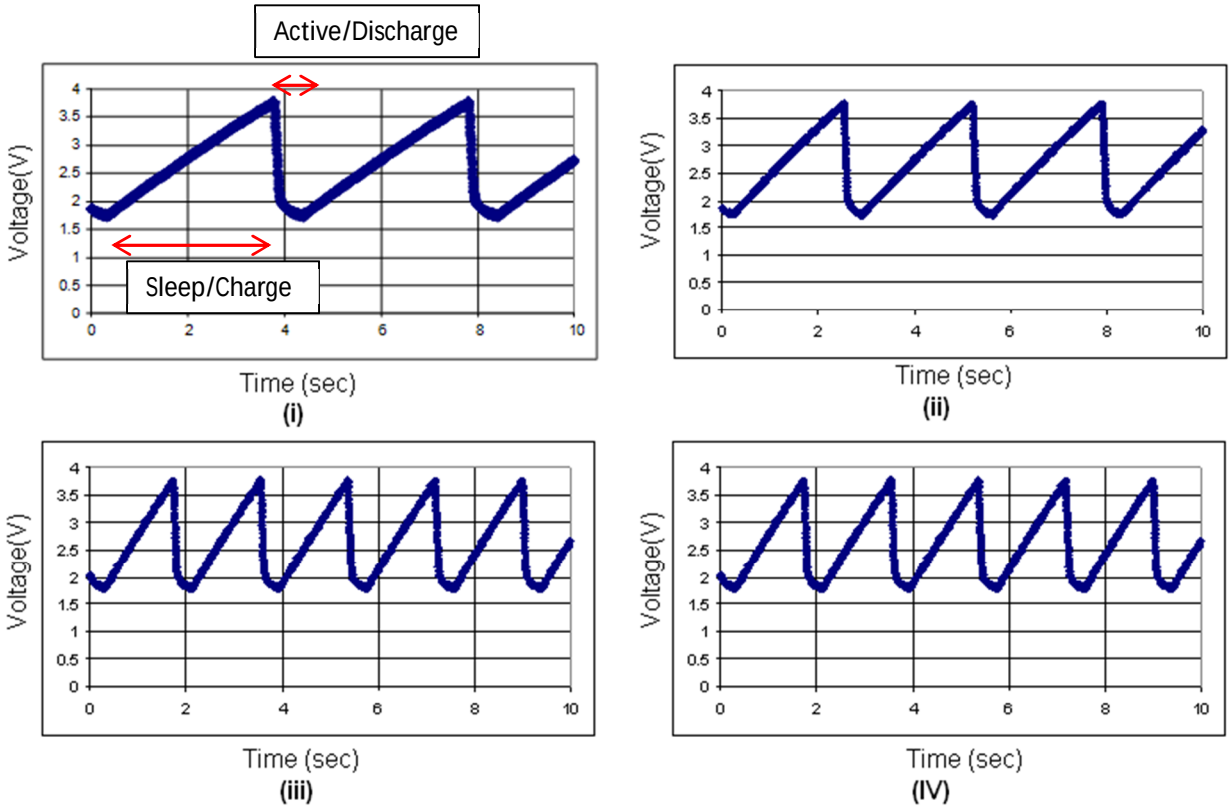

Figure 41. PMU controlled charge tank voltages for different light intensities in Atlanta, Georgia.

(i) 10.5 kLux; Transmit time interval =4.4 sec.
(ii) 20 kLux; Transmit time interval =2.7 sec.
(iii) 50 kLux; Transmit time interval =1.8 sec.
(iv) 70 kLux; Transmit time interval =1.4 sec.

4.4 Localization Results

Once successful link between the SOLTAG and WSN motes is established in the lab, the SOLTAG was put to test in the field to evaluate its performance for the end localization application. The SOLTAG's GUID identification number that allows the WSN infrastructure to identify different tags is extracted from the received wireless data sequence and time stamped by all the WSN motes within the SOLTAG's range. The SOLTAG GUID and RSSI along with the WSN mote's tower identification number are pooled together onto a central server into an SQLITE database where it is filtered and trilateration is performed based on the RSSI readings and prior knowledge about the WSN antenna gain and positions shown in **Figure 33** [*80*]. The range of the SOLTAG from the WSN motes for the trilateration is estimated using a two ray beam tracing model. The estimates that are then averaged for the WSN motes in range of the SOLTAG and displayed on a WGS 84 latitude-longitude coordinate system on Google Earth [*81*] [*82*]. The diameter of the area covered by the overall topology is around 190 meters, and the radius of the area covered by each WSN mote is 90 meters based on the SOLTAG design. An example of the localization estimate returned in Google Earth and compared to its real placement is shown in **Figure 42**. The mean, maximum and minimum estimate errors are summarized in Table 2. It is worth noting that, the average error is within a few car lengths when the SOLTAG is located in an area around the center of the topology. The location estimate error increases as the transmitter moves near the periphery or outside of the topology where optimal coverage by multiple anchor nodes in the WSN is not provided. This latter value is not been taken into consideration as the SOLTAG will always be considered to move in an area optimally RF covered by the WSN.

(i) (ii)

Figure 42. End result showing actual position of SOLTAG (blue car) with respect to the Trilateration (localization) estimate (red dot) for 2 instances [*75*]**.**

Table 5. Localization results summary [*75*]**.**

mean value	38.56m	
max value	95.9m	for O
min value	1.62m	for G
mean value of green	24.52m	those in middle of topology
mean value of red	51.98m	those in periphery or further of topology

CHAPTER 5. PROPOSED RESEARCH: AN EMBEDDED, WIRELESS-ENERGY-HARVESTING PLATFORM FOR POWERING ON SENSORS USING AMBIENT TV SIGNALS PRESENT IN THE AIR

While Solar power offers higher power density compared to other energy harvesting sources, solar intensity tends to be low or absent in areas shaded from the sun, or at night (see Table 1). Several machine-to-machine (M2M) and sensor applications related to monitoring of structural health, environmental sensing, agriculture and ambient intelligence require M2M and sensor motes to be deployed in places outside of direct sunlight, such as in building structures or beneath the top soil in farms. Depending on the frequency of wireless propagation, power supplied wirelessly can be used as a non-invasive power source for some of the M2M and sensor applications even with low power densities. In this section, an embedded, wireless, energy-harvesting platform (E-WEHP), which can sustain M2M and sensor application using power contained in ambient TV signals without batteries is described.

5.1 Ambient Wireless Radiation Measurements

In order to quantify wireless energy present in the air, wireless radiation around downtown Tokyo and Atlanta were measured using a NARDA SRM-3000 radiation meter [*83*]. Ambient radiation measurements showing the frequency bands occupied by digital TV in downtown Tokyo and midtown Atlanta are illustrated in **Figure 43** (i) and (ii), respectively. Radiation measurements carried out in Tokyo city show electric fields in air in the 80-100 MHz and 200-700 MHz frequency bands due to FM-radio and TV-signal broadcasts, respectively. By comparison, radiation measurements in Atlanta show radiation peaks in the sub-100 MHz range due to FM radio and AM radio broadcasts and in the 200 MHz range due to VHF mobile-radios

used for weather forecasts and air-traffic control. A closer analysis of both the spectrum measurements show significant amount of wireless radiation present in the 500-700 MHz band due to modern digital TV wireless broadcasts that are deployed in most urban places around the world since the year 2000.

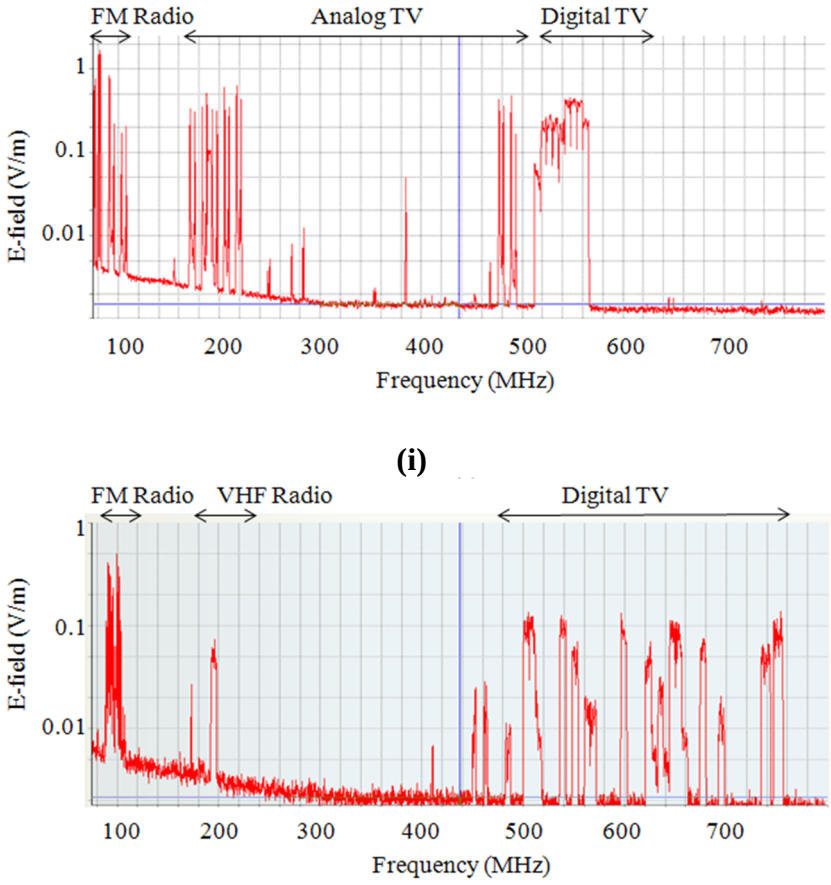

Figure 43. (i) Magnitude of ambient electric-field measured in downtown Tokyo. (ii) Magnitude of ambient electric-field measured in midtown Atlanta.

Ultra-high-frequency (UHF) bands offer better propagation characteristics while traversing through the air, and through physical obstacles such as trees and buildings. Incident electric-fields in the UHF bands also have free-space wavelengths between 42.3 and 60 cm,

which make it possible to efficiently capture them with antennas that are more compact than antennas designed for FM and AM radio frequencies.

5.2 Analog versus Digital TV Broadcasts

The spectrum in **Figure 43** (i) from downtown Tokyo shows both analog and digital TV-signals in the air between 200 and 400 MHz and between 500 and 600 MHz, respectively. Analog TV-signals have largely been phased out in most of North America as can be seen in the spectrum from downtown Atlanta in **Figure 43** (ii). Analog TV is a remnant from the late 1940s when analog TV standards such as the National Television System Committee (NTSC) were used in the US and Japan, and Phase Alternating Line (PAL) were used in most of Europe and around the world to transmit video and audio. Analog TV signals used a single 6MHz channel to transmit only once carrier and its subcarrier as shown in **Figure 44** (i), which rendered them spectrally inefficient allowing for a TV viewing resolution of only 640 by 483 pixels [*84*]. By comparison digital TV uses the same 6 MHz bandwidth to send out much higher data-payloads required by High-Definition-TV content (HDTV). Digital TV achieves this by digitally compressing and transmitting its data over multiple carriers within the same bandwidths. Rather than carry video signals at higher power levels and over single carrier frequency bands as was the case with the previous NTSC/PAL standards, digital streams are sent at digitally modulated, closely spaced carrier frequencies for digital video broadcasts [*85*] [*86*].

In Japan, digital TV is sent out wirelessly using the Integrated Services Digital Broadcasting standard for terrestrial TV (ISDB-T). Under ISDB-T standards, high definition TV content is broadcasted wirelessly using 6 MHz wide channels between in the frequency bands between 470 and 700 MHz. Each 6MHz channel has 5617 carriers at 0.99206 kHz frequency

spacing each of which carry video and audio data using 64 Quadrature Amplitude modulation (64-QAM) and Quadrature Phase shift keying modulation (QPSK) as shown in **Figure 44** (ii). Using spectrally efficient multi-carriers within each 6 MHz channel allows ISDB-T TV receivers to display 1080p resolution video and audio using MPEG-2 coding over the air. Data rates of roughly between 2 to 8 Mbits per second are supported for each of the 13 segments that make up each 6MHz channels [*85*]. By comparison, in the US digital TV signals are sent out wirelessly using the Advanced Television Systems Committee standard (ATSC). Using MPEG-II compression and 8-VSB RF modulation nearly 7 times as many pixels as NTSC can be broadcasted in a single 6MHz channel at rates of 1GB/sec [*86*].

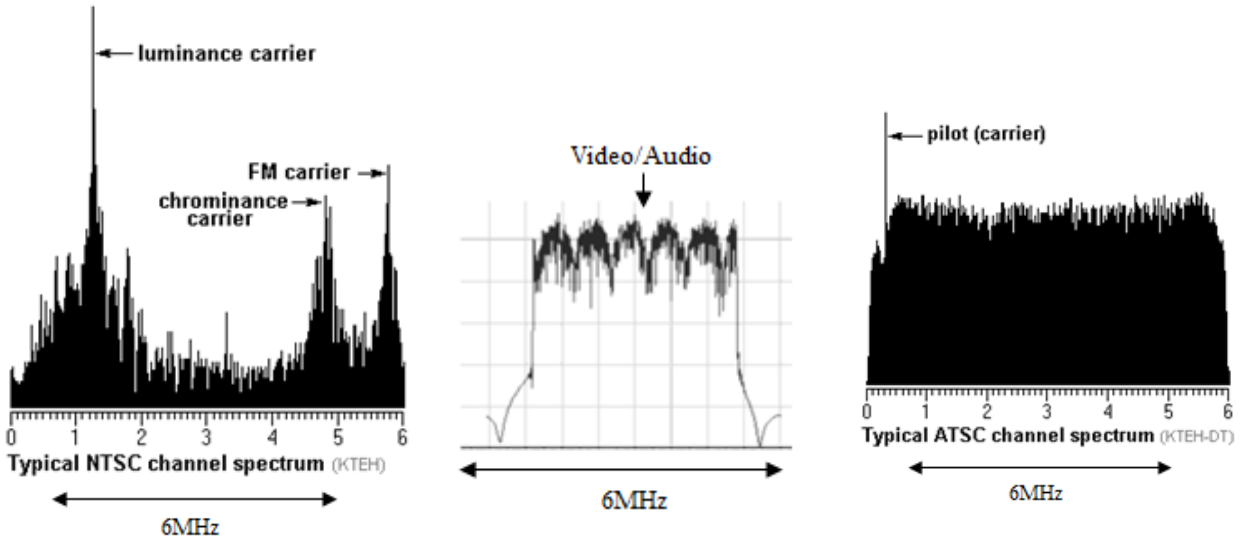

(i) (ii) (iii)

Figure 44. Frequency Channel Spectrums for (i)NTSC (ii) ISDB-T (iii) ATSC.

For wireless digital-TV-signals the power is not contained in a single carrier as is the case for analog TV but over many carriers that are present in a 6 MHz channel. The power in the band or channel is characterized by is given by (19), where X is the input power spectrum from a specified band, 'fl' is the low bound of the frequency band, and 'fn' is the high bound of the frequency band. [*87*]

$$P_{CHANNEL} = \sum_{f1}^{fn} X(f) \tag{19}$$

Figure 45 shows the wireless digital TV spectrum in Midtown Atlanta as measured by a Tektronics RSA 30408A real-time-spectrum analyzer connected with a matched ultra-wideband antenna array covered in the next section. While the peak carrier levels of the TV signals are only up to -30 dBm (1µW) or less, the aggregate of the power contained in all the carriers in about 16 TV channels add up to -8.95dBm (127.4 µW) due to the multi-carrier make up of Digital TV channels. Also all sixteen of the Digital TV signals were observed to be continuously on with respect to time as can be observed by the spectrogram shown in **Figure 45**, which is an advantage compared to harvesting power from cellular signals that vary with respect to location and the number of cellular users in a given cell. The multi-spectral nature of wireless digital TV signals and their perpetually on nature make them an ideal source of wireless power in urban areas.

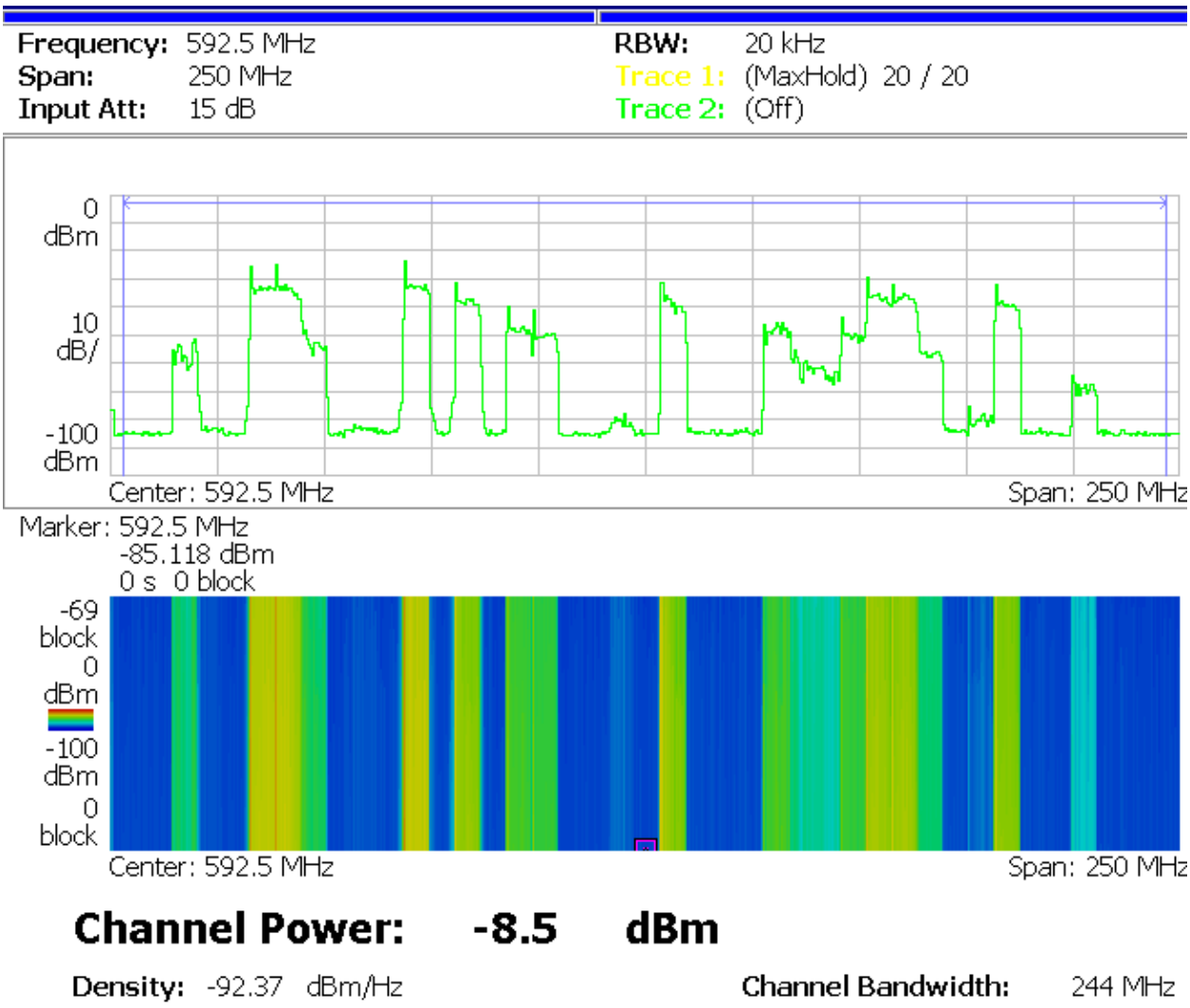

Figure 45. Wireless Digital TV spectrum in Midtown Atlanta within frequency band 500-700 MHz.

5.3 E-WEHP: Embedded Wireless-Energy-Harvesting Platform System

An embedded, wireless-energy-harvesting platform (E-WEHP) to harvest power from multi-carrier wireless digital TV signals is shown in **Figure 46**. The platform comprises of an optimized antenna to transduce the wireless radiation into an RF signal; a matched RF-DC charge-pump circuit to step up and rectify the low RF signal induced across the antenna into a usable DC form; a low leakage capacitor for use as a charge-tank to store the harvested wireless power; and a low power 16-bit microcontroller to manage the charge stored across the charge tank, and for interfacing with any sensor or M2M device.

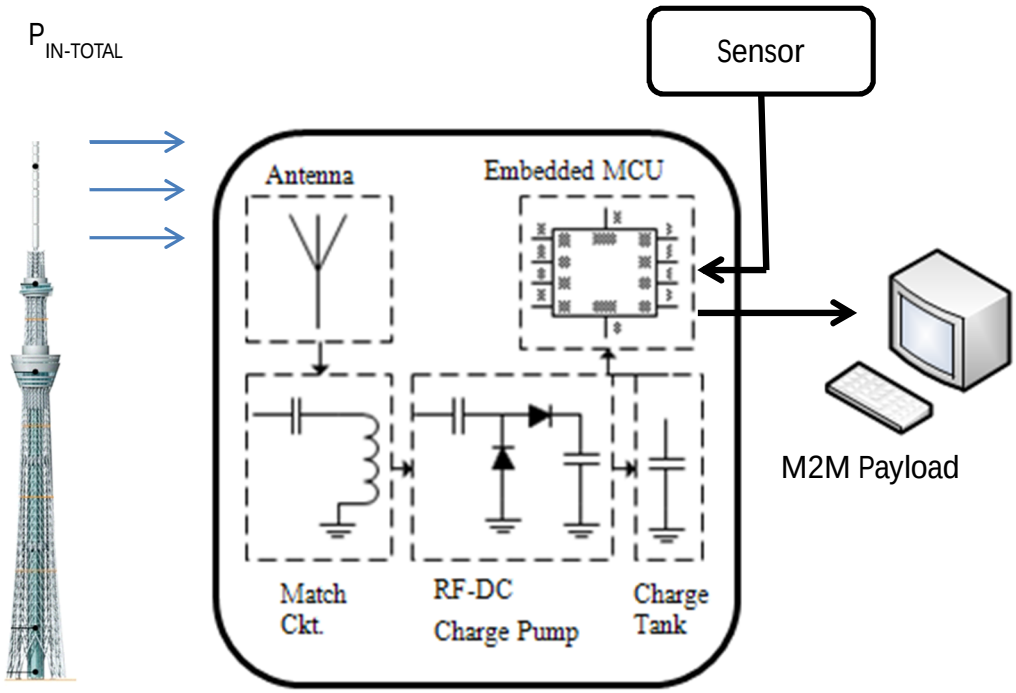

Figure 46. Embedded Wireless Energy Harvesting Platform to harvest power from wireless, digital-TV signals.

The amount of wireless radiation transduced into an electrical signal by the E-WEHP is a function of its antenna's aperture area (A_E). The antenna's aperture area is a function of the antenna's orientation with respect to the incident electric-field, the antenna's gain (G), the return loss between the antenna and the RF-DC converter (S_{11}), and the wavelength of the incident field (λ). The return-loss is a function of the field's carrier-frequency (f), and the voltage across the charge-tank capacitor (V_{CAP}). The wavelength of the incident field is a function of the field's frequency, and speed of propagation through the air (v_C). The wireless power ($P_{1\text{-}TONE}$) captured by the antenna from each tone or carrier present in TV signals is a product of the antenna's aperture area, the power density of the incident field (E), and the field's wave-impedance through the air (Z_{air}), which is determined using (20) [*88*]. Digital TV signals use ISDB-T standard where the power is present not just at one frequency but in each of the 5617 carriers that make up each of the 6 MHz channels present in the air [*84*] [*89*] .

$$P_{1-TONE} = \frac{|\overline{E_\theta}(f)|^2}{Z_{air}}.G(f).(1-|S_{11}(f,V_{CAP})|^2).\frac{(\lambda(f))^2}{4.\pi} \tag{20}$$

The total wireless power across an antenna tuned to digital TV channel frequencies (P_{TOTAL}) is hence an aggregate of the combined power present in each of the carrier frequencies (f_1 to f_N) in as many TV channels (c_1 to c_N) in the digital TV bands that is calculated using (21). The E-WEHP is optimized to capture wireless TV power across multiple such channels for operation at long range from the TV broadcast source. Maximizing the E-WEHP's response across the entire digital TV bandwidth in the 500-700 MHz UHF range as opposed to a single frequency or carrier in it is critical for operability at long distances from TV broadcasting sources. The long range operability of the E-WEHP is feasible because the number of carriers

across multiple such TV channels stays constant even though power levels of the subcarriers fade with an inverse square relationship to the distance between the E-WEHP and the TV broadcasting towers.

$$P_{TOTAL} = \sum_{C_1}^{C_N} \int_{f1}^{fN} \left[\frac{|\overline{E_\theta}(f)|^2}{Z_{air}} . G(f) . \ (1 - |S_{11}(f, V_{CAP})|^2) . \frac{(\lambda(f))^2}{4.\pi} \right] . df \quad (21)$$

5.4 Antenna Design

The antenna performs the task of converting the incident electric field in the air to an AC electrical signal at UHF. Antennas come in many different shapes and sizes. During field measurements, several different antenna types were tested out in the field to study the effect of its orientation with respect to the wireless radiation. Best results were obtained with linear antennas such as dipoles and monopoles when they were held with their lengths parallel to the ground and normal to the direction towards the TV broadcast towers, which indicates the orientation of the electric fields oscillating in the air due to the TV signals. Orienting linear antennas parallel to the direction of the electric field increases the antenna's effective aperture area to the incident field, which maximizes the transduction of the incident electric field into a RF signal. The effective aperture area of the antenna is also increased by maximizing the antenna gain 'G(f)' as per the mathematical relationship in (21). The gain of an antenna is a measure of its overall effectiveness in traducing an incident electric field across it into a usable electrical RF signal from a particular direction. Typical gains for linear antennas currently available are listed in **Table 6**.

Table 6. Gain and Bandwidth performance of various antenna structures.

Antenna Type	Gain (dBi)	Gain	Bandwidth
Dipole	1.76	1.5	High
Monopole	3	2	High
Microstrip Patch	6-9	4-8	Low
Log Periodic	4-9	2.5-8	Medium
Arrays	6-15	4-31.6	Low
Horn	20	100	Low
Dish Antennas	61	100-400	Medium

5.4.1 Short Backfire Antenna (SBA)

The Short-Backfire Antenna (SBA) first developed in the 1960s has been extensively used in Maritime and Terrestrial radios. SBAs typically offer excellent radiation characteristics with a maximum gain in the order of 13-15 dBi with a relatively simple configuration. An SBA antenna comprises of a monopole feed that is half-wavelength long, which acts as the driving element. In addition, the SBA antenna makes use of a bottom disc with sides that are roughly two wavelengths in length, which acts as a reflector. SBA antennas suffer from low bandwidth primarily due to the dipole-based feed atop the reflector, with bandwidths typically lower than 1% [*90*]. An scaled-up SBA antenna similar to [*90*] with an optimized feed was designed to achieve maximum gain and bandwidth for the purpose of harvesting power present in wireless digital TV signals in the 500-700 MHz frequency bands. The SBA antenna comprises of a monopole-based driver on a paper substrate that is fed with a single-ended 50-ohm microstrip feed on the other side of the substrate. To achieve a wide-band performance for input impedance, the printed monopole is split along its central line into two parts with a slot [*90*]. The feeding element is suspended from a copper-clad reflector that is two wavelengths long as shown in the fabricated prototype in Figure 47 (i) (ii). The SBA antenna was designed using Ansoft's High Frequency Structure Simulator (HFSS). The SBA antenna dimensions and prototype are shown in Figure 47. The driving element of the SBA antenna was fabricated using copper tape on a paper-based substrate, and the reflector was fabricated using copper foil on a cardboard base as shown in Figure 47 (ii).

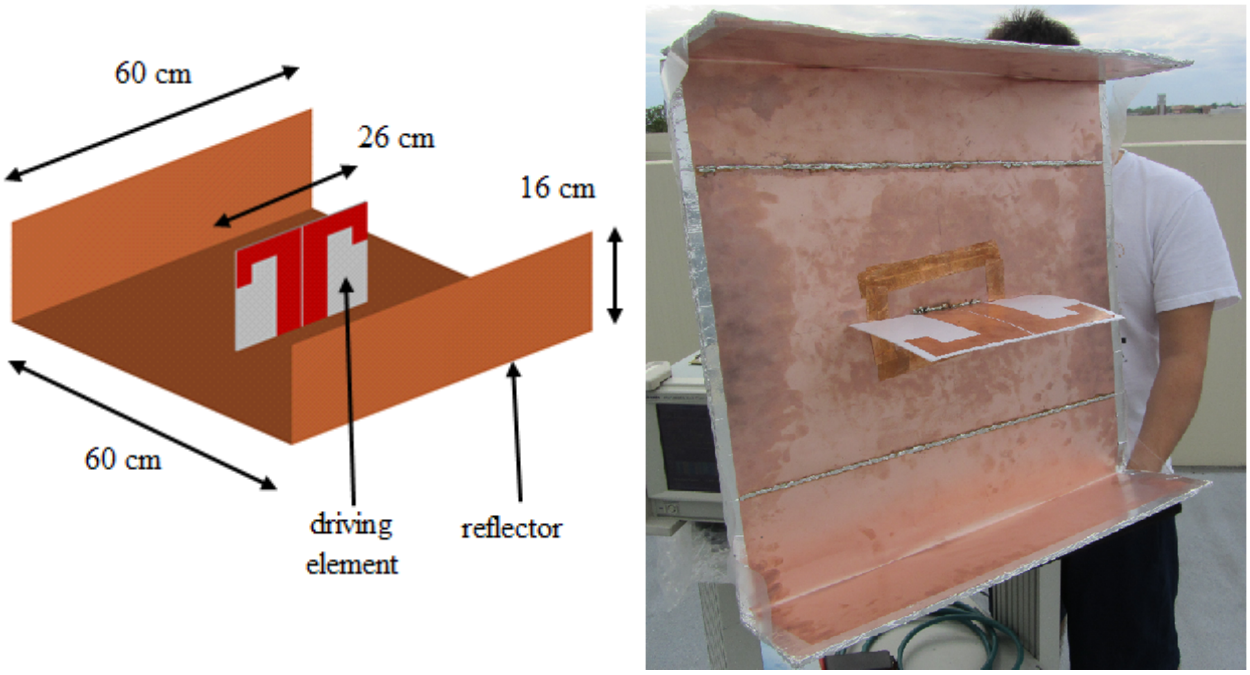

(i) (ii)

Figure 47. Short Backfire Antenna with optimized feed (i) Layout (ii) Prototype.

The fabricated SBA antenna prototype's return loss was measured using a Rohde and Schwarz ZVA-8 vector-network-analyzer (VNA). The measured and simulated return losses of the SBA antenna with respect to a standard 50 ohm port are plotted in **Figure 48**. The SBA antenna shows a return loss of 10dB or higher between 450 and 650 MHz, which translates into a much improved percentage bandwidth of 45 %. The measured bandwidth is lower than the simulated design primarily due to fabrication error as a result of cutting out and aligning the top and bottom layers of the driving element by approximation.

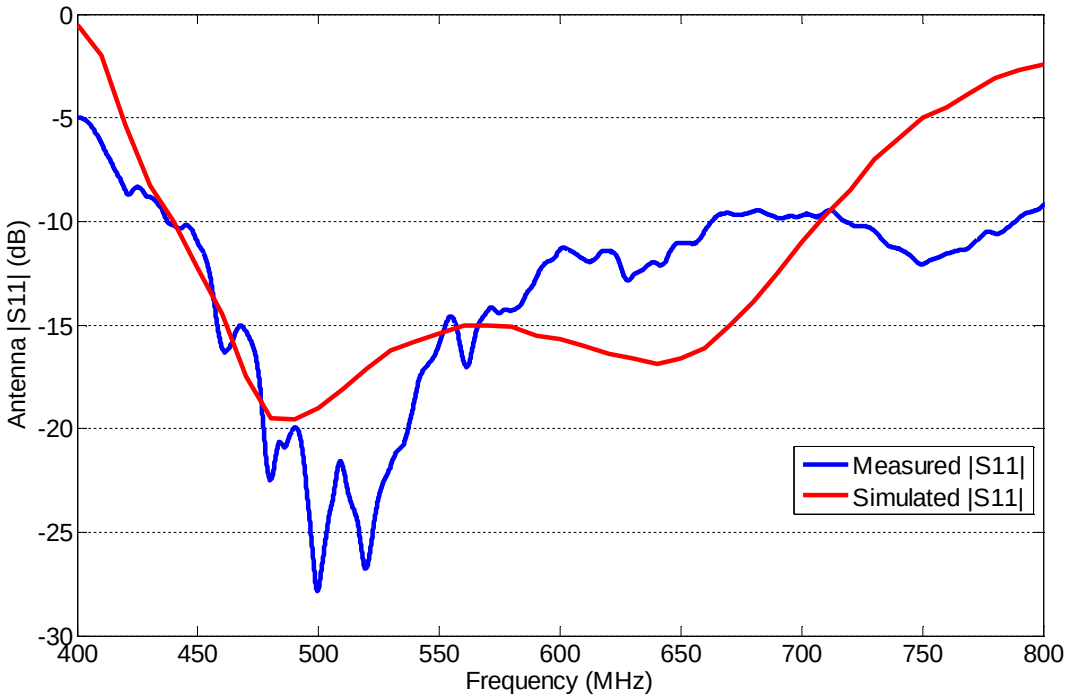

Figure 48. SBA Antenna Measured and Simulated return loss.

The radiation pattern of the SBA antenna was measured in a Satimo Stargate SG-24 anechoic chamber as shown in Figure 49. The antenna was placed on a base made out of Styrofoam that was drilled out to pass a calibrated 3.5 mm SMA Cable through to the antenna to provide an input RF signal swept between frequencies of 400 to 800 MHz. The power radiated out by the antenna was captured by calibrated probes placed around the Stargate system as shown in Figure 49. The base rotated around a vertical axis by fixed increments, which was controlled with servo motors, which allowed the probes to measure the radiation pattern of the antenna in the E-field and H-field planes.

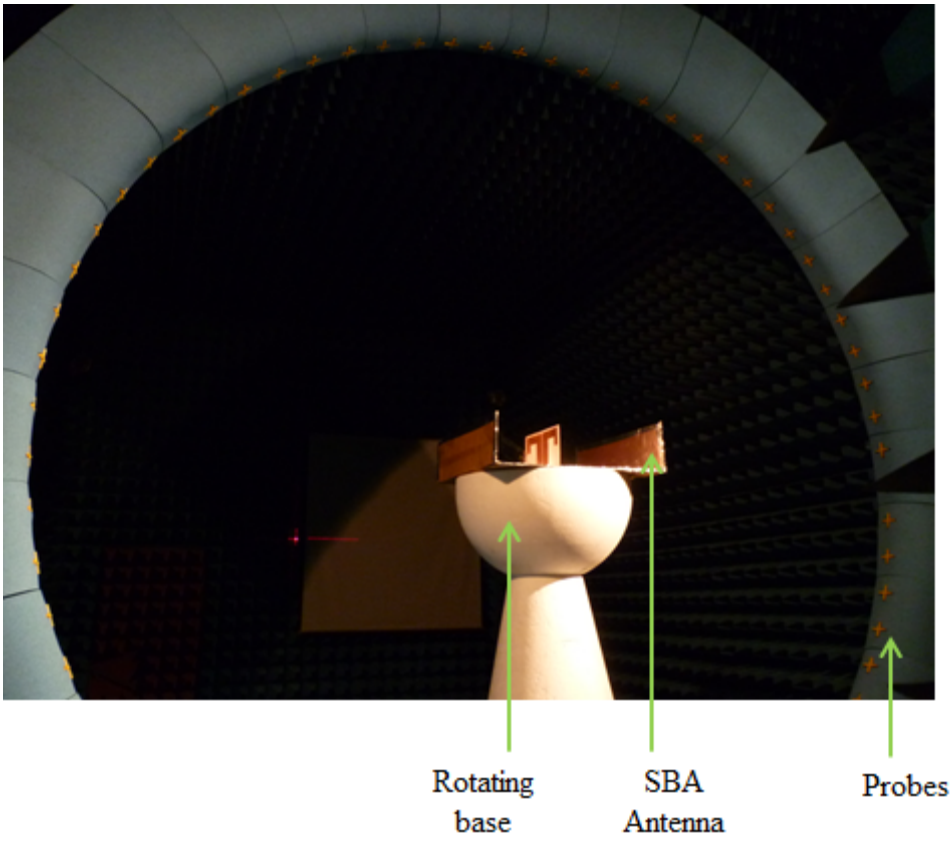

Figure 49. Radiation pattern measurements of SBA Antenna in Satimo-SG24 Chamber.

The measured and simulated radiation patterns of the SBA antenna in the E-field and H-field planes are shown in **Figure 50** and **Figure 51**, respectively, and show good agreement. The SBA prototype achieves a maximum measured gain of 9.5dBi with a front to back ratio of less than -25dB and an azimuth beamwidth of 50 degrees in the E-field plane.

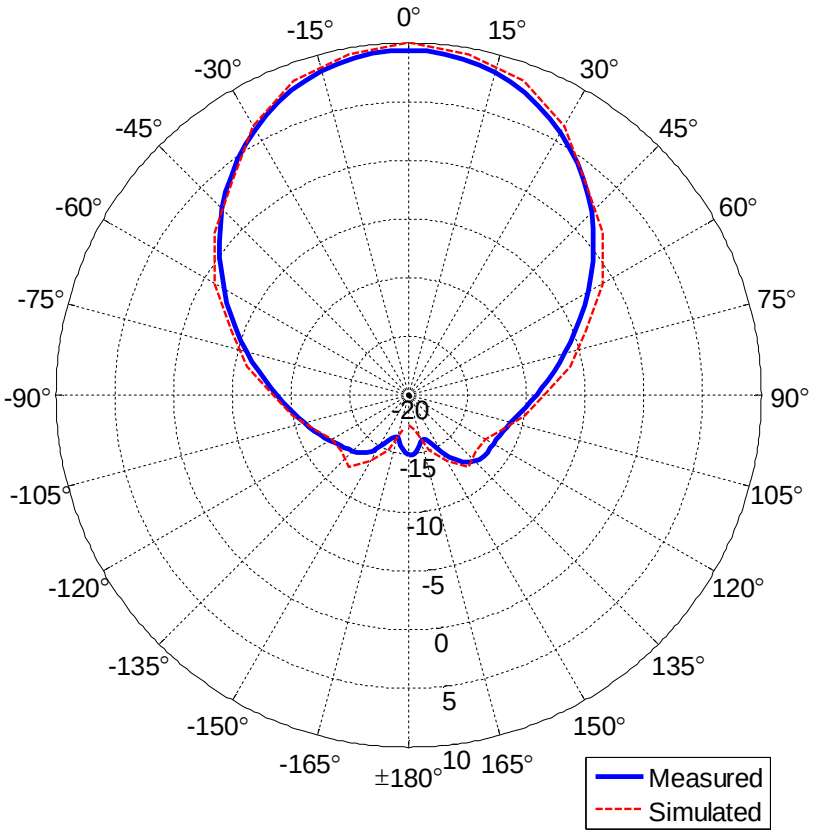

Figure 50. Measured and Simulated radiation pattern of SBA Antenna (Phi=90; E-plane).

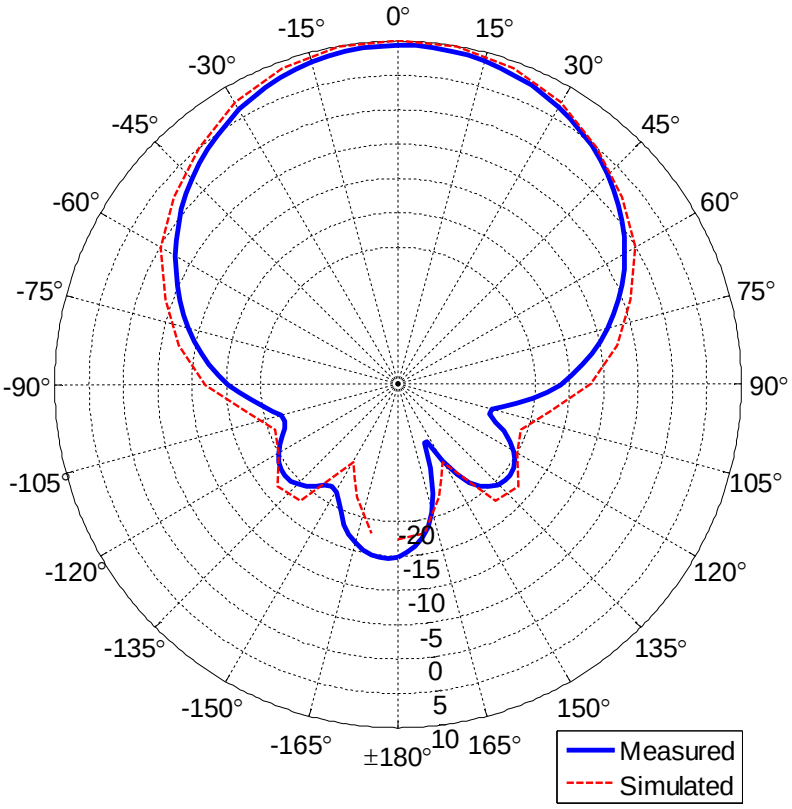

Figure 51. Measured and Simulated radiation pattern of SBA Antenna (Phi=0; H-plane).

The gain of the SBA antenna at different UHF frequencies is shown in Figure 52. The SBA antenna prototype exhibits a minimum gain of 8.5dBi and a maximum gain of 9.5 dBi between the digital TV bands of 500 and 700 MHz. The measured gain was observed to be between 0.5 and 1dB lower than the simulated design primarily due to fabrication defects, which lowered the antenna resonance between 600 and 700 MHz. The defects are primarily due to misalignment in positioning the driving element and substrate losses introduced by bonding the top and bottom layers of paper-substrate using commercially-available glue.

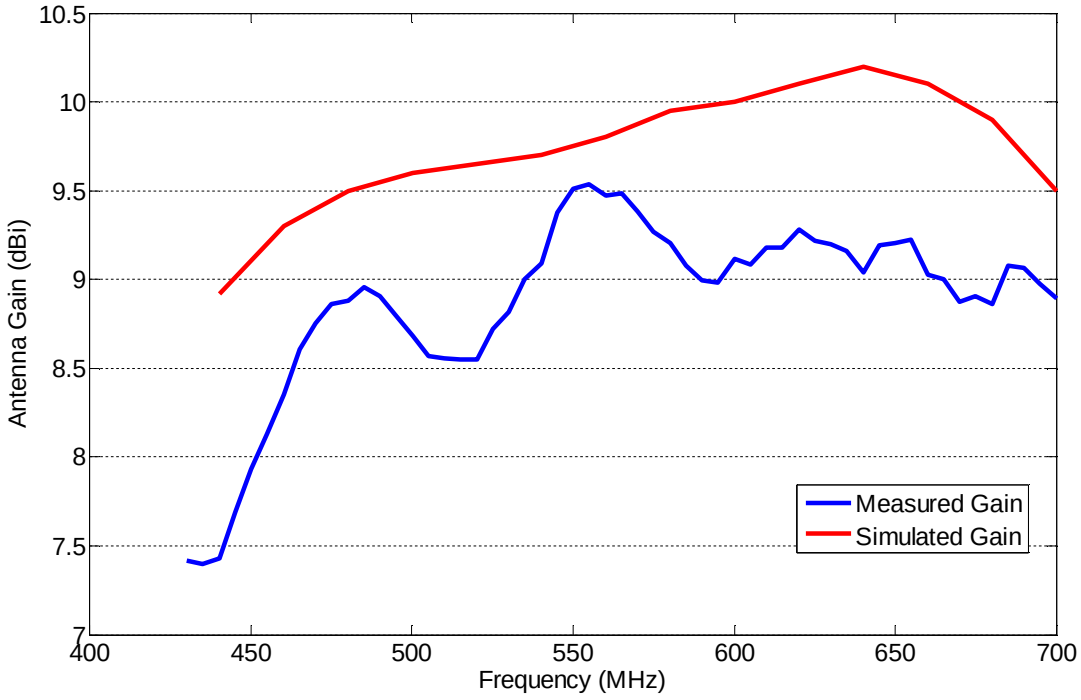

Figure 52. SBA Antenna Gain versus Frequency.

The response of the SBA antenna in the field was measured by aligning it in the direction of known TV broadcast towers in Midtown Atlanta. The wireless power captured by the SBA antenna was measured at its output using a Tektronics RSA 30408A real-time spectrum-analyzer (RTSA). The spectrum of the wireless power, and its spectrogram captured by the RTSA is shown in Figure 53. The spectrum shows the SBA antenna capture power from 17 different TV channels over the air with maximum carrier levels of around -30 dBm. However the aggregate of the power captured across all the carriers in the 17 digital TV channels adds up to -8.5 dBm. The spectrogram further shows the wireless power from all 17 digital TV channels to be continuously on as shown in Figure 53.

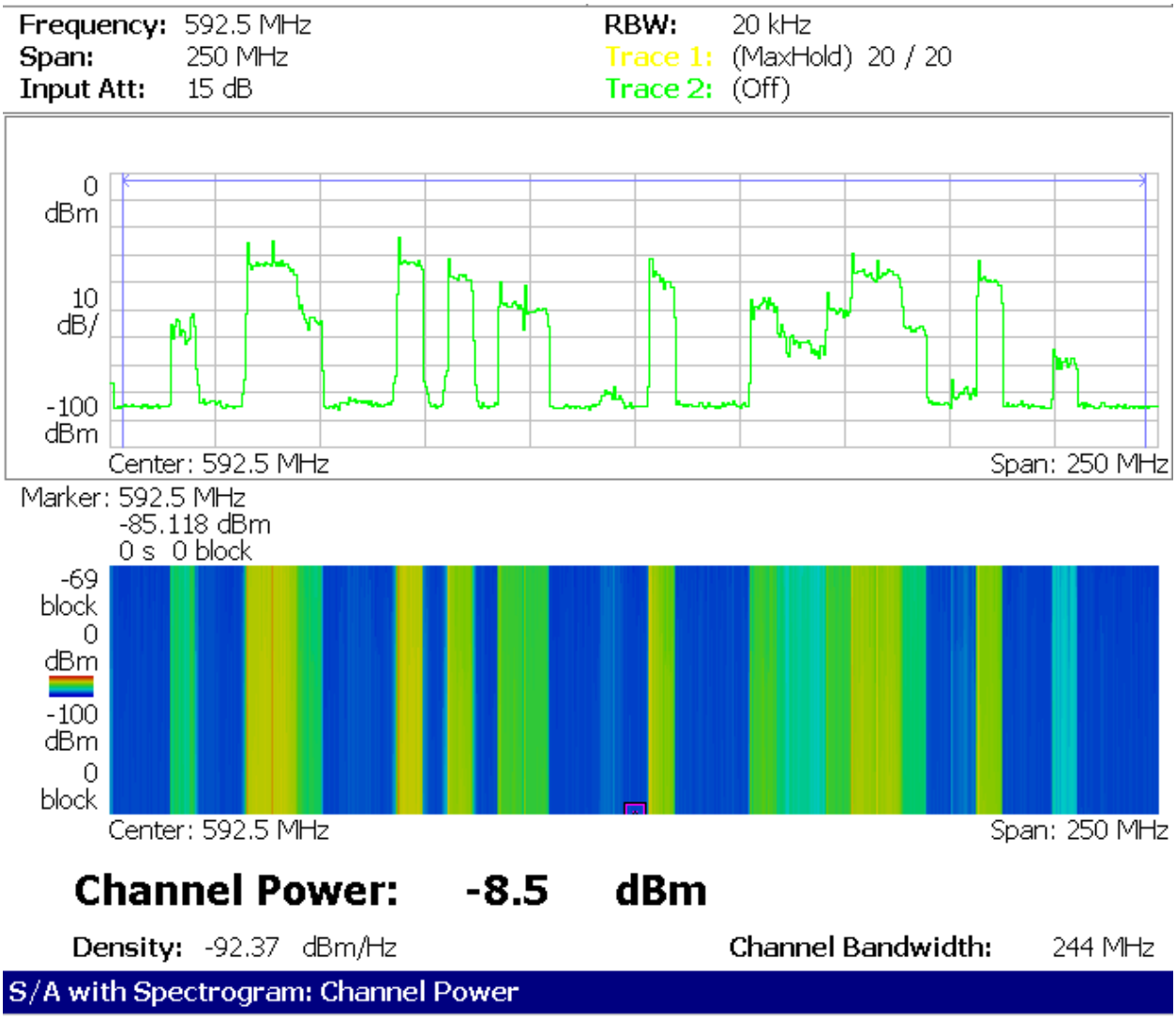

Figure 53. Wireless power spectrum captured by SBA antenna from 17 different TV channels broadcasted in Midtown Atlanta.

5.4.2 Log Periodic Antenna Array

While the SBA antenna array with an optimized input feed achieves high gain and bandwidth, its bulky 3D size does not allow for easy mounting and portability that are required in many wireless sensor network applications. The 60 cm long reflector is required to be a multiple of the wavelength, which at UHF frequency results in a substantially large structure as shown in Figure 47 (ii).

The size of antenna arrays with gains higher than 4dBi can be shrunk by using frequency-independent structures such as log-periodic antennas. Log-periodic antennas can achieve gains similar to array-type antenna but with much wider bandwidths [*78*]. First designed by DuHumel and Isbell from University of Illinois [*91*], a well-designed log-periodic antenna can be expected to capture well over 4 and up to 8 times as much power from an optimum direction. In addition, a properly designed log-periodic antenna should have as high of a gain ('G') and a 50 ohm input impedance across as wide of a bandwidth possible between 500-700 MHz frequencies to absorb power in as much of the incident electric fields from as many TV channels broadcasted out from TV towers in the vicinity. The trade off with using an antenna with high gain is that it is only effective within a certain beam width or angle of coverage and diminishes rapidly beyond it due to which the antenna has to be oriented with its end fire direction towards the wireless power source. However within its angle of coverage in the azimuth plane, a high gain antenna is capable of transducing greater amounts of wireless power from the electric field incident on it at even further distances from the TV broadcast towers. This results in the generation of a higher magnitude RF voltage across its terminals. It is important to bump up the antenna gain high enough so as to induce a voltage across its terminals that is greater than the turn-on (threshold) voltage of the diodes that are used in the RF to DC converter circuit. Doing so ensures that the

diodes used in the RF to DC converter circuit are forward biased and turned on enabling its charge up operation to give a high voltage at its output tank capacitor.

A much more compact Log-periodic antenna was designed and optimized for capturing power from ambient digital TV signals in the air using [*78*] [*91*] [*92*]. In [*92*], Carrel presents an empirically derived method of miniaturizing log periodic antennas, albeit for a three dimensional antenna structure. For this work, a planar log periodic antenna structure was designed using a similar concept for the purpose of capturing ambient wireless power from the air. The antenna was designed with specifications listed in **Table 7**.

Table 7. E-WEHP Log-periodic antenna specifications.

<table>
<tr><td></td><td colspan="2">Parameter</td><td>Simulated</td><td>Measured</td></tr>
<tr><td rowspan="3">Required Specifications</td><td colspan="2">Gain ‘G’ (dBi)</td><td>5-7.4</td><td>5-7.3</td></tr>
<tr><td colspan="2">Bandwidth ‘Bar’ (MHz)</td><td>500-600</td><td>500-600</td></tr>
<tr><td colspan="2">Size (cm2)</td><td>30 x 21.5</td><td>30 x 21.5</td></tr>
<tr><td rowspan="10">Dimensions</td><td colspan="2">Scale Factor ‘τ’</td><td colspan="2">0.95</td></tr>
<tr><td colspan="2">Relative Space ‘σ’</td><td colspan="2">0.18</td></tr>
<tr><td colspan="2">Angle ‘α’</td><td colspan="2">6.59</td></tr>
<tr><td colspan="2">Number of elements ‘I’</td><td colspan="2">6</td></tr>
<tr><td>L1 (cm)</td><td>30</td><td></td><td></td></tr>
<tr><td>L2 (cm)</td><td>28.5</td><td>R2-R1 (cm)</td><td>4.95</td></tr>
<tr><td>L3 (cm)</td><td>27.1</td><td>R3-R2 (cm)</td><td>5.35</td></tr>
<tr><td>L4 (cm)</td><td>25.75</td><td>R4-R3 (cm)</td><td>0.65</td></tr>
<tr><td>L5 (cm)</td><td>25.50</td><td>R5-R4 (cm)</td><td>6.15</td></tr>
<tr><td>L6 (cm)</td><td>24.23</td><td>R6-R5 (cm)</td><td>6.55</td></tr>
</table>

In order to achieve maximum directivity and gain in excess of 9 dBi with a minimal size, the optimum antenna element scaling factor (τ) and relative element spacing (σ) were determined to be close to 0.94 and 0.18, respectively using empirical relationship derived in [*91*] [*92*]. The

bandwidth of the antenna (B_{ar}) was restricted to between 500 and 600 MHz since the bulk of the TV channels were found in those bands as shown by field wireless radiation measurements in **Figure 43** (i) and (ii). Lowering the bandwidth to 100 MHz also enables us to achieve the desired gain (G) of between 7 and 9 dBi using just 6 radiating elements ('I') as determined by (22). In order to tune the antenna to operate across the desired TV frequency channels, the longest dipole is designed to have an approximate length (L_6) as in (23), which determined to be 30 cm. The length of the remaining radiating dipole elements (L_1-L_5) of the array were determined using the scaling factor as in (24) and (25), and are listed in **Table 7**.

$$I = 1 + \frac{\ln(B_{ar})}{\ln(1/\tau)} \tag{22}$$

$$L_6 = \frac{1}{2}\frac{v_C}{f_{MIN}} \tag{23}$$

$$\frac{1}{\tau} = \frac{L_6}{L_5} = \frac{L_{i+1}}{L_i} \tag{24}$$

$$R_{i+1} - R_i = \sigma \times 2 \times L_{i+1} \tag{25}$$

Equations to determine the cross sectional dimensions of the dipole elements and feed in [*93*] [*92*] are for 3-dimensional forms due to which CST Microwave studio had to be relied on to simulate and optimize the planar log periodic antenna structure further to achieve an input impedance of 50 ohms while maintaining high gain. The antenna was miniaturized to fit into an area equal to that of an A-4 size paper for unobtrusive mounting on walls and side rails along building structures as shown in **Figure 54**. To shrink the antenna width, the dipole elements are

designed to have a tooth like pattern so as to be able to fit within A4 width while still having the same effective radiating length listed in **Table 7**.

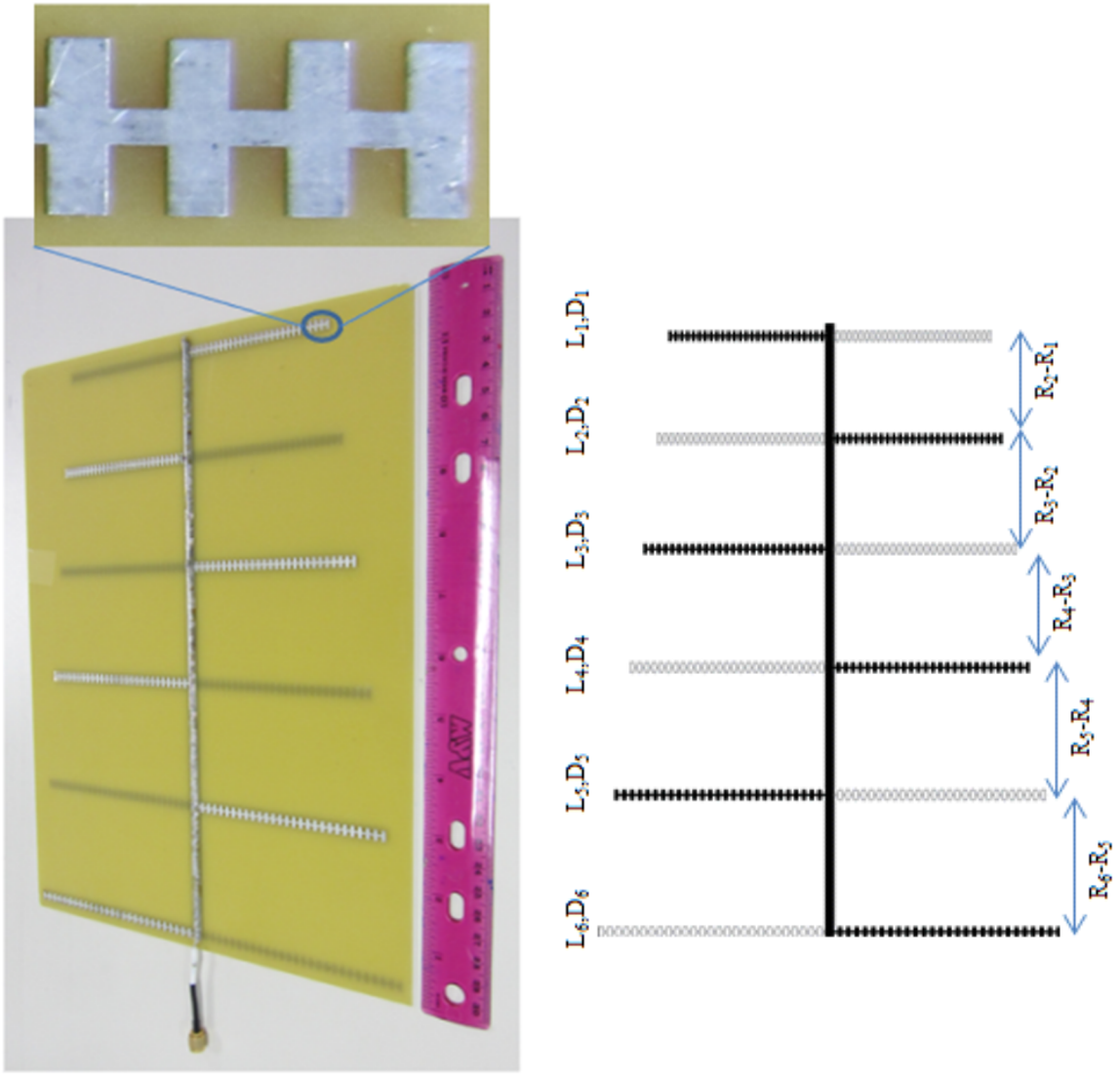

(i) (ii)

Figure 54. (i) E-WEHP Log-periodic antenna prototype fabricated on 0.062 inch FR-4 substrate using tooth-like pattern. (ii) E-WEHP Log-periodic antenna layout.

The optimized log-periodic antenna structure was fabricated on standard 0.062 inch FR-4 substrate as shown in **Figure 54**. The log-periodic antenna is connected to the E-WEHP RF-DC converter using a standard 3.5mm SMA cable with its inner conductor and outer shields stripped to feed the dipole elements on the antenna's under and upper sides, respectively, in the form of an infinite balun.

The antenna return-loss was measured using a Rohde and Schwarz ZVA-8 vector network analyzer, and showed an input impedance of close to 50 ohms between the frequencies of 500 and 600 MHz, with peak return loss resonance occurring between 540 and 560 MHz where peak ambient electric fields are present as shown in **Figure 55**.

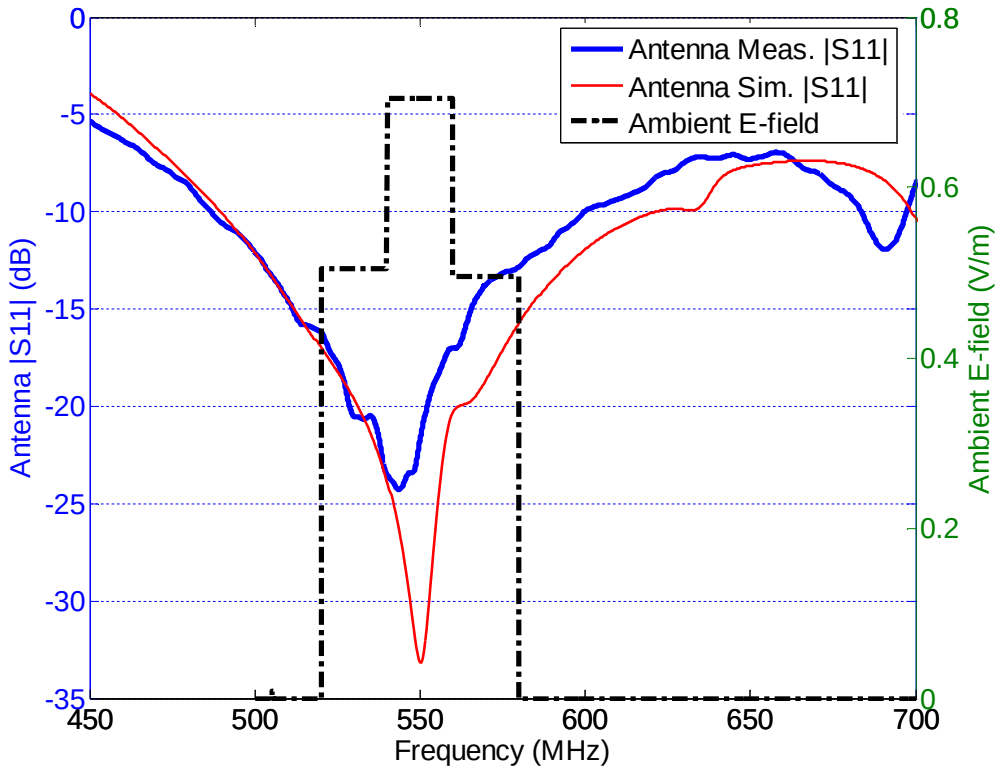

Figure 55. E-WEHP Log-periodic Antenna measured and simulated return loss.

The radiation pattern of the Log-periodic was also measured in a Satimo Stargate SG-24 anechoic chamber as shown in **Figure 56**. The measured and simulated radiation pattern of the Log-periodic in the E and H-field planes are plotted in **Figure 57** and **Figure 58**, respectively, and show good agreement. The Log-periodic design has an end-fire radiation pattern with a half-power beamwidth of 62.7 degrees as simulated by CST. The measured gain is in good agreement with the simulations carried out using CST microwave studio that are also plotted as a function of frequency in **Figure 59**.

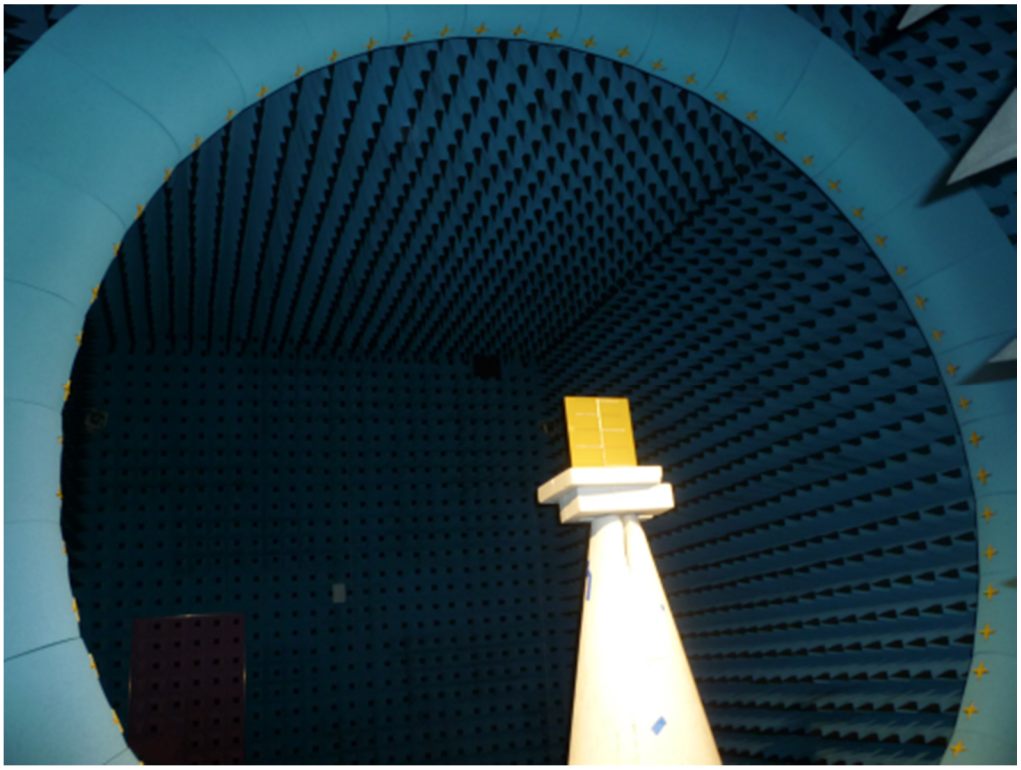

Figure 56. Radiation pattern measurements of E-WEHP Log-periodic Antenna in Satimo-SG24 Chamber.

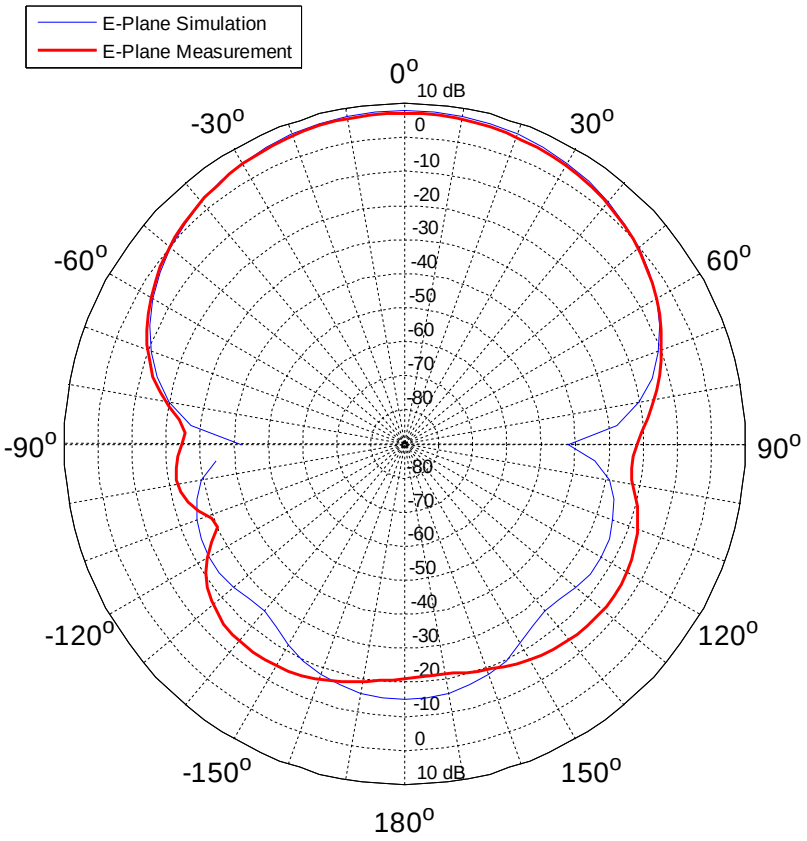

Figure 57. Simulated and Measured radiation pattern of E-WEHP Log-periodic antenna (E-plane, Phi=0).

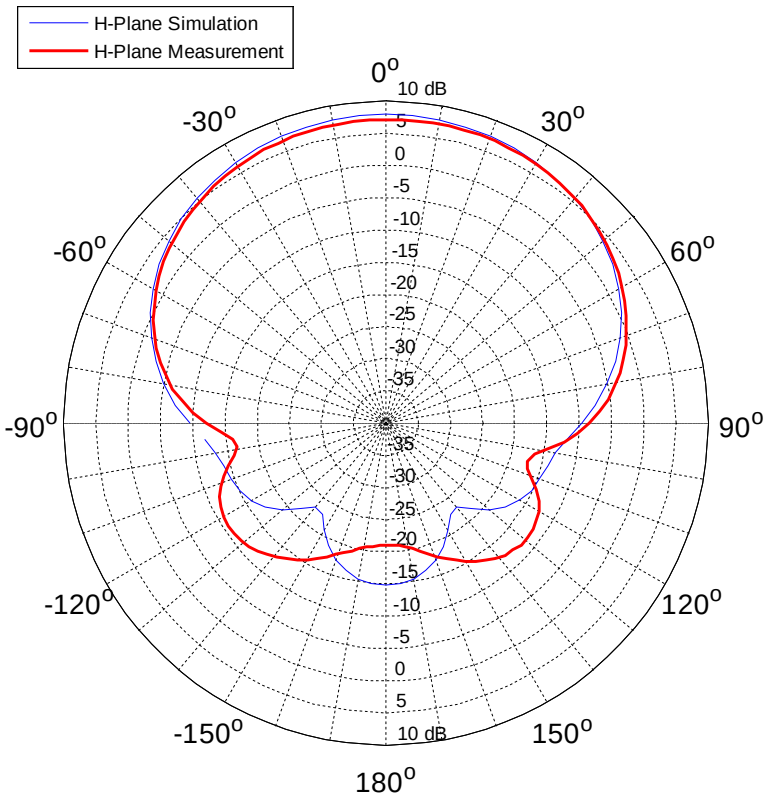

Figure 58. Simulated and Measured radiation pattern of E-WEHP Log-periodic antenna (H-plane, Phi=90).

The antenna achieves a measured gain of between 5 and 7.3 dBi, and simulated gain of between 6 and 9 dBi in the 500-600 MHz bands with its maxima at 550 MHz lining up well with the peak of the wireless radiation captured during field measurement as shown in **Figure 59**. Therefore, it maximizes its absorption of wireless power from ambient electric fields present in air due to digital TV channels.

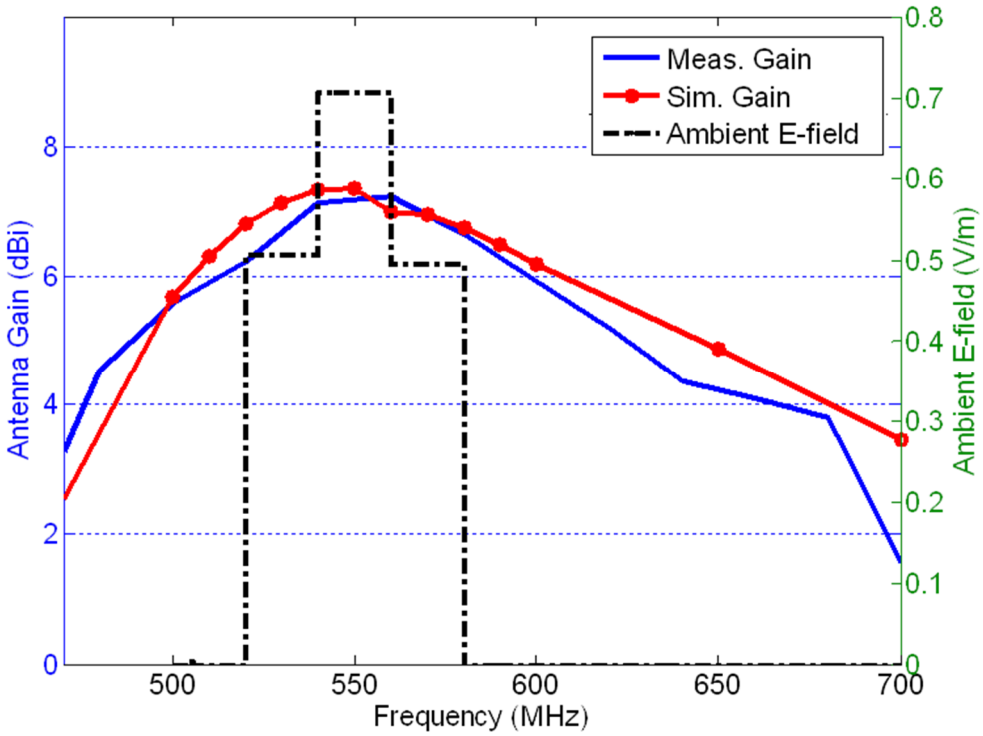

Figure 59. E-WEHP Log-periodic antenna measured and simulated gain versus frequency.

The power transduced by the E-WEHP log-periodic antenna design from the ambient electric fields due to digital TV signals was measured by connecting it to a Tektronics RSA3308B spectrum analyzer, and pointing it towards a known TV broadcast source atop the Tokyo TV tower 6.5km away in downtown Tokyo as shown in **Figure 60**.

Figure 60. Location of TV broadcast tower in downtown Tokyo with respect to measurement point (POI).

Wireless Power levels captured were observed to be about 3dB higher when the antenna dipole elements were oriented parallel to the TV signal's E-field in the horizontal plane parallel to the ground. The power transduced by the antenna from the digital TV signals in the air from the optimum direction is shown in **Figure 61**. The E-WEHP antenna captures power from nine TV channels broadcasted out in downtown Tokyo whose channel numbers are also listed in **Figure 61**.

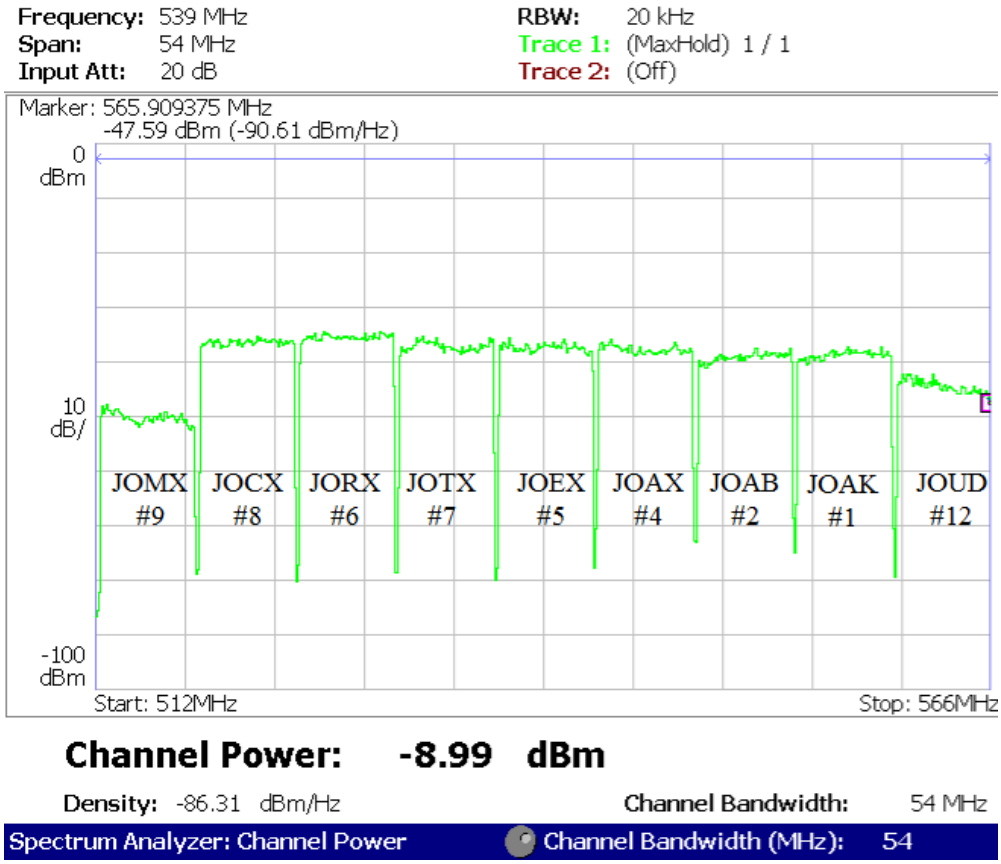

Figure 61. Wireless power spectrum captured by E-WEHP Log-periodic antenna from nine digital TV channel broadcasts in downtown Tokyo.

While the peak power derived by the antenna from each of the carriers in each channel is only about -35 dBm (0.32 µ-watts), the total channel power captured from the combined 9 channels aggregate up to -8.99 dBm (126.2 µ-watts), which is what the E-WEHP is designed to exploit. The channel power obtained by the antenna from each channel varies from between -15.57 dBm (27.7 µwatts) for TV channel #6 (JORX TV: 524-530 MHz) as shown in **Figure 62**, and approximately -27dBm (1.8 µ-watts) for TV Channel #9 (JOMX: 512-518 MHz).

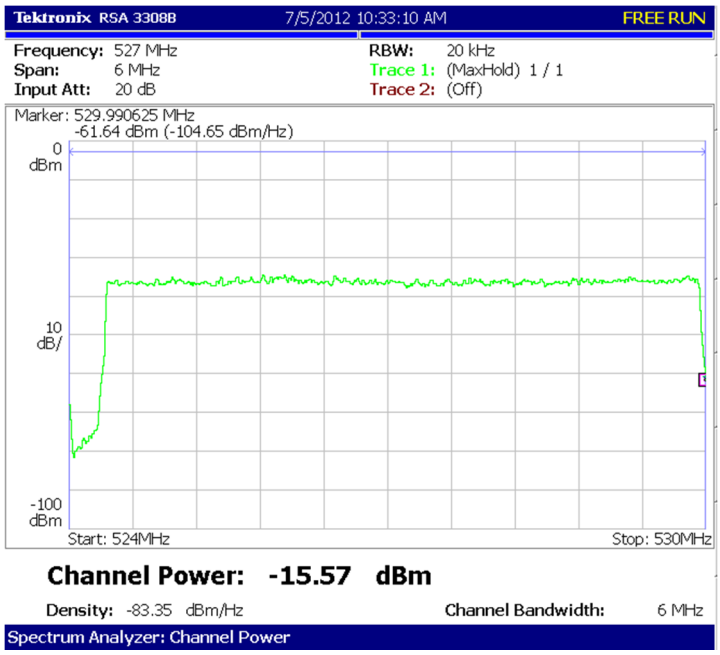

Figure 62. Measured channel power for TV channel #6 (JORX) by log-periodic antenna at measurement point.

The E-WEHP log-periodic antenna was also field-tested in Midtown Atlanta by orienting the antenna's end-fire direction towards known TV broadcast towers in Midtown Atlanta as shown in **Figure 63**. Over the air TV broadcasting in most North American cities is observably different than the broadcast infrastructure in downtown Tokyo primarily due to different population densities and ownership models between 2 places. Unlike in Tokyo, TV broadcast towers in Atlanta are observed to be scattered all over the Midtown and Downtown areas. Broadcast towers in the U.S. tend to be privately owned separately from the TV broadcasters, and it is common for space atop the towers to be leased to different TV and cellular service providers contributing to the scattered nature of the TV broadcasts as seen in **Figure 63**.

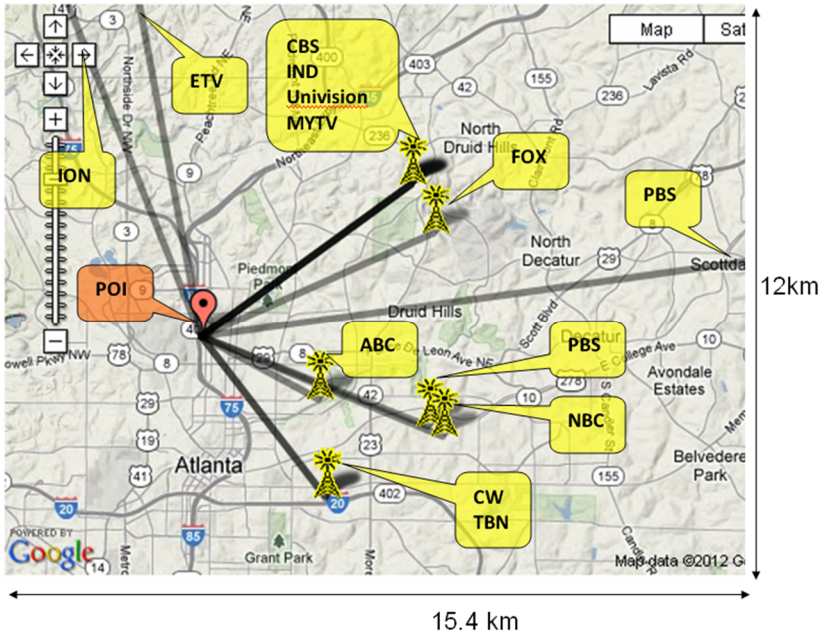

Figure 63. Location of TV broadcast towers in Midtown Atlanta with respect to measurement point (POI).

The 62.17 degree beamwidth of the Log-periodic in the E-field plane is helpful for the purpose of harvesting power from TV signals in such a scattered broadcast environment. Aligning the Log-periodic antenna in just 2 directions in the north-east and south-east directions as shown in **Figure 64** allows power to be harvested from more than 1 TV channel.

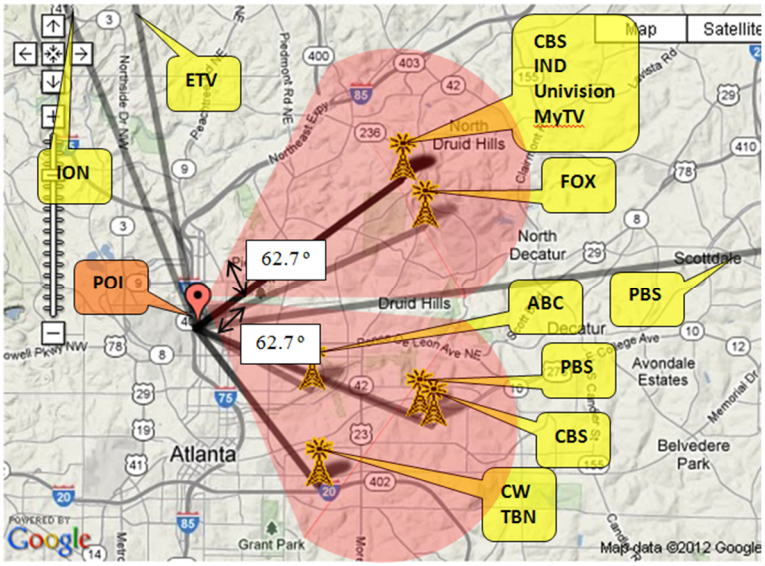

Figure 64. Angular coverage of the designed log-periodic antenna. Horizontal Beamwidth = 62.17 degrees.

The wireless power spectrum captured by the Log-periodic in Midtown Atlanta is shown in **Figure 65**, and exhibits a scattered placement of the TV channels frequency-wise between 500 and 700 MHz bands. While the carrier power levels have a peak value of -25dBm or 3.16 microwatts, the aggregate of the power across all the carriers in all the digital TV channels adds up to -10.87dBm or 81.80 microwatts. The aggregate channel power present in each of the TV channels measured with the RTSA is shown in **Table 8**. Seven-eighths of the total TV wireless channel power measured in Midtown Atlanta was observed to be from just five TV Channels namely CBS, IND, MyTV and Fox as shown in **Figure 66**. The aggregate power present from multiple carriers was measured to be -13.92 dBm or 40.55 microwatts due to CBS and IND TV channels and -15.29 dBm or 29.58 microwatts due to MyTV and Fox TV Channels as shown in **Figure 66**.

Table 8. Ambient RF Power Captured by the Log-periodic Antenna Design at each of the ATSC Digital TV channels at measurement point in Atlanta (POI).

TV Channels	***Freq. Band (MHz)***	***Measured Channel Power***	
		dBm	***microwatts***
CBS	500-506	-16.92	20.32
IND	506-512	-16.92	20.32
MyTV	536-542	-16.29	23.5
Fox	548-554	-22.05	6.24
WDTA	596-608	-24.83	3.2
ABC	620-626	< -24.83	< 3.2
ETV	632-638	< -24.83	< 3.2
CW	644-650	< -24.83	< 3.2
TBN	650-656	< -24.83	< 3.2
Univision	674-680	< -24.83	< 3.2

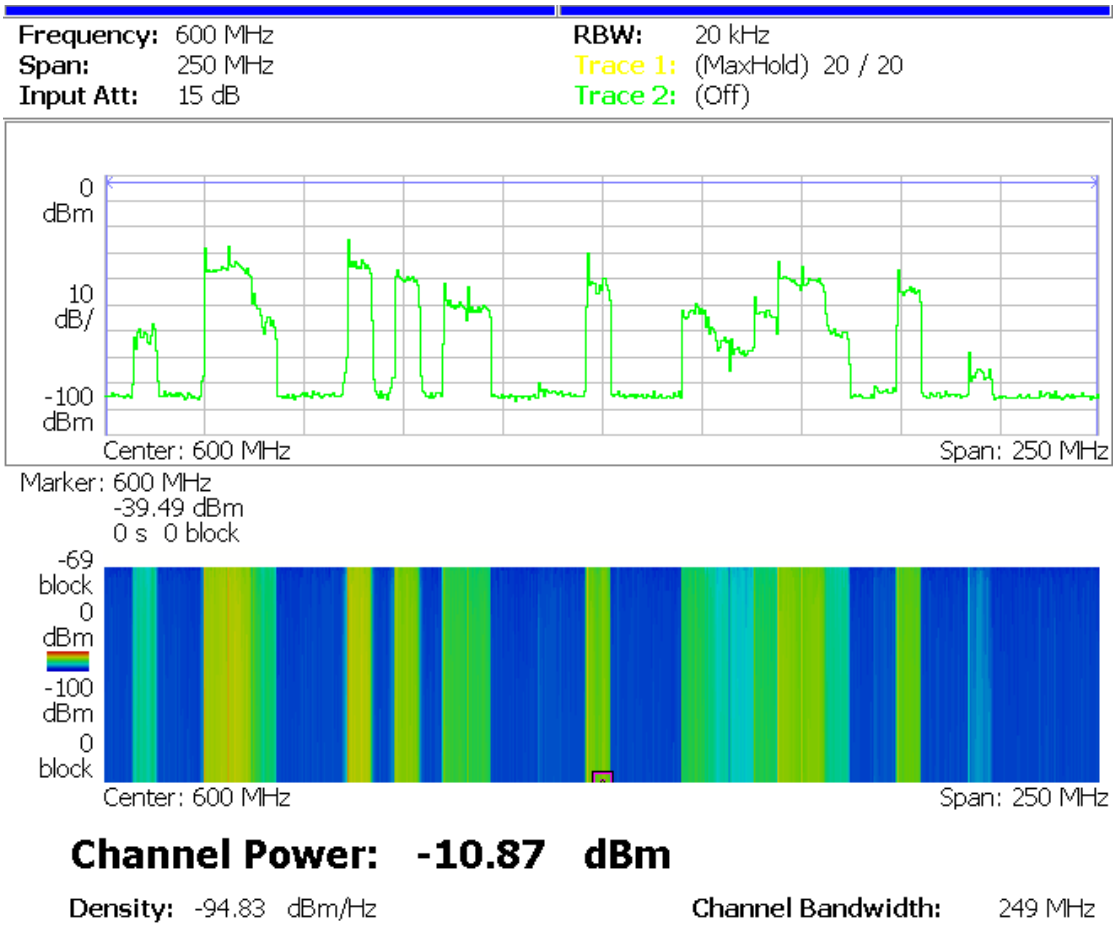

Figure 65. Wireless power spectrum captured by E-WEHP Log-periodic antenna from digital TV channel broadcasts in Midtown Atlanta.

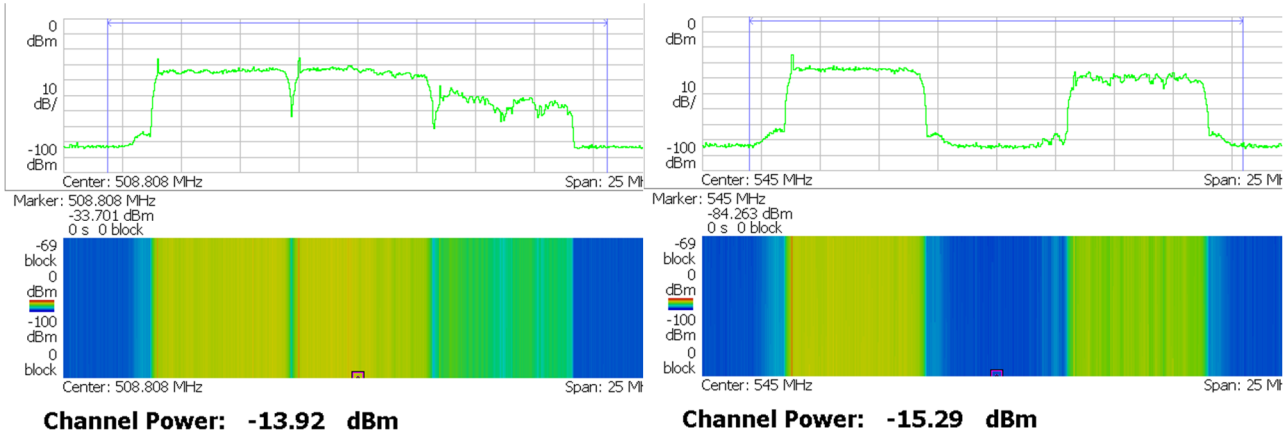

Figure 66. Measured channel power for CBS (500-506 MHz), IND (506-512 MHz), MyTV (536-542 MHz) and Fox (548-554 MHz) TV channels captured by Log-periodic antenna at the Georgia Tech campus in Midtown Atlanta.

5.5 RF to DC Charge-Pump Circuit

Each of the carriers in the digital TV channels that are transduced across the antenna terminals are in RF form, and induce a very low voltage RF signal. Being able to harness this power requires as many of the carrier signals in as many digital TV channels incident to be rectified, and stepped up to an output voltage of 1.8V or higher at which most electronic devices such as embedded processors and sensors can operate. One option to step up and rectify low power RF signals are RF-DC charge pump circuits (also known as RF voltage or Dickson multipliers) that are commonly used in EPC-Gen 2 RFID tags in the free 900 MHz ISM band. In spite of having low efficiencies and a lack of dynamic output voltage control at higher power levels compared to DC to DC converters, they provide battery-less operating capability at very low power levels. Advances in semi-conductor and IC design technologies have allowed RFID Gen-2 tags using charge pumps to give out output voltages of close to 1V, which is enough to power on the tag's digital circuitry for limited duty cycles with just tens of microwatts of wireless power [*94*]. The E-WEHP platform is fitted with a custom-designed, ultra-low-power RF-DC Charge Pump circuit that is optimized to harvest and store ambient RF energy present in the digital TV channels in the air. In [*95*], Vita theoretically proves that for single tone input power levels in the 20 to 80 microwatts range, RF-DC charge pumps containing between three and eight stages yield the maximum output voltage for the least amount of input power. Several different RF charge pump circuits using different commercially-available Schottky diodes are tested for RF-DC conversion performance. In some configurations, two step-up stages are replaced with a step up RF transformer coil in an attempt to boost the RF-DC conversion efficiency. Transformers do not suffer from forward-voltage drops suffered by diodes, which yield higher efficiencies. The designs are optimized using the Agilent Advanced Design Systems

(ADS) RF system simulator with the harmonic balance method for operation in the 500-600 MHz frequency bands using diode models provided by the diode manufacturers.

The four different RF-DC topologies are shown in **Figure 66**. Four different prototypes named E-WEHP v1, v2, v3 and v4 were fabricated on standard 0.062 inch FR-4 to test out each of the topologies shown in **Figure 67** (i), (ii) and (iii). The fabricated prototypes are shown in **Figure 68**, **Figure 69**, **Figure 70** and **Figure 71** . All E-WEHPs comprise of an RF input that is connected to an antenna and a matching circuit with the help of standard 3.5mm SMA connectors. The RF input is fed into an RF-DC rectifying circuit that converts and steps up the low RF input signal induced across the antenna into a usable DC form, which is stored as energy across a 100 µF charge tank capacitor. E-WEHP v1 in **Figure 68** (i) uses a 1:2 RF Transformer fabricated by Skyworks with a 3-stage RF-DC Charge pump topology as shown in **Figure 67** (i) with the intention of minimizing forward losses introduced by diodes during the RF-DC rectification process. Avago HSMS-282C diodes with low forward losses and parasitics are used in the RF-DC Charge pump circuits. E-WEHP v2 in **Figure 69** uses an 8-stage RF-DC Charge pump topology as shown in **Figure 67** (iii). E-WEHPs v3 and v4 in **Figure 70** and **Figure 71** use a 5-stage RF-DC Charge pump topology as shown in **Figure 67** (ii). E-WEHP v4 uses a modified layout with a shorter coplanar waveguide (CPWG) as an RF input feed, whereas v3 uses a microstrip line as an RF input feed.

In, **Figure 67** during each consecutive negative half-cycle of the input RF AC signal, the odd-numbered capacitors C1,C3,C5,C7 and C9 get charged to a voltage equal to the input RF voltage plus the voltage across the preceding even numbered capacitor through odd-numbered diodes D1, 3, 5 and 7 minus the forward voltage loss across each diode. During the positive half cycle of the RF input signal, the even numbered capacitors get charged in a similar fashion

through forward biased even-numbered diodes D2, 4, 6, 8 and 10 with opposite polarities shown in **Figure 67**. The voltage across the output charge tank capacitor as a function of a single tone of the input RF voltage induced across the antenna is estimated by (26), where 'x' is the number of charge pump stages, and 'V_f' is the voltage induced at the input due to each carrier present in the digital-TV signal. The output voltage of the RF-DC charge pump is adversely affected by the forward voltage-drop across the diode junction (V_d), which represents resistive losses through the diode due to which low-barrier Avago HSMS-282C Schottky diodes with the lowest available forward voltage and junction capacitance at microampere current levels were used. Circuit traces were kept as small as possible to minimize substrate losses.

$$V_{CAP} = 2 \cdot x \cdot V_f - (2 \cdot x + 1) \cdot V_d \tag{26}$$

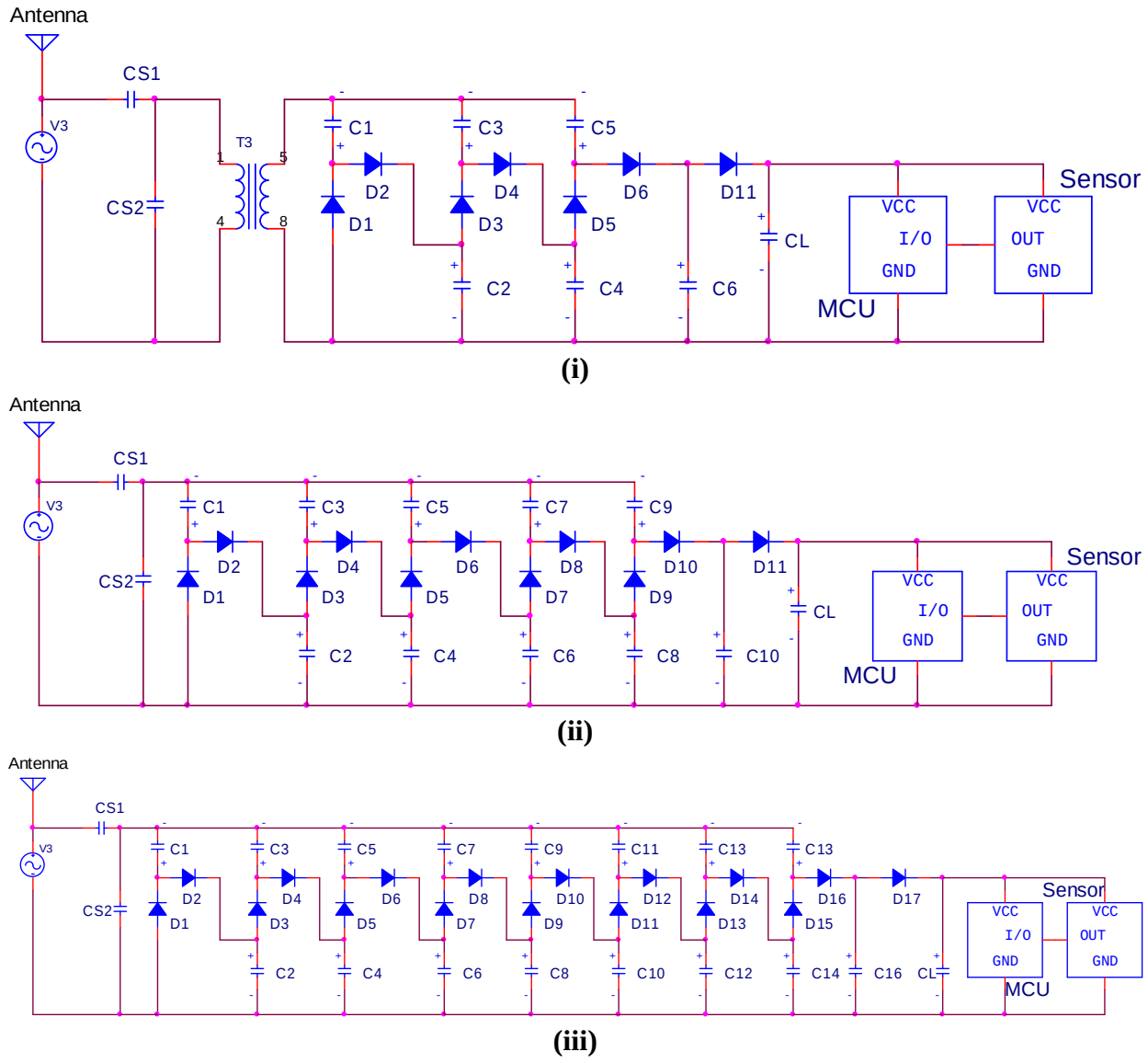

Figure 67. RF-DC-converter-circuit topologies used to rectify and step-up ambient wireless power.
(i) 3-Stage charge pump with 2:1 RF transformer. (ii) 5-Stage charge pump. (iii) 8-Stage charge pump.
C1-C13 (odd) = 15 pF, C2-C16 (even) = 20 pF, CL = 100 µF, CS1=1pF, CS2=6.6pF.

Microwatts of power present in the wireless TV signals, which are stored in DC form across the charge tanks, are utilized using a collect first (Charge/sleep) mode during which enough wireless power is allowed to build up across the 100µF charge tank, and use later

(Active/Discharge) during which the stored energy is utilized towards a useful end application. DC energy utilization from the charge tank is managed using a power management unit (PMU). The Power management unit is implemented using an analog circuit in E-WEHP v3 shown in **Figure 68** (iii), which uses a MOSFET switch to route power that is stored in the charge tank once its voltage reached a threshold that is adjustable using a potentiometer along with a zener diode. Perpetually high leakage currents through the zener diodes during the Charge and Discharge cycle combined with the lack of flexibility of altering the zener breakdown voltage necessitated the use of a smarter embedded option for the PMU in E-WEHPs v2 and v4 shown in **Figure 69** and **Figure 70**. E-WEHPs v2 and v4 use a self-adjusting embedded firmware implemented in a Microchip PIC24F microcontroller to carry out the PMU function. The RF-DC response of E-WEHPS v1, v2, v3 and v4 are characterized in the 500-700 MHz bands in the subsequent section.

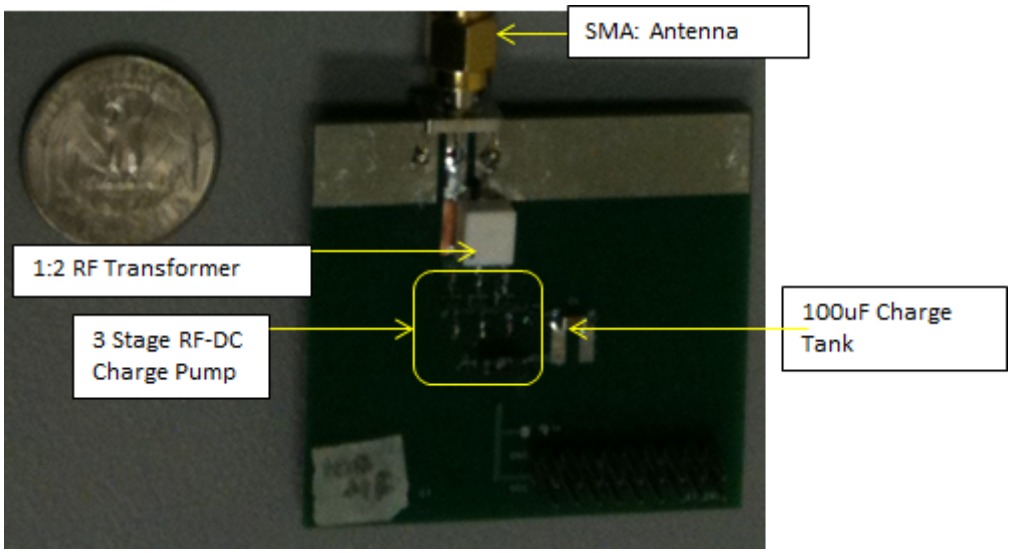

Figure 68. E-WEHP v1 prototype with 1:2 RF transformer and 3 stage RF-DC charge pump circuit.

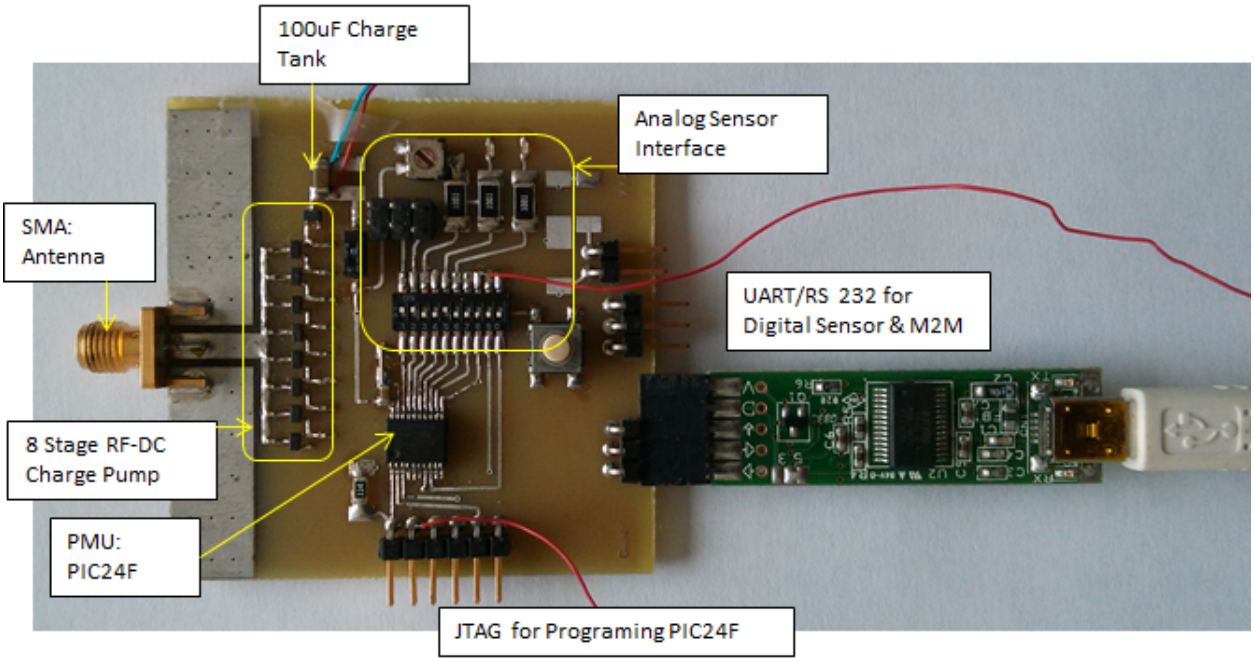

Figure 69. E-WEHP v2 prototype with 8 stage RF-DC Charge pump circuit and PIC24F microcontroller based PMU.

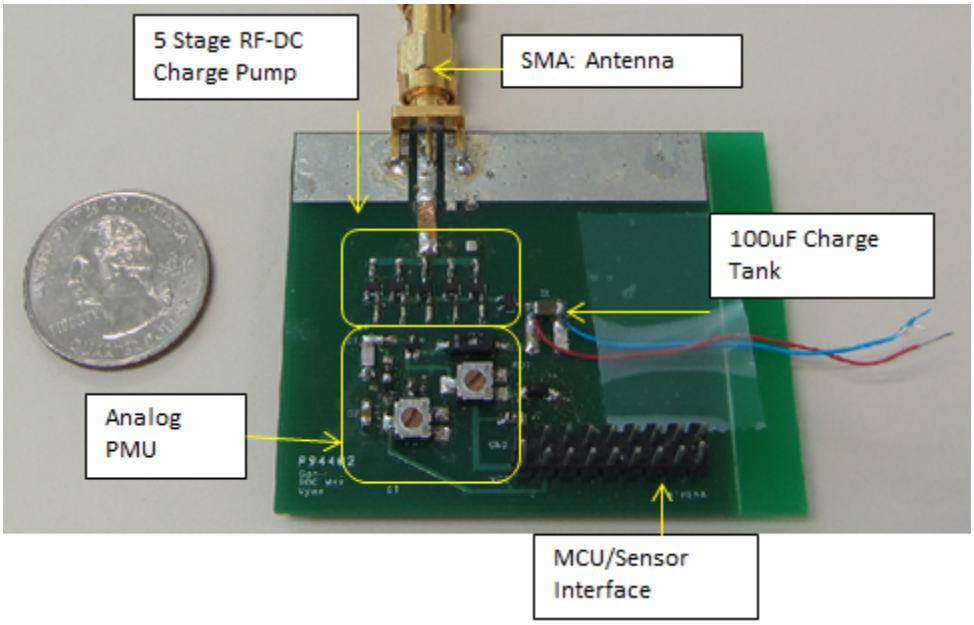

Figure 70. E-WEHP v3 prototype with 5 stage RF-DC Charge pump circuit and analog PMU.

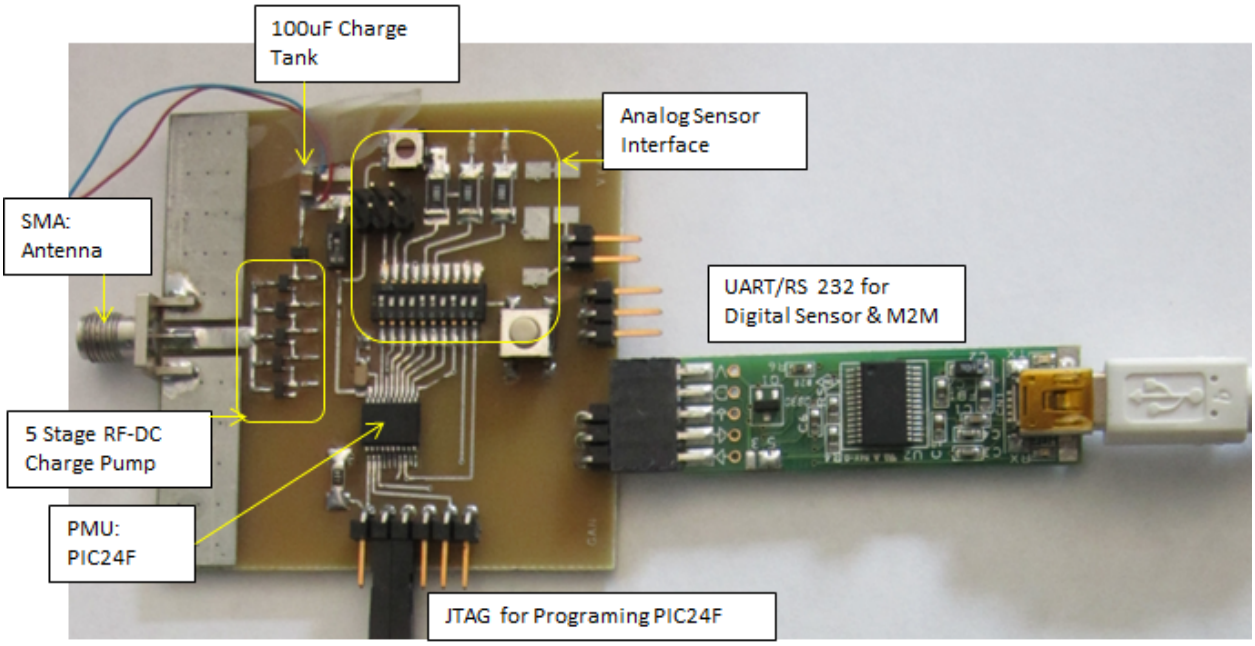

Figure 71. E-WEHP v4 prototype with 5 stage RF-DC Charge pump circuit and PIC24F microcontroller-based PMU.

5.5.1 Single Tone RF-DC Response

The overall loss in the RF-DC charge pumps in E-WEHPs v1, v2, v3 and v4 can be gauged from its input impedance that can be represented as a series RC circuit, with 'R' representing losses including forward-voltage losses of the diodes, and 'C' representing the equivalent capacitance of the charge-pump circuit [*96*] [*97*] [*98*]. During simulation, the circuit parameters, namely capacitors, are optimized to maximize the voltage output across the charge tank capacitor for a given input power level, or conversely reduce the series resistive losses in the circuit at frequencies where the ambient TV signals are present. Low leakage MLCC capacitors with values of 20 pF and 15 pF were used for all the even and odd-numbered capacitors, respectively, shown in **Figure 67**. The input resistances of the RF-DC Charge Pump

circuits were measured using a Rohde and Schwartz ZVA-8 vector network analyzer (VNA) in the 500-700 MHz frequency band, and are shown in **Figure 72** (i)-(iv).

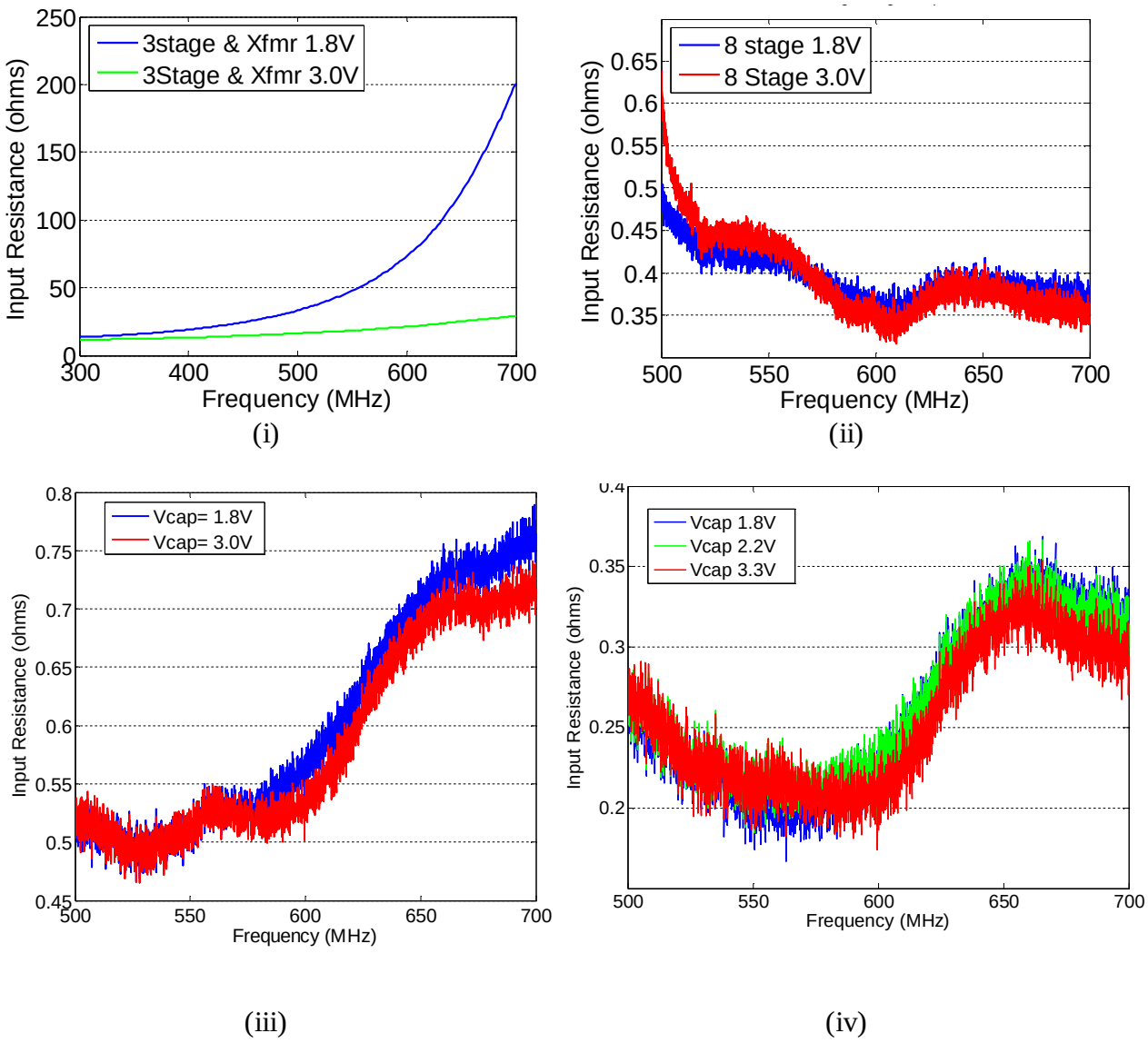

Figure 72. E-WEHP RF to DC Charge Pump Circuit input resistance for charge tank voltages of 1.8 and 3.0V.

(i) E-WEHP v1: RF Transformer with 3 stage RF-DC Charge pump
(ii) E-WEHP v2: 8 Stage RF-DC Charge pump with PIC24F PMU
(iii) E-WEHP v3: 5 Stage RF-DC Charge pump with Analog PMU
(iv) E-WEHP v4: 5 Stage RF-DC with PIC24F PMU

The RF-DC rectifier in E-WEHP v1 shows losses of between 20 and 200 ohms in the frequency band between 500 and 700 MHz as shown in **Figure 72**(i). The high resistance is primarily due to parasitic losses in the way the wires are wound around the core of the transformer. E-WEHPs v2 and v3 exhibited similar resistive losses of between 0.45 and 0.7 ohms in the TV frequency bands. E-WEHP v4 exhibited the lowest RF-DC series loss of between 0.2 and 0.35 ohms in the TV bands.

The basic single tone response of the E-WEHP RF-DC charge pumps are a good gauge to study its basic RF-DC rectifying response at different frequencies within the digital TV bands by eliminating effects of impedance mismatch with respect to the antenna. The input, single-tone power ($P_{Turn\text{-}on}$) required at different TV signal frequencies to charge up the charge tanks to 1.8V and 3.3V is determined using (27) and is plotted in **Figure 73** (i)-(iv) for E-WEHPs v1-v4. The single tone responses shows the RF-DC charge pumps needing the least amount of RF input power between 550 and 600 MHz where most of the TV channels measured in downtown Tokyo and midtown Atlanta are present.

$$P_{Turn-On} = P_{CARRIER} \cdot (1 - |S_{11}|^2) \tag{27}$$

At the frequency of interest in the 500-700 MHz bands, the transformer based RF-DC charge pump topology in E-WEHP v1 requires substantially higher input power levels of between 2 and 3.5 milliwatts to generate DC outputs between 1.8 and 3.0V, respectively, as shown in **Figure 73** (i). The higher RF input power levels are primarily because of losses due to the way the wires are wound around the core of the transformer.

The five-stage and eight-stage RF-DC charge pumps in E-WEHPs v2 and v3 exhibit similar performance requiring between 40 and 75 microwatts of single tone input RF power to

generate DC outputs between 1.8 and 3.0V, respectively, as shown in **Figure 73** (ii) and (iii) [*99*].

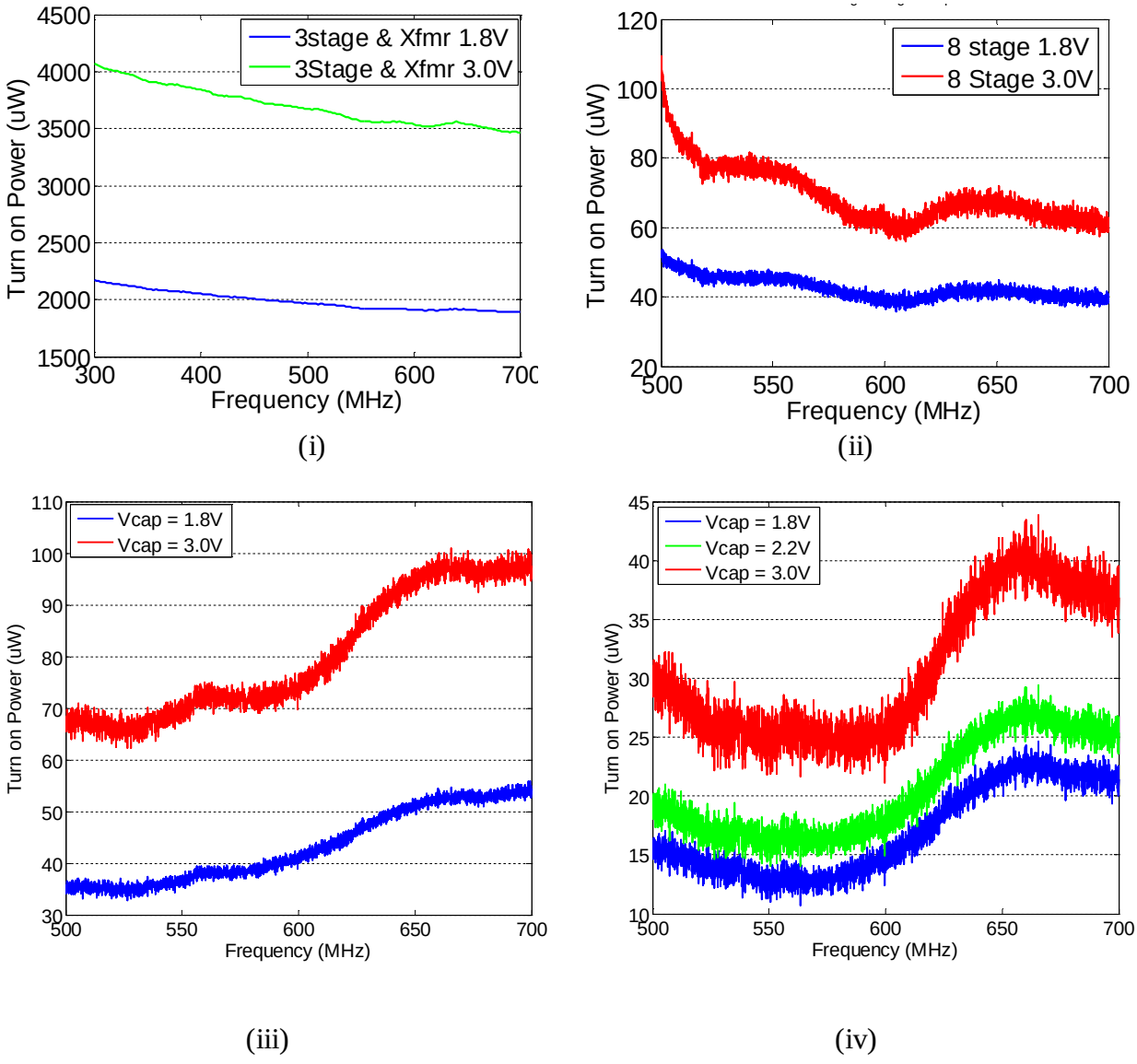

Figure 73. E-WEHP RF to DC Charge Pump Circuit input power for charge tank voltages of 1.8 and 3.0V.

- **(i) E-WEHP v1: RF Transformer with 3 stage RF-DC Charge pump**
- **(ii) E-WEHP v2: 8 Stage RF-DC Charge pump with PIC24F PMU**
- **(iii) E-WEHP v3: 5 Stage RF-DC Charge pump with Analog PMU**
- **(iv) E-WEHP v4: 5 Stage RF-DC with PIC24F PMU**

The three extra stages of the eight stage RF-DC charge pump in E-WEHP v2 offer no extra RF-DC gain due to saturation by the parasitics in the diodes used in the charge pump circuitry. For the type of diode used, the optimized RF-DC charge pump in E-WEHP v4 yields the correct trade-off between output voltage level and power efficiency with respect to the RF input at the frequency of interest. Only between 12 and 22 microwatts of input RF power is needed to generate an output DC voltage of 1.8 whereas between 25 and 40 microwatts of input RF power is needed to generate 3.0V DC output in the TV bands between 500 and 700 MHz as shown in **Figure 73** (iv) [*100*].

High RF-DC sensitivity of E-WEHP v4 makes it ideal for harvesting wireless power from ATSC-standard, Digital TV signals in use in North America shown in **Figure 51** and **Figure 65**, where channels tend to be scattered between 500 and 700 MHz frequency bands. Due to their higher RF-DC sensitivities and use of fewer charge-pump stages, E-WEHPs v3 and v4 were further optimized to harvest wireless power in multi-carrier ISDB-T and ATSC TV signals in Tokyo and Atlanta, respectively.

The RF-DC charge pump circuit in E-WEHP v3 exhibits an input impedance of about 0.52-j7.3 ohms at UHF TV bands with the 100 microfarad charge tank capacitor charged to 1.8V, which is the operating voltage point for the proposed end load. An optimal matching network is designed to match this capacitive RF-DC impedance to the near 50 ohm input impedance of the E-WEHP SBA and log-periodic antennas in the TV bands as shown in **Figure 48** and **Figure 55**. The impedance match minimizes input return losses (S_{11}) in (21), between the antenna and RF-DC charge pump, which maximizes an already low voltage signal at the charge-pump input that is induced by the antenna, which enables trickle charge-flow through the charge pump and into the output charge-tank capacitor.

The matching network in E-WEHP v3 was optimized for the signal measured in downtown Tokyo with the log-periodic antenna shown in **Figure 61**. A mixed L-section matching network comprising of lumped discrete capacitors and distributed transmission line elements is used as shown in **Figure 67** (ii) since it allows for easy tuning of the matching network based on the RF-DC's response to varying input power levels and output loads. The extra phase introduced by the SMA connectors are also included as part of the distributed transmission line network. Capacitors of 1 and 6.6 pF are used for CS1 and CS2 along with the added phase of microstrip to SMA input transition to form an L-section matching network for E-WEHP v3 as shown in **Figure 67** (ii). The matching network gives a 10 dB return-loss bandwidth of 12 MHz over the TV frequency bands.

The matching circuit in E-WEHP v3 is designed so that as the RF-DC charge-tank voltage increases, the matching circuit ensures that the charge-pump's varying impedance is conjugately matched to the 50 ohm log-periodic antenna over the digital TV frequency bands measured in Tokyo as shown in **Figure 74**. The matching network is optimized such that during the initial charge up of the charge tank capacitor at 0.5V, the charge pump's return loss (S_{11}) is greater than 10dB between frequencies of 515 MHz and 527 MHz. At this point the E-WEHP v3 harvests power from digital TV channels #9 (JOMX) and 8 (JOCX) as shown in **Figure 74**. Ensuring over 90% power transfer from one or more ambient wireless TV channels at initial turn-on is critical to ensure further charge build up across the charge tank capacitor. As charge tank voltage varies between 1.8 and 2.0V, the matching network is designed to have a return loss (S_{11}) greater than 10dB between wireless TV channels 8, 6 and 7, where peak ambient wireless power is transduced by the log periodic antenna as shown in **Figure 74**. This ensures maximum power-harvesting from the ambient signals and charge flow into the charge tank capacitor to

replenish it when the E-WEHP's PIC24F enters the Charge/Sleep mode covered in a subsequent section. The L-section matching network was used due to its ease of configurability in dynamically matching the 50 ohm log-periodic antenna to a varying RF-DC charge pump load.

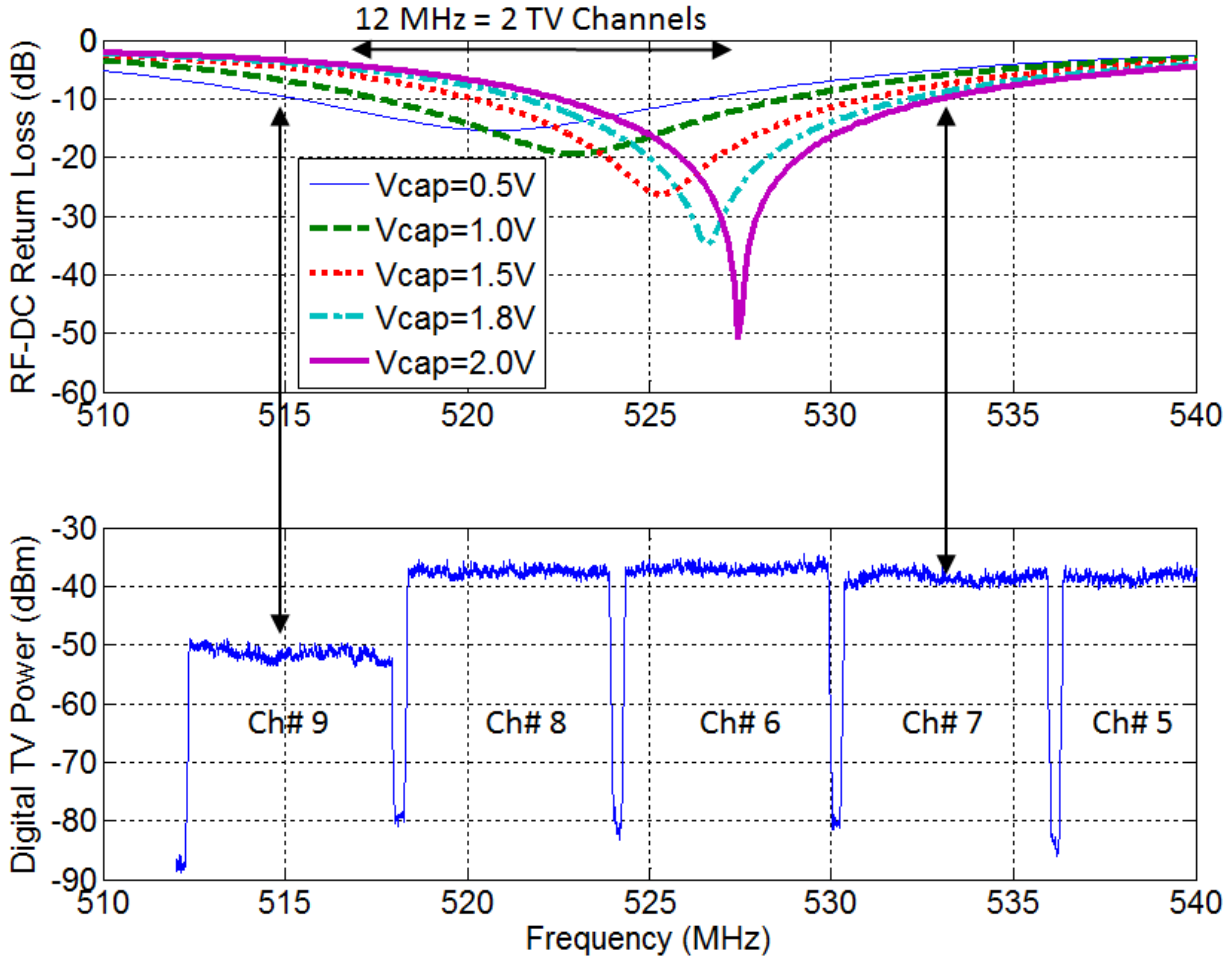

Figure 74. Measured E-WEHP v3 RF to DC Charge Pump input return loss ('S11(f,V_{CAP})') for charge tank capacitor voltage (V_{CAP}) between 0.5 and 2.0V with respect to the wireless digital TV channels measured in the field in Tokyo.

Harvesting power from the scattered TV channels in Atlanta requires the RF-DC to draw more power from fewer channels that are spaced apart in frequency. For power harvesting in Atlanta, the more sensitive E-WEHP v4 with two optimized L-section matching circuits was used. Matching circuits 1 and 2 were optimized to match E-WEHP v4's RF-DC charge pump to the 50 ohm Log-periodic antennas over the combined CBS and IND TV channels, and MyTV and Fox TV channels, which together induce the maximum amount of channel power across the log-periodic antenna within a given bandwidth as shown in **Table 8** and **Figure 75**. For the final design of E-WEHP v4, matching circuit 1 was used due to the continued presence of wireless TV power within a 12 MHz bandwidth window that allows for a higher charge build up at the RF-DC output compared to matching circuit 2. Matching circuit 1 ensures power-transfer resonance between 500 and 512 MHz over the CBS and IND TV channels as the RF-DC's output charge tank charges from 1 to 3.3V as shown in **Figure 75**. By using a multi-section matching and a shorter transmission-line network, the overall return-loss bandwidth can be increased up to a maximum of 71 MHz, which is the theoretical Bode Fano limit for the RF-DC's reactive loads at the TV bands [*88*].

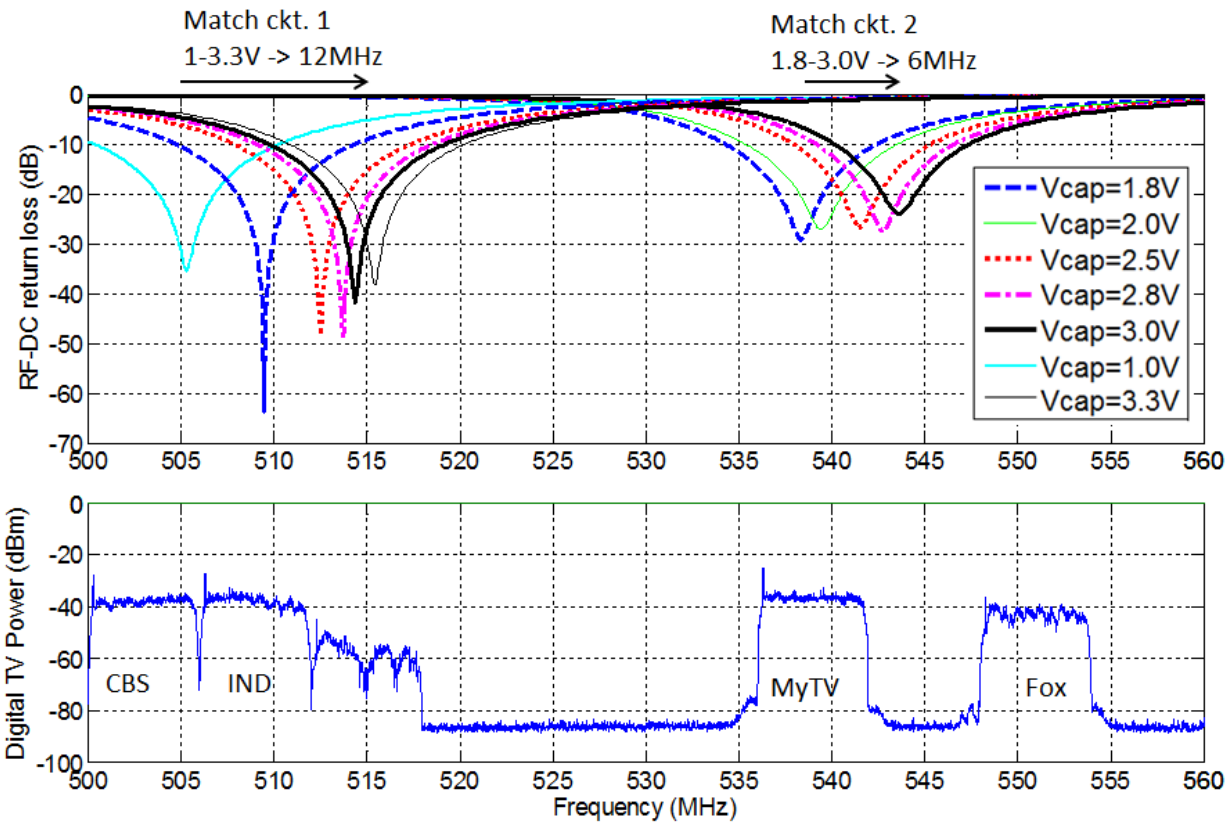

Figure 75. Measured E-WEHP v4 RF to DC Charge Pump input return loss ('S11(f,VCAP)') for charge tank capacitor voltage (VCAP) between 1 and 3.3V with respect to the wireless digital TV channels measured in the field in Atlanta.

5.5.2 Multi-tone RF-DC Response

As shown in sections 5A and 5B, modern digital TV signals in Tokyo and Atlanta are transmitted using multiple carriers in each of the multiple TV channel simultaneously, which is what allows 1080p of resolution to be displayed in television sets worldwide. In order to characterize the E-WEHPs' response to such multi-carrier TV signals, a Rohde and Schwarz SMJ100A RF vector signal generator (SigGen) and a Tektronics RSA 30408A real time spectrum analyzer (RTSA) were used in the lab to generate multiple carriers, and emulate Digital TV signals observed in the air in downtown Tokyo as shown in **Figure 76**. The output charge tank voltage of the E-WEHP RF-DC was measured with a Tektronics DPO7354 oscilloscope using a high impedance probe.

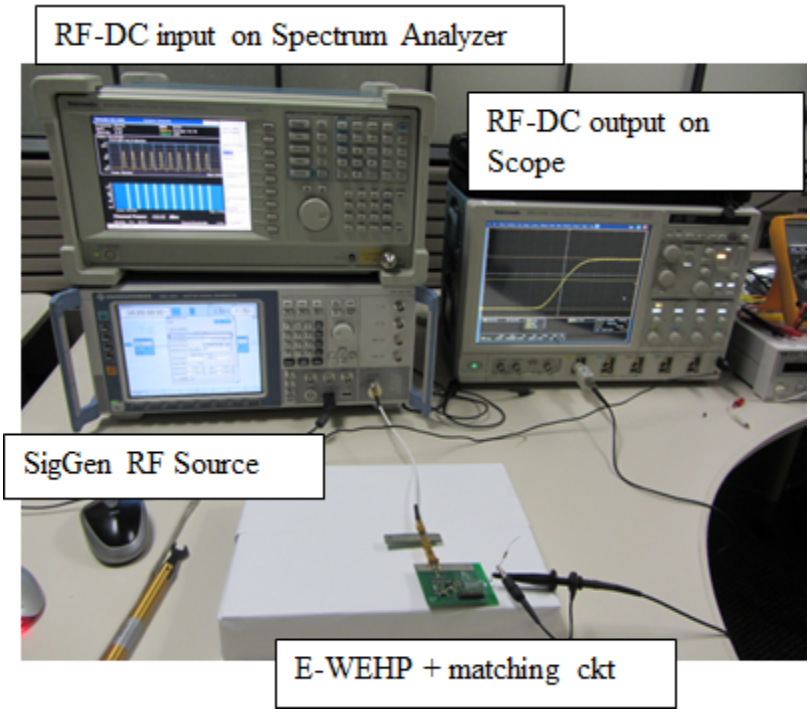

Figure 76. Measurement setup to measure multi-tone response of E-WEHP v3 RF-DC Charge pump circuit.

To gauge the E-WEHPs response to the number of tones or carriers in a single TV channel at first, between 1 and 12 tones spaced 500kHz apart within a 6MHz bandwidth between 537 and 543 MHz at two constant carrier levels of -18dBm and -22dBm were fed into the matched RF-DC circuit in E-WEHP v3 as shown in **Figure 77**. The RF-DC was terminated at the output with a 1 mega-ohm load to emulate the proposed end load of a microcontroller.

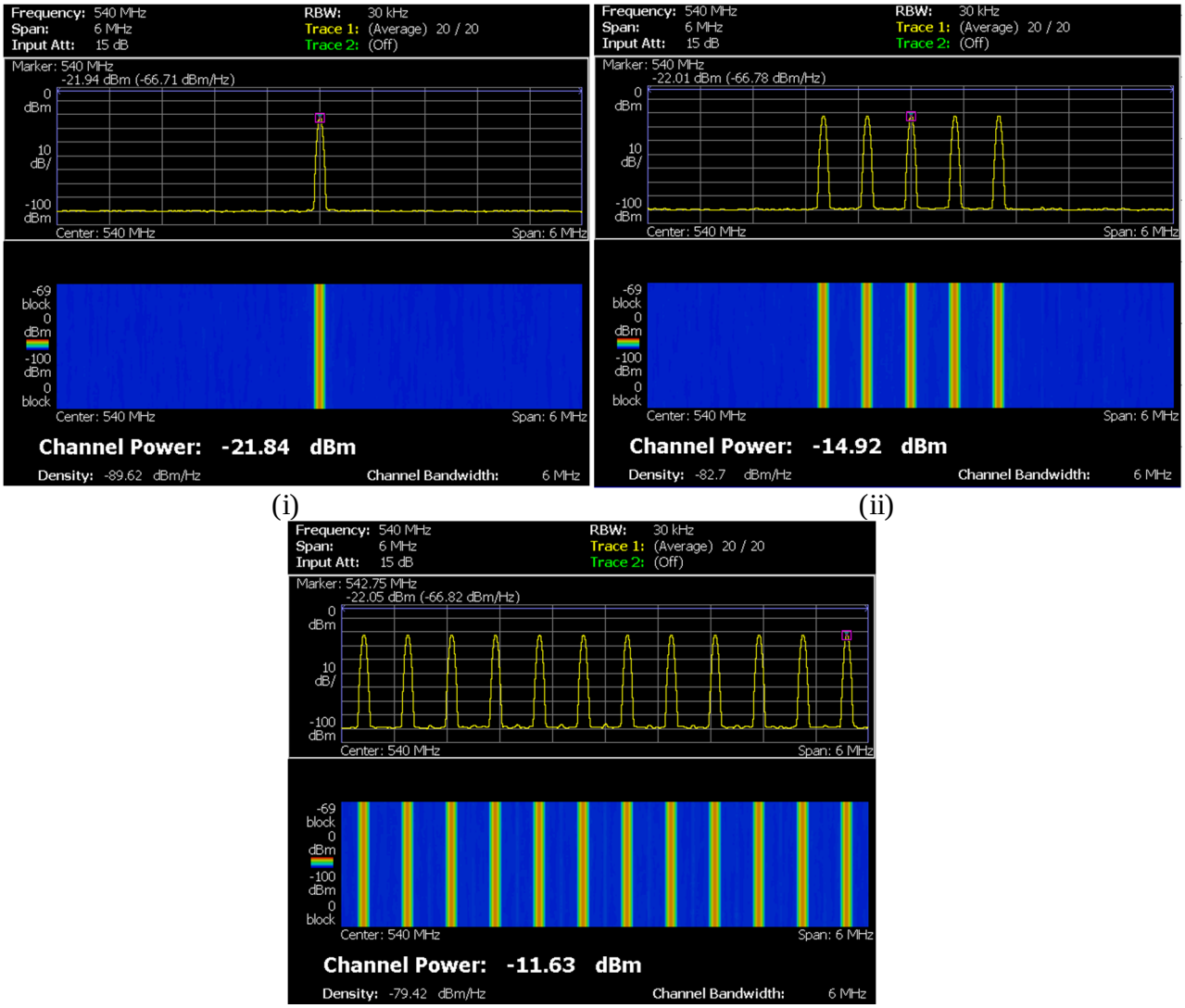

Figure 77. Multi-tone signal inputs generated by Rohde and Schwarz SMJ100A Vector signal generator to test multi-tone response of E-WEHP RF-DC circuit.

The DC output voltages of the RF-DC charge pump circuit in E-WEHP v3 with respect to the number of tones for carrier levels of -18 and -22 dBm are plotted in **Figure 78**. At input carrier levels of -22dBm (6.3 microwatts) and -18 dBm (15.8 microwatts), the output of the RF-DC yields close to 0V as per E-WEHP v3's single tone response shown in **Figure 73** (iii). However each extra tone fed into the E-WEHP v3 RF-DC charge pump is observed to increase the RF-DC output by 1.0V with a -22dBm carrier level and by 1.5V with a -18dBm carrier level. This performance is counter-intuitive to the behavior of a diode which can be expected to disallow charge build-up if the RF-DC's input is lower than the forward voltage of its diode.

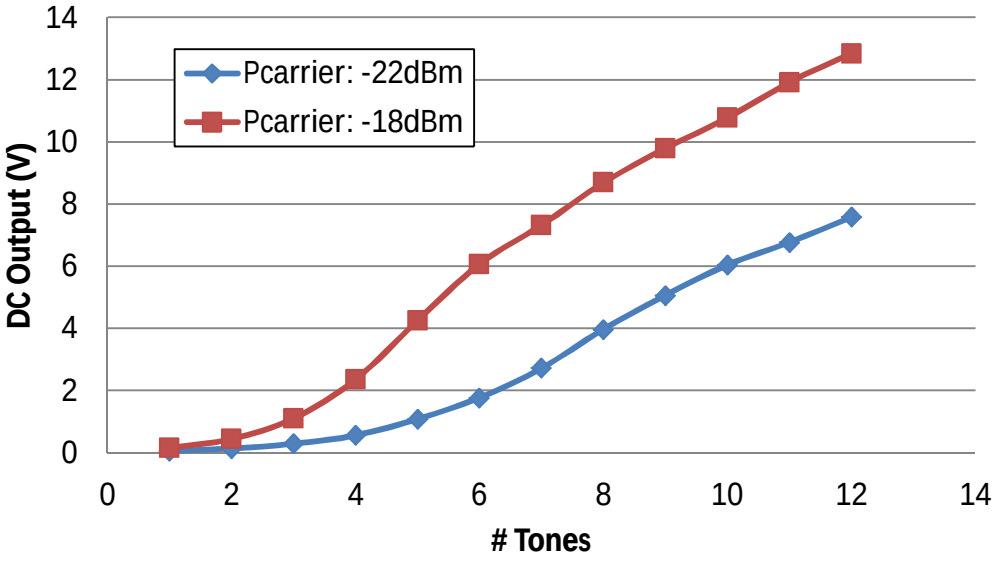

Figure 78. E-WEHP v3 RF-DC Charge pump output voltage response to multi-tone RF input signal.

Consequently, the efficiency of the RF-DC charge pump increases by 10% and 15% with each increase in tone or carrier at input carrier levels of -22 and -18dBm, respectively, as shown in **Figure 79**. Wireless digital TV signals broadcasted using ISDB-T and ATSC standards

contain close to 5567 carriers or tones per 6MHz channel, thereby making it an ideal choice for harvesting wireless power over long range.

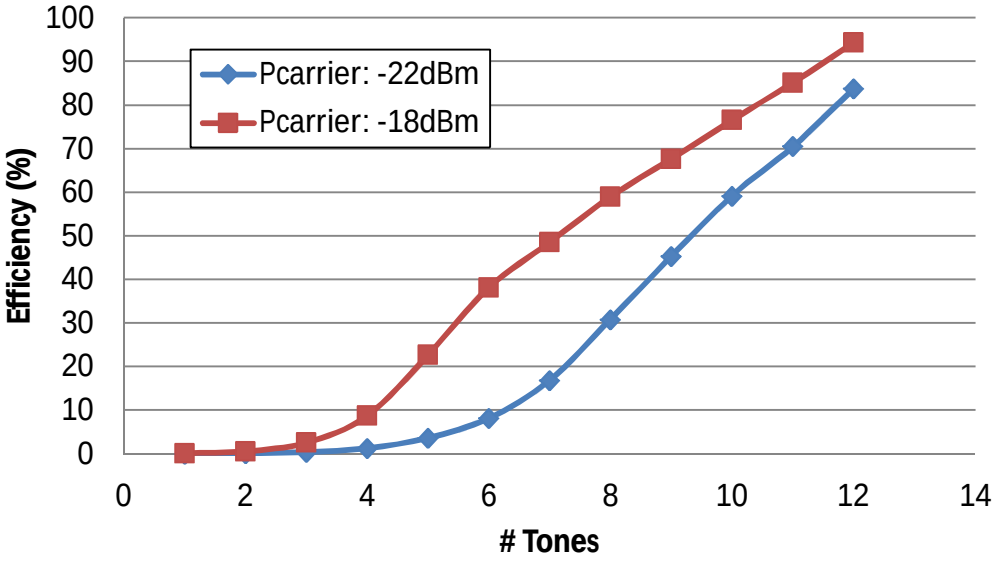

Figure 79. E-WEHP v3 RF-DC Charge pump efficiency with respect to multi-tone RF input signal.

Peak envelope power limits of the Rohde SMJ100A measurement equipment do not allow generating 5567 subcarriers across each of the 9 TV channels that are present under ISDB-T digital TV standards measured in Tokyo shown again in **Figure 80** (i). However using 1860 subcarriers each 29 kHz apart for a multicarrier baseband signal around a carrier frequency of 539 MHz with a chirp type power distribution scheme does allow for a 9 TV channel wide signal with the roughly the same channel power as in the field to be emulated within the lab without exceeding the peak envelope power limit of the Rohde SigGen, albeit with lower carrier amplitude as shown in **Figure 80** (ii).

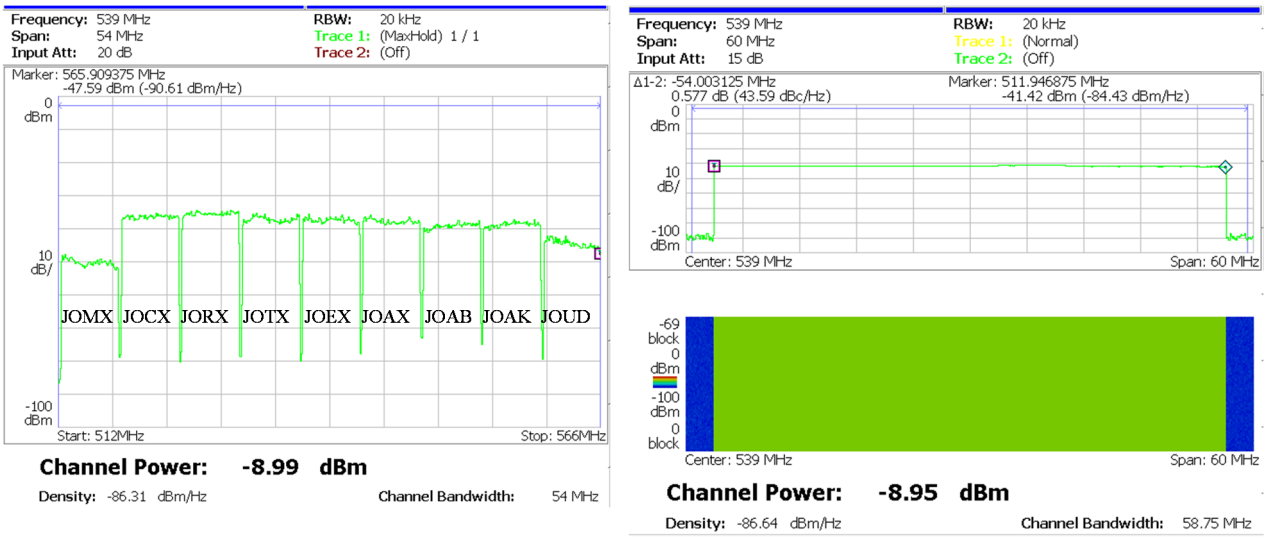

(i) (ii)

Figure 80. (i) Multi-carrier wireless ISDB-T TV signals captured by Log-periodic antenna from TV tower 6.5 km away in Tokyo (ii) ISDB-T like signal generated in lab using Rohde and Schwarz SMJ100A Vector Signal Generator to test E-WEHP v3 RF-DC Charge pump.

The performance of the E-WEHP v3 was tested with the emulated ISDB-T like TV signals in the lab for different channel power levels, and fed to its input with 1 M-ohm and 18 M-ohm loads across its output charge tank capacitor. The loads were placed to emulate the proposed end load which is a PIC24F 16 bit embedded microcontroller unit (MCU) operating in a low clock (32 kHz) active mode and a deep sleep mode. The microcontroller's deep sleep mode is when the E-WEHP transfers wireless power from the air into the charge tank capacitor in the Sleep/Charge mode for the microcontroller to operate for limited duty cycles later on during the Active/Discharge mode. Since the wireless power harvested from the air is not used to directly power a load but using a collect first (Charge/Sleep) and use later (Discharge/Active) modes, we use the relationship in (28) to gauge the efficiency of the E-WEHP RF-DC charge pump circuit.

In (28), the energy collected by the E-WEHP RF-DC charge pump is dependent on the charge tank capacitance (C_L) and it's charged up voltage (V_{CAP}), which is chosen to be around the operating voltage of the end device i.e. 1.8V for embedded and wireless ICs. The energy supplied by the ambient wireless TV signals through the log-periodic antenna is the product of the input channel power ($P_{All\text{-}CHANNELS}$) supplied across all 9 TV channels during the charge up time 'T_{VCAP}' to 1.8V at the charge tank. Calculating efficiency in terms of energy, which is a function of power and time, is a better gauge of the energy-harvesting efficiency of the E-WEHP given the multi-channel make up of Digital TV signals and E-WEHP's time varying response to it based on the charge tank's voltage level as shown in **Figure 74**.

$$\eta_{ALL-CHANNELS} = \frac{Energy\ Out}{Energy\ In\ all\ channels} = \frac{{}^{1}/_{2} \cdot C \cdot {V_{CAP}}^{2}}{P_{ALL-CHANNELS} \cdot T_{VCAP}} \cdot 100 \quad (28)$$

Even though all nine TV channels are incident at the input of the E-WEHP's RF-DC Charge pump, at any given time it is only power contained in 2 channels that actually contribute to the voltage build-up at its output charge tank capacitor. This is due to the 12 MHz return loss bandwidth of the RF-DC Charge pump circuit shown in **Figure 74**. The efficiency of the E-WEHP RF-DC charge pump only with respect to the input power causing the charge up is determined using (29), where the term '$P_{2\text{-}CHANNELS}$' is the channel power contained within 2 TV channels. The efficiencies of the E-WEHP for an output charge tank voltage (V_{CAP}) of 1.8 V for output loads of 1 M-ohm and 18 M-ohms using (29) with respect to the total input channel power across all 9 Digital TV channels are shown in **Figure 81**.

$$\eta_{2-CHANNELS} = \frac{Energy\ out}{Energy\ in\ 2\ channels} = \frac{{}^{1}/_{2} \cdot C_L \cdot {V_{CAP}}^2}{P_{2-CHANNELS} \cdot T_{VCAP}} \times 100 \quad (29)$$

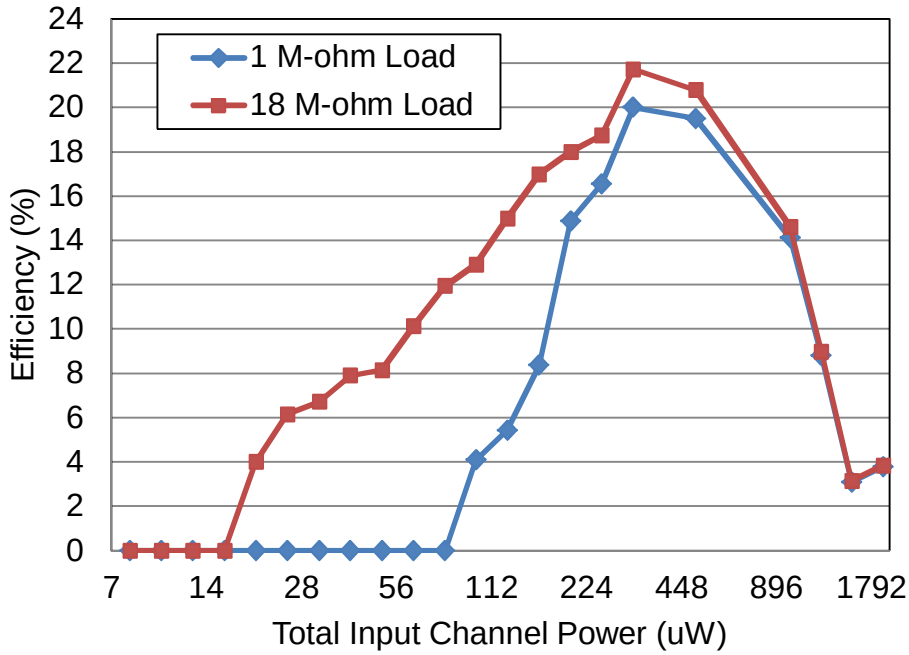

Figure 81. E-WEHP v3 RF-DC energy conversion efficiency versus channel power of ISDB-T-like multi-carrier input signal.

The E-WEHP v3 RF-DC charge pump circuit fed with digital TV signals emulated in the lab with the SigGen show maximum energy efficiencies of 19.50% and 21% for 1M-ohm and 18 M-ohm loads across the charge tank capacitor, respectively. Around total channel power levels of -8.99 dBm (126 microwatts) observed at the measurement point, lab tests on the E-WEHP v3 yield efficiencies of between 5 and 15% for a 1 M-ohm and 18 M-ohm output loads across the charge tank capacitor, respectively. Output voltage measurements on the E-WEHP v3 under lab conditions with a Tektronics oscilloscope (Scope) show the 100 µF output charge tank capacitor voltage rises to 2.32V in 406 seconds for a 1 M-ohm output load with an input channel power

level of around -8.99 dBm (126 microwatts) as shown in **Figure 82**. At the same channel power levels at its input, the E-WEHP v3 gives out in excess of 10.32 volts with an 18 M-ohm load across the 100 µF charge tank.

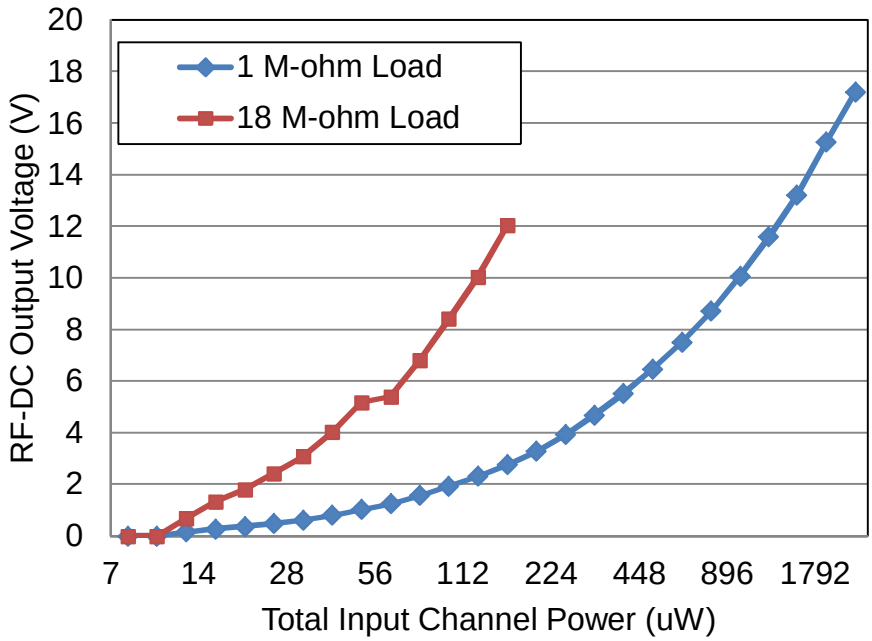

Figure 82. E-WEHP v3 RF-DC DC output voltage versus channel power of ISDB-T-like multi-carrier input signal.

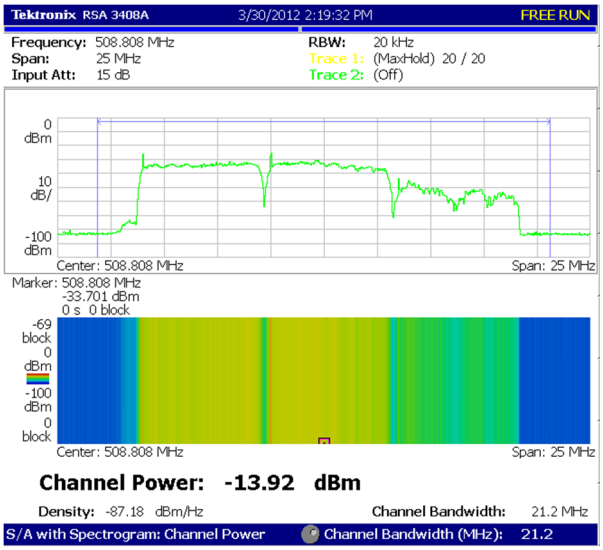

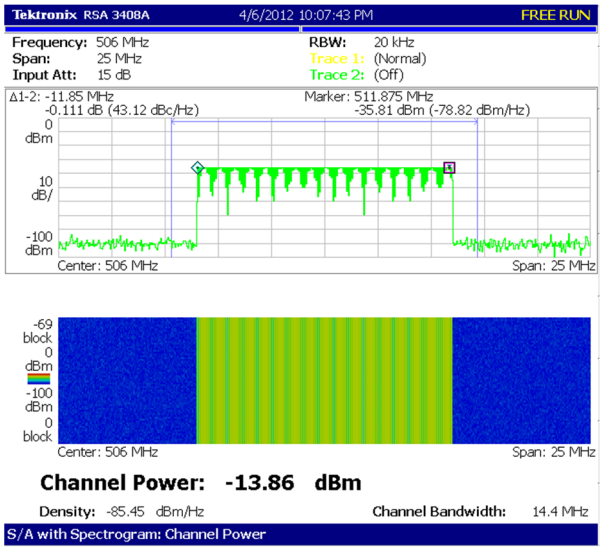

(i) (ii)

Figure 83. (i) CBS and IND TV signals captured by Log-periodic antenna 6.0 km from source in Atlanta (ii) CBS and IND-like signals generated in lab using Rohde and Schwarz SMJ100A Vector Signal Generator to test E-WEHP v4 RF-DC Charge pump.

The multi-tone response of the RF-DC charge pump in E-WEHP v4 was measured using a 2-channel wide multi-carrier signal generated by the SMJ-100A similar in power and bandwidth to the CBS and IND signals captured by the Log-periodic antenna in Atlanta as shown in **Figure 83**. The E-WEHP v4's RF-DC output voltage to such a signal for varying amounts of channel power is shown in **Figure 84**. Based on lab measurements, E-WEHP v4 is expected to yield a little less than 2 V for input channel power of -13.92 dBm (40.55 microwatts) that was measured by the Log-periodic in Atlanta.

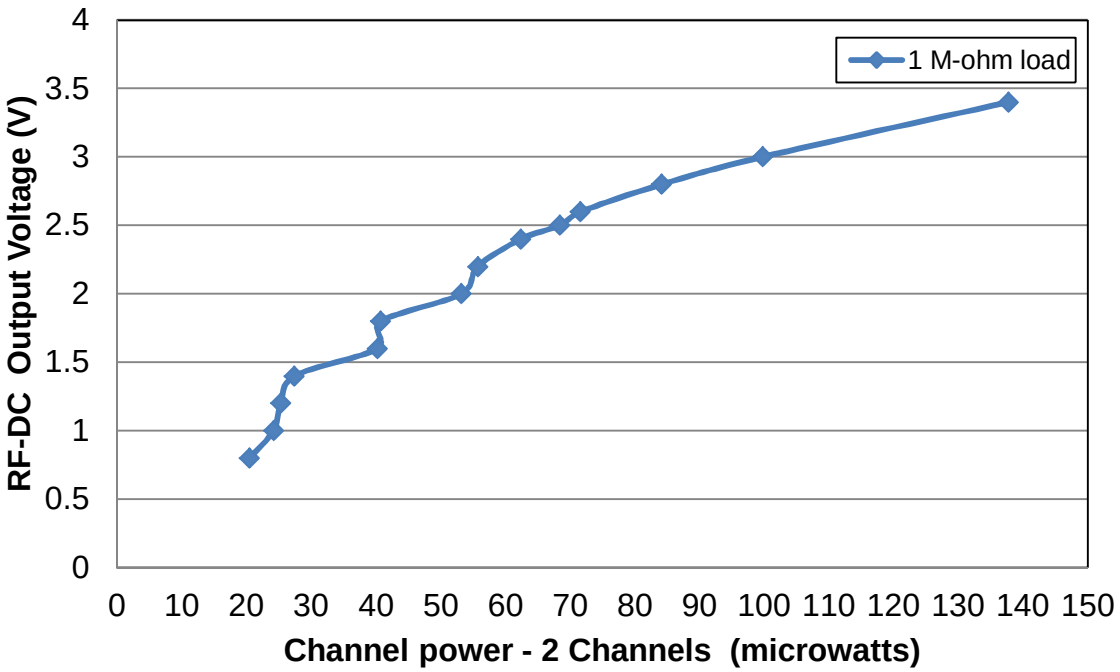

Figure 84. E-WEHP v4 RF-DC DC output voltage versus channel power in CBS and IND-like multi-carrier input signal.

A comparison of the multi-tone efficiencies between E-WEHPs v3 and v4 is shown in **Figure 85**. Lab measurements show v4's RF-DC charge pump exhibiting roughly twice the efficiency of v3. The E-WEHP v4 RF-DC charge pump has efficiencies between 30 and 70% when used with input channel power levels of between -10 dBm (99.8 µW) and 5dBm (3.17mW). The higher sensitivities are useful in harvesting more power from fewer TV channels or lower carrier levels as is the case with digital TV broadcasts in North America shown in the subsequent section.

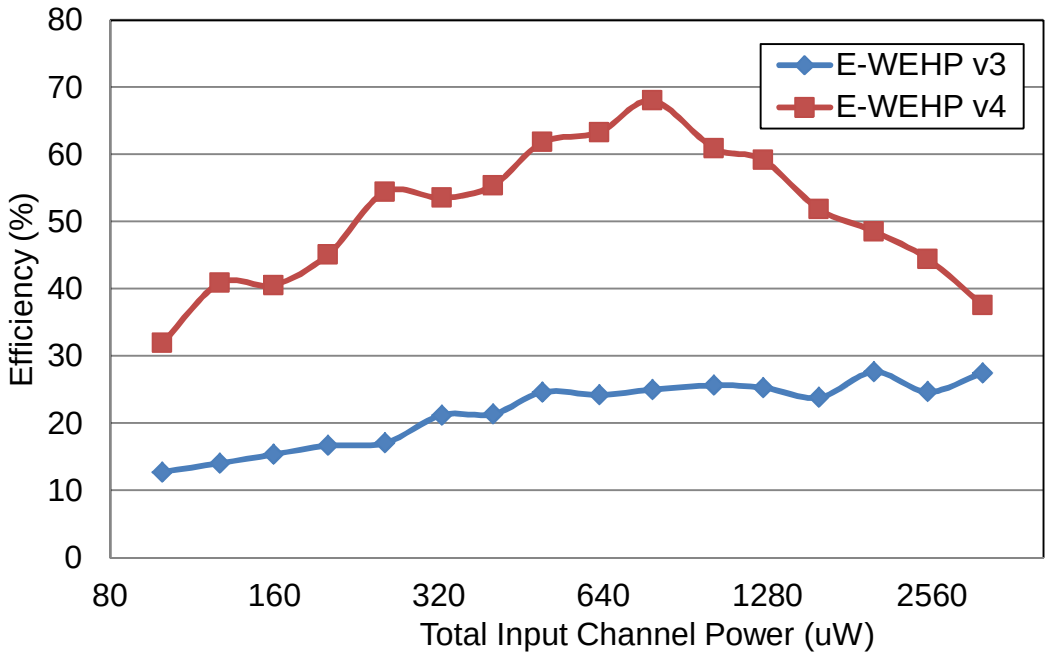

Figure 85. RF-DC energy conversion efficiency comparison between E-WEHP v4 for ISDB-T like multi-carrier input signals with 1 mega-ohm output load.

5.6 Field Measurements

The E-WEHP v3 prototype was then tested in the field by orienting its log periodic antenna towards a known TV broadcast source atop the Tokyo TV 6.5 km away from the lab as shown in **Figure 60** and **Figure 86**. Based on the site survey carried out in Tokyo in the preceding section and shown in **Figure 60**, the transmit source for the measured radiation in the field are nine TV channels that are broadcast from atop the Tokyo TV Tower, 6.5 km south as shown in **Figure 86**. With the E-WEHP's Log-periodic antenna aligned to the broadcast source, the RF-DC's output 100 µF charge tank capacitor charges up to 4.18V in 120 sec from the ambient wireless TV signals as shown by oscilloscope measurement in **Figure 87** (i) [*101*].

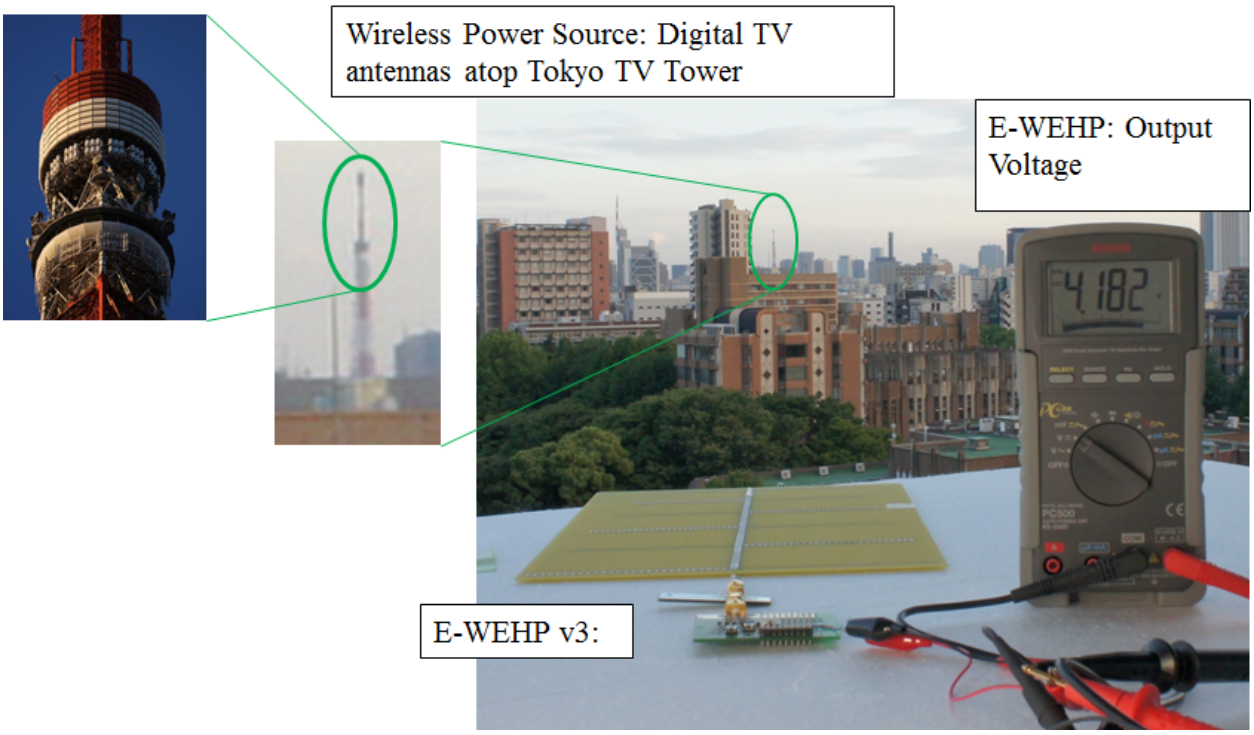

Figure 86. Field measurement in downtown Tokyo with E-WEHP v3 prototype harvesting wireless energy from wireless digital TV signals broadcasted from atop the Tokyo TV tower 6.5 km away.

E-WEHP v3 yields a higher voltage in a shorter period of time during measurements in the field in downtown Tokyo than in the lab as shown in preceding sections. This higher output was primarily due to the measured wireless TV signals in air at the field having a higher crest factor (peak to average power ratio) while still having the same channel power in the frequency domain as compared to the SigGen emulated signals as can be seen in **Figure 80** (i) and (ii). In the field, the wireless TV signals in the air transduced by the E-WEHP v3's antenna into the RF-DC charge pump have TV channels with maximum carrier levels of close to -37dBm (158.5 nW) (TV channel numbers: 8,6,7,5,2 and 1) and minimum carrier levels of -50dBm (TV channel# 9) to yield a total channel power level across all 9 TV channels of -8.99dBm including the nulls in-between each of the TV channels as shown in Fig. 8. By comparison the TV signals emulated in the lab using the SigGen had peak carrier levels limited to -41.42dBm (72.1 nW) across all nine channels to yield the roughly the same channel power level of -8.95 dBm in order not to exceed the SigGen's peak envelope power limit [*102*]. Higher amplitude tones at the input of the RF-DC charge pump have the effect of lowering the loss across each of its schottky diodes resulting in higher amounts of wireless trickle charge flowing in, which result in higher voltage output and conversion efficiency. As a result the performance of the E-WEHP v3's RF-DC charge pump circuit yields higher voltage output and efficiency in the field in Tokyo than under lab conditions [*101*].

The output current that E-WEHP produces from the ambient wireless TV signals is the sum of the current charging up the charge tank capacitor ($C_L.dV_{CAP}/dt$) and the current consumed by any load across it plus any leakages through them ($I_{C\text{-}LEAK}$) as in (30) where 'I_{MCU}' is the current consumed by the end load comprised of an embedded microcontroller and 'V_{CAP}/R_{PROBE}' is the current consumed by the high impedance scope probe used to measure the E-WEHP output

charge profile. The Tektronics high impedance probe used to measure E-WEHP performance at the measurement point has an impedance of 1 megaohms (R_{PROBE}), and introduces leakages of the order of microamperes at the E-WEHP v3 output, which has to be accounted for such low power measurements. The E-WEHP v3 output voltage typically saturates to a maximum, when its output current sourced from ambient wireless TV signals equals the current consumed in any load across the charge tank along with any of its leakages. The E-WEHP v3 output current measured in the field is shown in **Figure 87** (ii) [*101*].

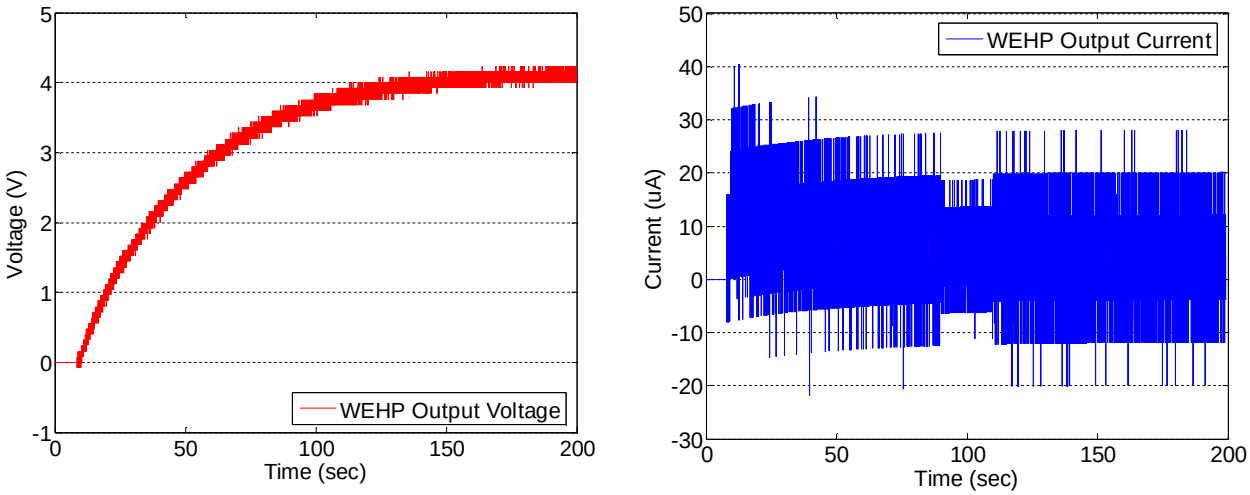

(i) (ii)

Figure 87. E-WEHP v3 output voltage and current measured in the field showing charge up from power harvested from ambient wireless TV signals broadcasted from Tokyo TV Tower 6.5 km away.
(i) E-WEHP v3 charge-tank voltage showing charge up from 0 to 4.18V in 120 sec.
(ii) E-WEHP v3 charge tank current output current measured.

The E-WEHP output shows substantially higher order noise ripples due to environmental noise, multi-path effects, and RF reflections within the RF-DC charge pump itself, which was post processed to filter the noise out using an averaging, low-pass, moving filter in Matlab as shown by the plot in **Figure 88**. In the field, 6.5 km from the wireless TV broadcast sources, the

E-WEHP is capable of continuously sourcing between 4.1 and 8.25 microamperes at output voltages of between 4.1 and 1.8V, respectively. At these output voltages, total output power given by the E-WEHP is between 15 and 17 microwatts, which are between 26.2 and 29.7% of the wireless power present within 2 TV channels transduced by the E-WEHP antenna in the field. The E-WEHP output saturates to 4.1V when its output current draw is equal to the 4.1 microamperes, consumed through the 1 mega-ohm oscilloscope probe.

$$I_{E-WEHP} = C_L \cdot \frac{dV_{CAP}}{dt} + I_{C-LEAK} + \frac{V_{CAP}}{R_{PROBE}} + I_{MCU} \tag{30}$$

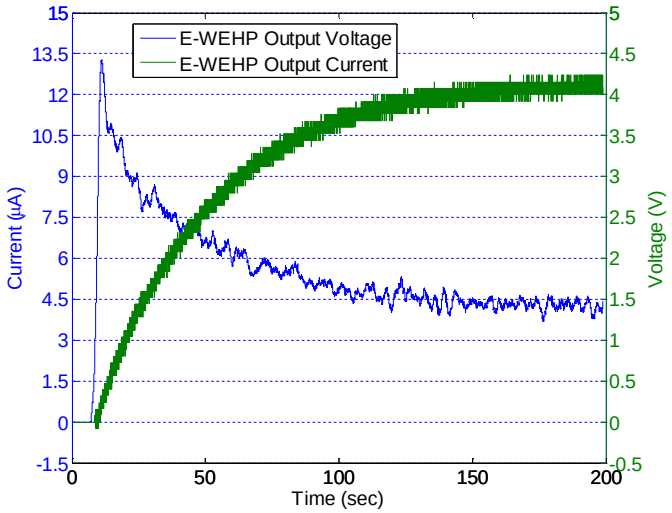

Figure 88. E-WEHP v3 output voltage and current measured in the field after filtering out higher frequency noise ripples introduced by the environment and the E-WEHP RF-DC charge pump circuit.

In addition to Tokyo, the E-WEHP v3 prototype was also tested in the field in Midtown Atlanta. The E-WEHP v3 RF-DC charge pump with its matching network was connected to the SBA antenna, which was pointed towards two TV broadcast towers 6.0 km away in the north-east direction as shown in **Figure 89**. Four TV channels CBS, IND, MyTv and Fox are broadcast from the TV towers towards which the optimum gain direction of the SBA antenna was pointed. The total wireless power transduced across the SBA antenna from the four TV channels as measured by a Tektronics RSA30408A real time spectrum analyzer is shown in **Figure 90**.

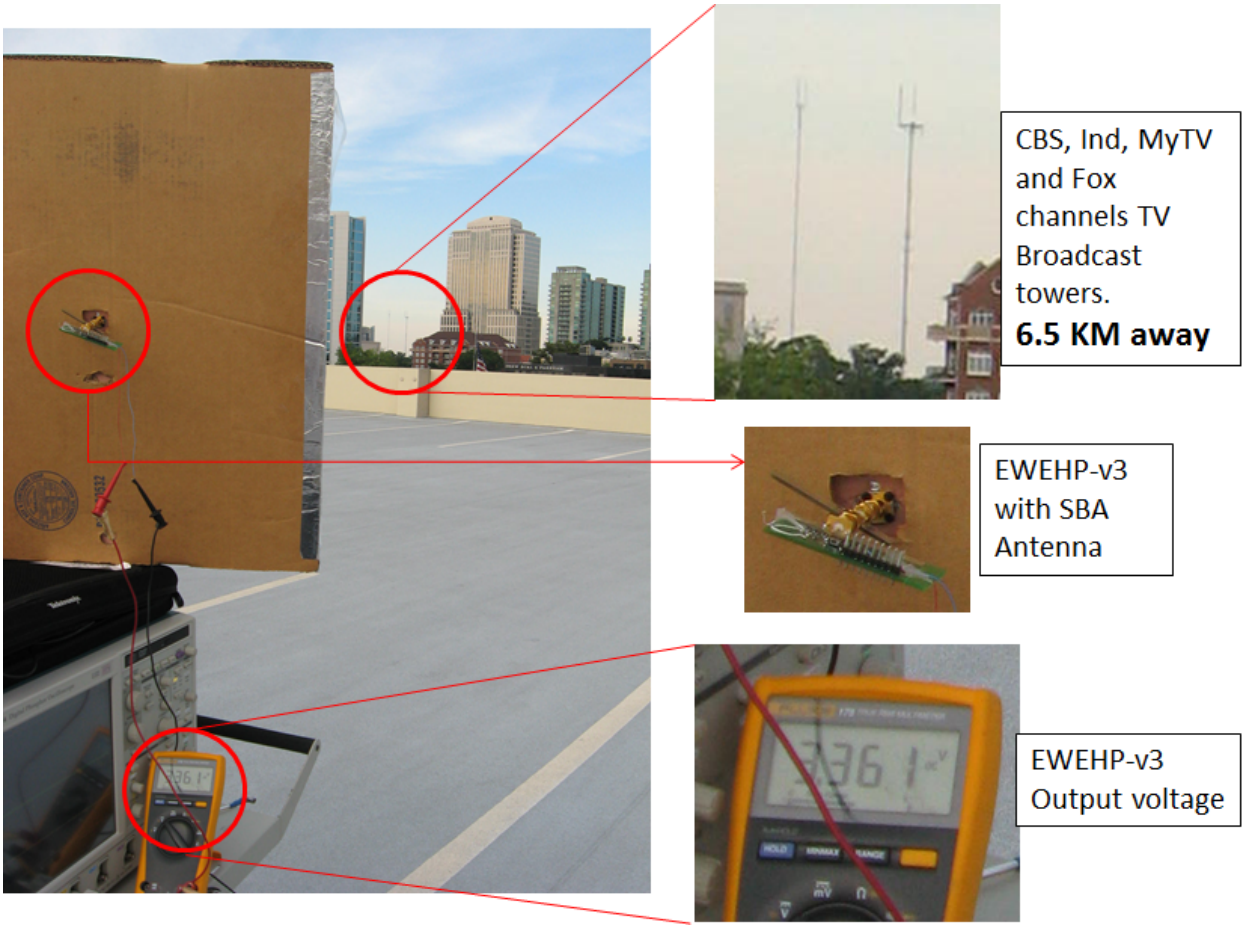

Figure 89. Field measurement with E-WEHP v3 prototype and SBA antenna harvesting wireless energy from wireless digital TV signals broadcasted from atop TV towers 6.0 km away in Midtown Atlanta.

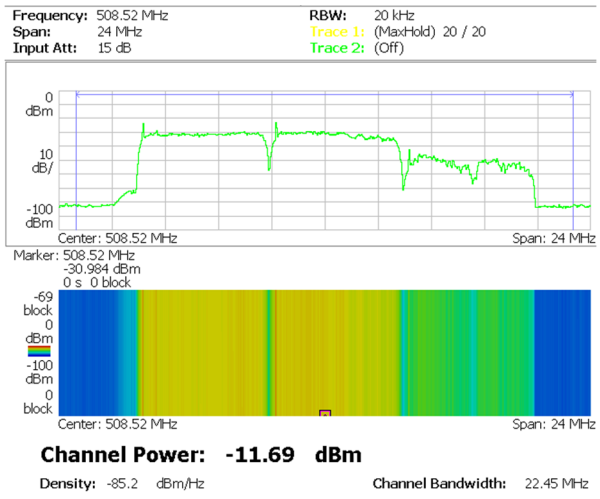

(i)

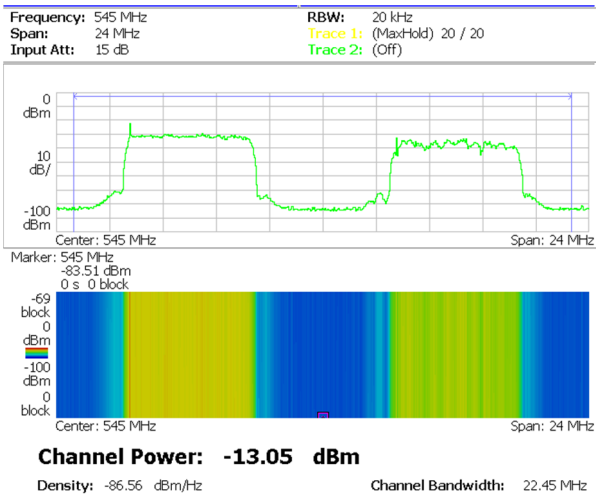

(ii)

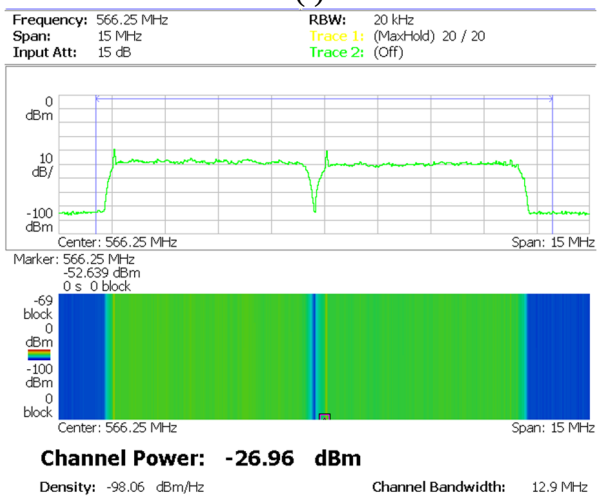

(iii)

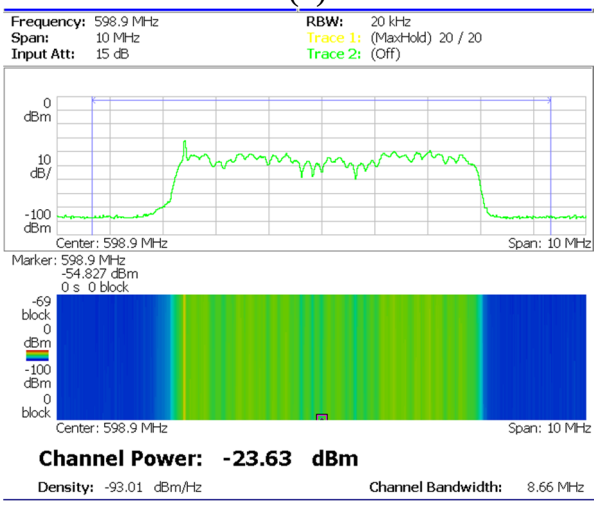

(iv)

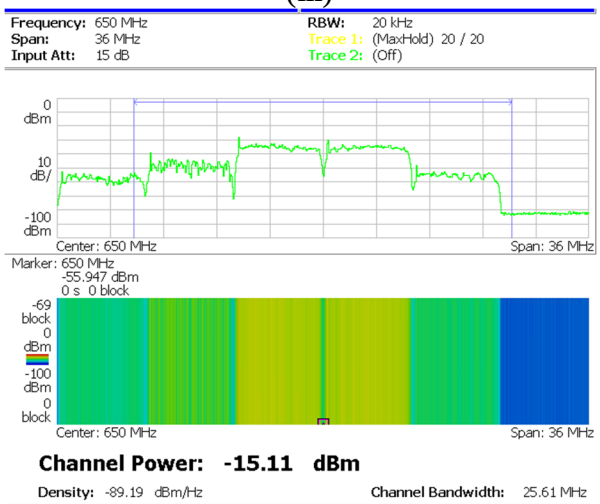

(v)

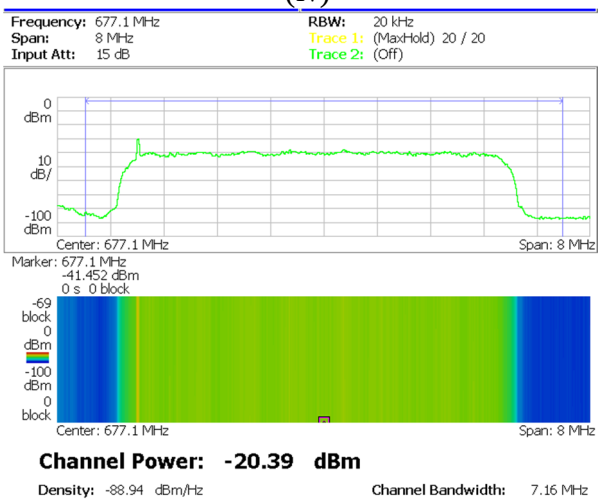

(vi)

Figure 90. Power from different wireless TV channels transduced across SBA antenna in

Midtown Atlanta.

(i) TV Channels: CBS and IND
(ii) TV Channels: MyTV and Fox
(iii) TV Channels: unknown
(iv) TV Channels: WDTA
(iv) TV Channels: ETV, CW, TBN and 2 unknown
(v) TV Channels: Univision

The aggregate of the power transduced across the SBA antenna when pointed in the North-East direction from the Georgia Tech campus in Midtown Atlanta is measured with the Teltronics RSA 30408A real time spectrum analyzer and is approximately 163.6 µW, with the bulk of it due to CBS, IND, MyTV and Fox TV channel broadcasts. Unlike the TV signals measured in downtown Tokyo, TV channel broadcasts are scattered within the 500-700 MHz bandwidth, making it hard to characterize the E-WEHP v3's response to it under lab conditions given the limitations of the Rohde and Schwarz SMJ100A SigGen. However, based on the RF-DC characterization done with adjacent multi-channel signals shown in **Figure 82**, E-WEHP v3 output can be estimated to be over 2.762 V when fed with the TV signals induced across the SBA antenna shown in **Figure 90**. Field measurement of the E-WEHP v3 RF-DC charge pump with the SBA antenna shows the output charge tank charging to 3.361V as shown in **Figure 89**.

The miniaturized log-periodic antenna was also tested on the Georgia Tech campus in Midtown Atlanta by aligning its end-fire direction towards the two known TV broadcast towers in the North-East direction as shown in **Figure 91**. Given the 100 MHz return loss bandwidth of the Log-periodic antenna, only power from seven TV channels are transduced by the antenna with the bulk of the power due to CBS, IND, MyTV and Fox TV channels as shown in **Figure 92**. The combined power due to the seven TV channels aggregates to a total channel power level of 74.6 microwatts at the output of the Log-periodic, which is less than half of what is transduced across the SBA antenna. Based on the E-WEHP v3 characterization in **Figure 82,** its RF-DC

charge pump output is expected to yield only 1.5V, which makes it unsuitable to operate embedded microcontrollers which require operating voltages between 1.8 and 5V. However, the log-periodic antenna combined with the E-WEHP v4, which has twice the RF-DC sensitivity of E-WEHP v3 as shown in **Figure 73** (iii) and (iv), can be expected to yield roughly twice the DC output voltage for the same amount of input RF channel power. Field measurement of the Log-periodic with the E-WEHP v4 carried out in Midtown Atlanta is shown in **Figure 91**, and shows the output charge tank charging to an output voltage of 3.26V in about 200 seconds [*100*].

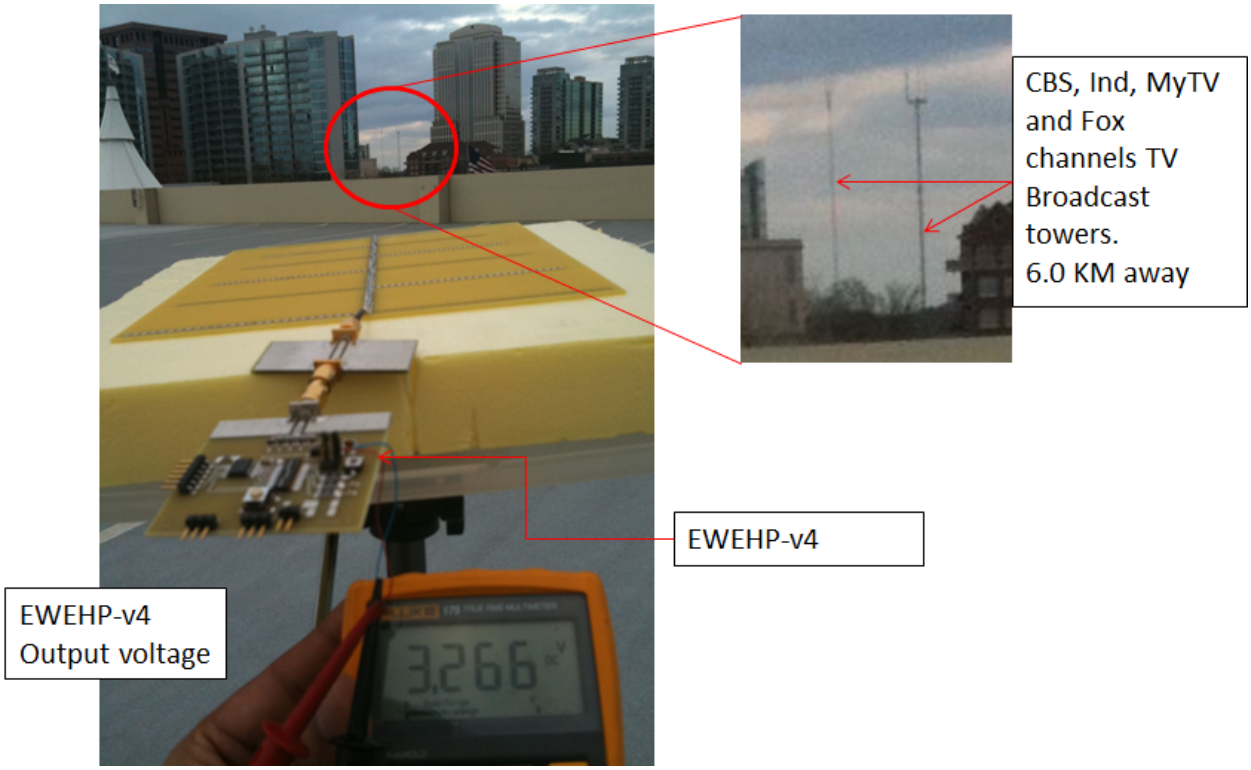

Figure 91. Field measurement with E-WEHP v4 prototype and Log-periodic antenna harvesting wireless energy from wireless digital TV signals broadcasted from atop TV broadcast towers 6.0 km away in Midtown Atlanta.

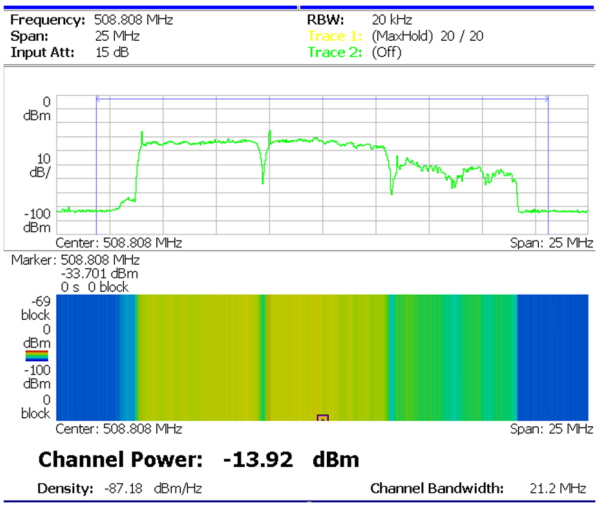

(i)

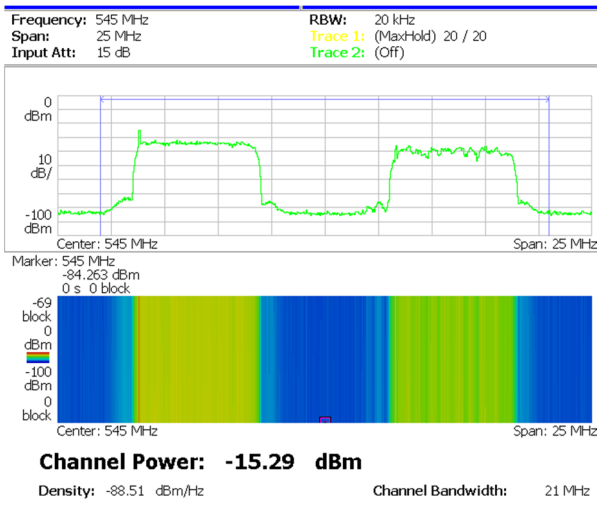

(ii)

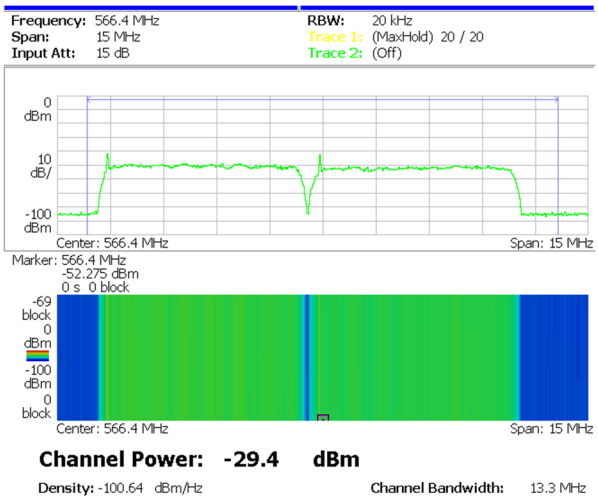

(iii)

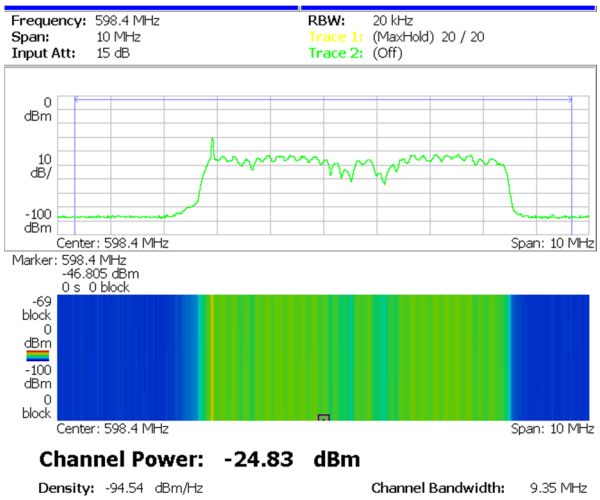

(iv)

Figure 92. Power from different wireless TV channels transduced across Log-Periodic antenna in Midtown Atlanta.

(i) TV Channels: CBS and IND
(ii) TV Channels: MyTV and Fox
(iii) TV Channels: unknown
(iv) TV Channels: WDTA

The output charge profile of the E-WEHP v4 was measured with a high impedance oscilloscope in the field in midtown Atlanta, which is shown in **Figure 93**. Field measurements show the E-WEHP v4 capable of powering a 1 mega-ohm end-load with between 5µA and 3µA at output voltages of between 1.8 and 3.1V from the -13.92 dBm (40.55 microwatts) of channel power present in CBS and IND TV channels, with an efficiency of 22.1%.

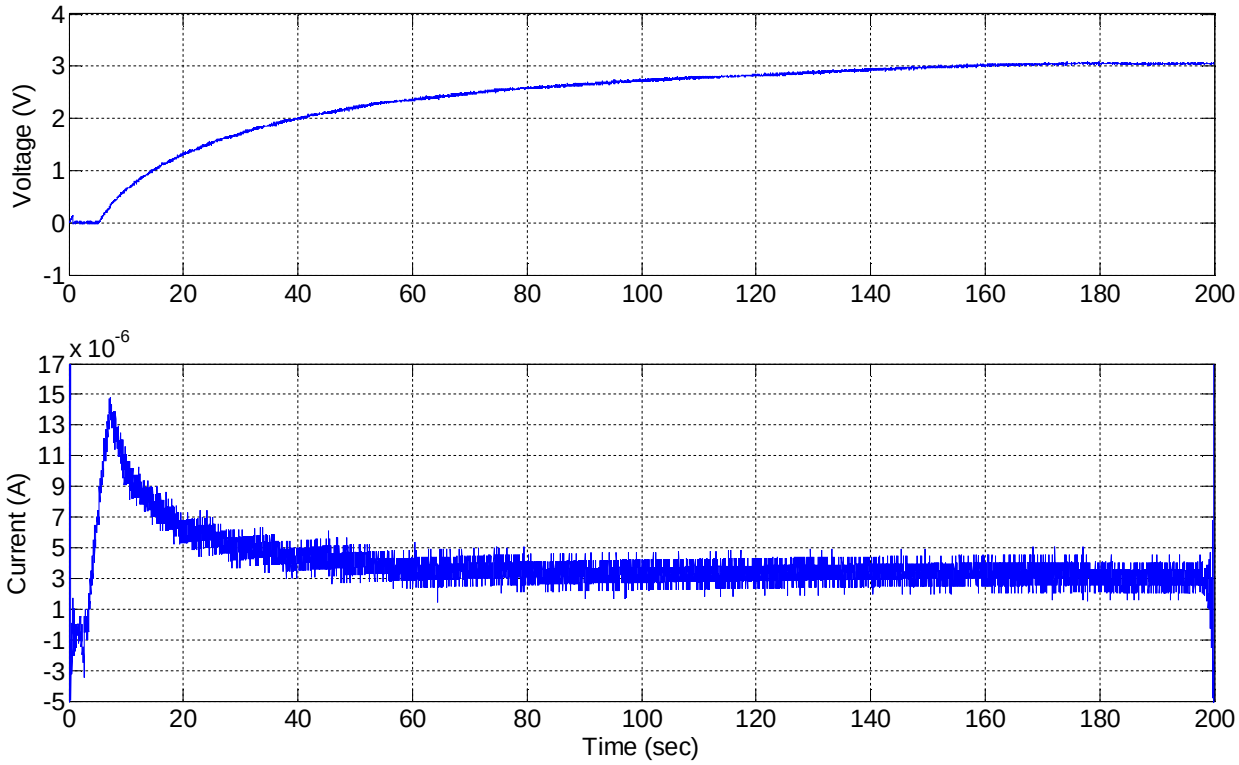

Figure 93. E-WEHP v4 output voltage and current measured in the field after filtering out higher frequency noise ripples introduced by the environment and the E-WEHP v4 RF-DC charge pump circuit.

The E-WEHP v4's output voltage of 3.27V measured in the field was consistently observed to be higher than the 2V measured in lab with the SMJ100A as shown in **Figure 84**. The discrepancy is explained by comparing the actual CBS and IND TV signals measured in the field and the emulated signals generated in the lab as shown in **Figure 94**. Field measurements

carried out in Atlanta with the SBA and log-periodic antenna yield better than expected DC output voltages due to the presence of the pilot carrier, and the presence of an extra TV channel between 512 and 518 MHz as shown in **Figure 94**. Digital TV broadcasts in North America under the ATSC standard use a type of amplitude modulation scheme known as 8-VSB in which each channel uses a pilot carrier, 309 kHz from the left-most edge of each TV channel, for carrier extraction on receiver side [*103*]. During field measurements carried out in Atlanta with the SBA and Log-periodic antenna, the pilot carrier was measured to be 10 dB higher than the other carriers within each channels as shown in **Figure 90** and **Figure 92**. While more carriers does improve the RF-DC output and efficiency, higher carrier levels due to the pilot in the input wireless signals have the effect of lowering the loss across each of its Schottky diodes. The higher pilot carriers result in higher amounts of wireless trickle charge flowing into the RF-DC charge pump, which results in higher output voltage and conversion efficiency thereby helping in harvesting TV signals for power [*101*].

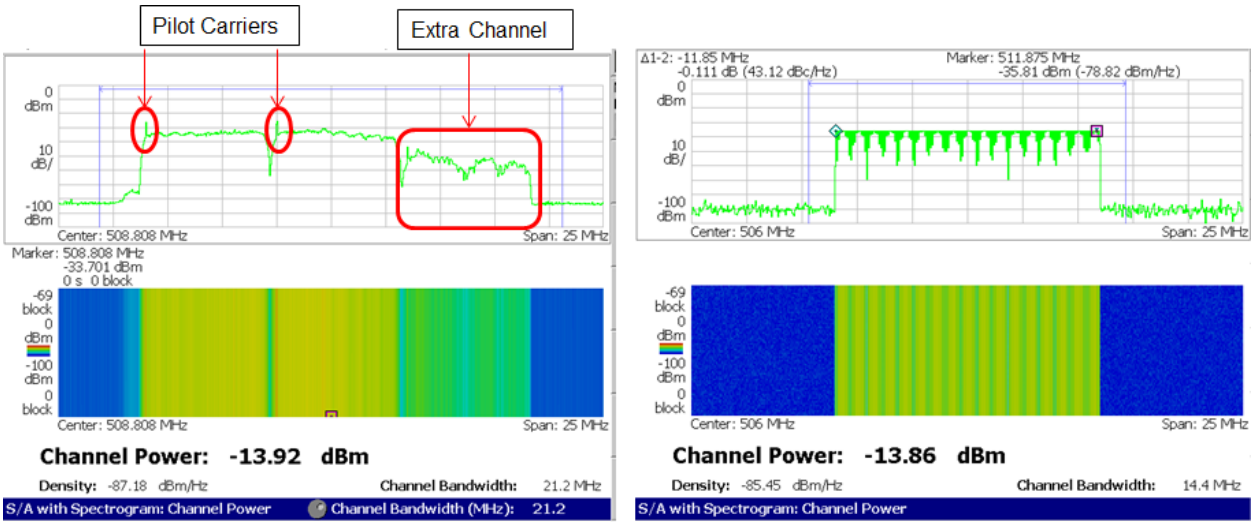

Figure 94. Discrepancy between multi-carrier CBS and IND TV signals measured in the field and emulated using SMJ-100A.

Field measurements in the 500-600 MHz bands using the SBA and Log-periodic antenna also reveal the existence of a 3rd unknown TV channel in the 512-518 MHz band as shown in **Figure 94**. Return loss measurements of the RF-DC in E-WEHP v4 carried out with a VNA show the RF-DC's return loss resonance shift higher than 512 MHz as its output impedance varies with output DC voltages higher than 3V as shown in **Figure 75**. Presence of an extra TV channel between 512 and 518 MHz allows the E-WEHP to continue harvesting power from this band even as its return-loss resonance has shifted higher than 512 MHz, which allows for output DC voltages higher than 3.0V as shown in **Figure 91**.

5.7 Embedded firmware

The primary application envisioned for the E-WEHP is a pervasive way to power on embedded sensors deployed over a large geographic area using ambient, wireless, digital-TV signals present in the air without the help of batteries. The logistical benefit of minimizing or avoiding periodic battery-replacement makes the E-WEHP ideal for applications such as structural health monitoring, monitoring radio-isotope levels in the air, environmental and agricultural sensing etc. In almost every sensing application, embedded microcontrollers play a vital role in sampling, processing, recording and relaying sensed information to the outside world through M2M networks. A comparison of voltage and current ratings of a few well known microcontrollers are shown in **Table 9**. Most embedded microcontrollers require between 1.8V and 3.6V [*104*] [*105*] [*106*] to operate since in that voltage range most CMOS processes offer the optimum combination of low voltage and low leakage current.

Table 9. Microcontroller electrical specifications.

Microcontroller	Clock Speed	Operating Voltage Range	Current
Microchip PIC24F	32 MHz	1.8 - 3.6 V	11 mA
	32 kHz	1.8 - 3.6 V	8-15 µA
	LP Deep Sleep	1.8 - 3.6 V	20-800 nA
TI MSP430	16 MHz	1.8 - 3.6 V	7 mA
	4 kHz	1.8 - 3.6 V	5-6 µA
	LP LPM4	1.8 - 3.6 V	100-150 nA
Silicon Labs SiM3C1XX	80 MHz	1.8 - 3.6 V	33 mA
	16.4 kHz	1.8 - 3.6 V	175-250 µA
	LP P.Mode9	1.8 - 3.6 V	85-650 nA

Newer microcontrollers typically consume in the order of milli-amperes of current at MHz or higher clock speeds and tens of microamperes at lower kHz clock speeds. The latest microcontrollers also offer extreme low power sleep modes (LP) consuming currents in the order of tens to hundreds of nano-amperes with use of limited memory and peripherals [*104*] [*105*] [*106*]. A comparison of the E-WEHP's wireless power supply capabilities from the ambience as shown in **Figure 86**, **Figure 88**, **Figure 89**, **Figure 91** and **Figure 93**, and the microcontroller electrical specifications are shown in **Table 9**. **Table 9** shows that at lower clock speeds in the kHz range or in the Low Power sleep modes, the E-WEHPs v3 and v4 can power up limited embedded applications consuming between 20nA and 8µA while still allowing output voltages of between 1.8 and 4V. While the E-WEHP's current output may not be able to supply milliamperes consumed by embedded operations running at MHz speeds, reserve energy stored up in the charge tank capacitor could be used to power high speed operations for limited duty cycles by using a collect first (Sleep/Charge) use later (Active/Discharge) embedded scheme described earlier. To demonstrate the feasibility of powering on embedded sensor applications from the ambient wireless TV signals, the E-WEHP prototypes connected to a Microchip PIC24F16KA101 microcontroller unit (MCU/PIC24F) were programmed with an energy-aware software-design to sustain itself using just the ambient wireless power present in digital-TV signals without the aid of any batteries and significant power management hardware [*100*] [*101*].

The PIC24F microcontroller includes several 16-bit Analog-to-Digital converter (ADC) modules; a real time clock and calendar module (RTCC); two watch dog timers (WDT); limited sleep memory retention, and several CPU interrupting schemes. These modules were successfully exploited with embedded software to power on and operate the ADC and UART functions on the PIC24F, necessary for sensing functions, for limited duty cycles from just the

power in ambient wireless TV signals captured by the E-WEHP's log-periodic antenna and RF-DC front end circuits. The PIC24F microcontroller unit in the E-WEHP system seen in the prototype in **Figure 71** is configured as per schematic shown in **Figure 95**. The embedded software algorithm successfully used to power and sustain sensing and M2M peripherals in the PIC24F MCU for limited duty cycles from just a 100µF charge tank capacitor, fed with trickle charge from ambient wireless power, is carried out with three different MCU operating modes outlined in subsequent sections [*100*] [*101*].

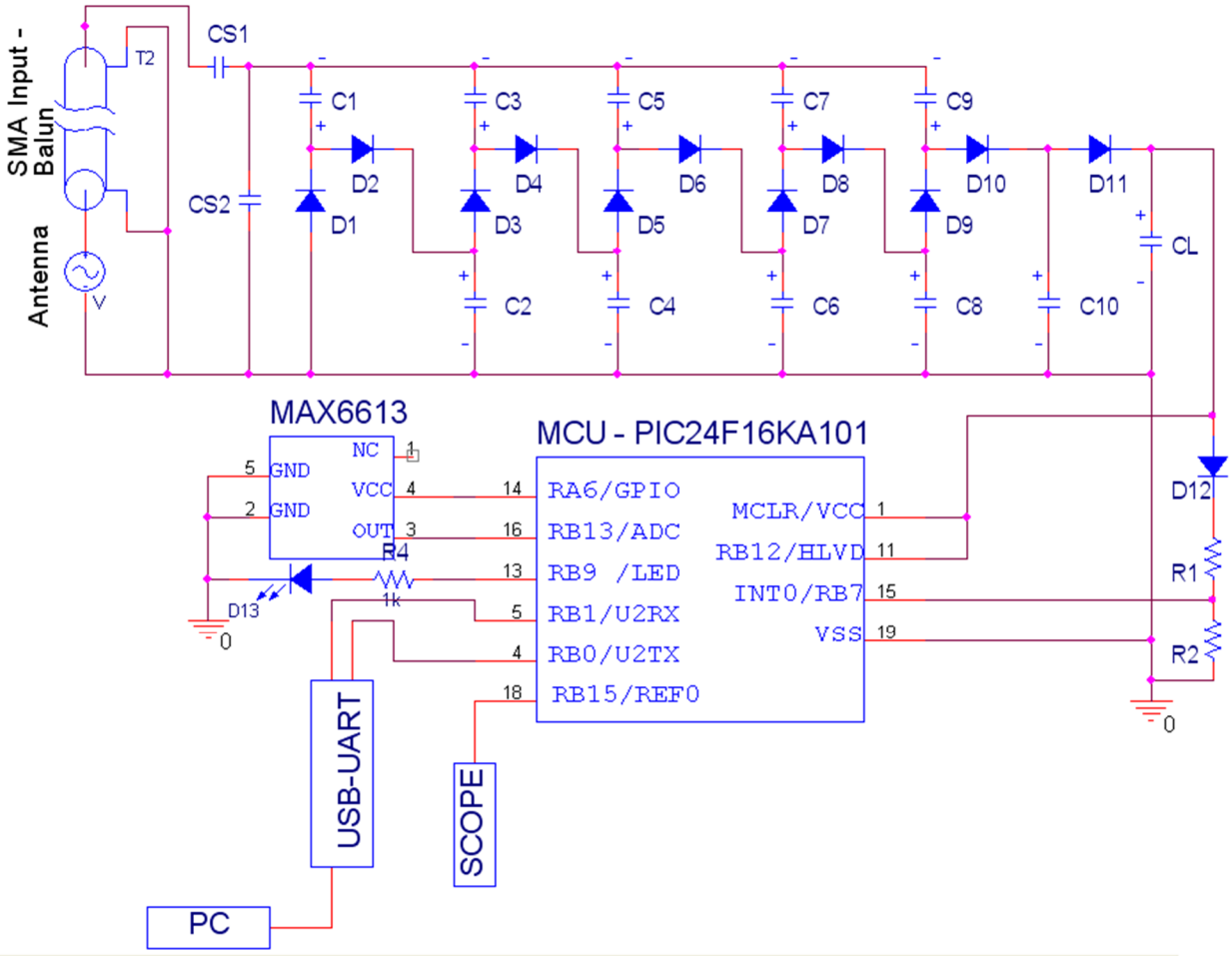

Figure 95. E-WEHP v4 schematic with PIC24F16KA101 Microcontroller connections.

5.7.1 Power-up Mode

During power-up, the digital MOSFET based switches in most processors are neither in an ON nor OFF state, which results in the processor inputs/outputs (I/Os) leaking substantial amounts of the stored capacitor charge. Several options proposed, use a battery to bootstrap the electronics during power-up operation or operate the energy harvesters at close range from the wireless source [*107*] [*108*]. The E-WEHP does not use a battery or extensive power management hardware but instead relies on a software-based approach to power on from the energy stored in the 100µF charge-tank capacitor. While some of the turn-on leakages may be unavoidable, using a faster clock during initial wake-up can cut down this leakage time substantially albeit at the cost of higher current consumption [*101*]. On the PIC24F MCU, using an 8 MHz clock would wake up the CPU in 1-10 microseconds compared to 300 microseconds for a 32 kHz clock [*104*] thereby avoiding deep discharge of the 100 µF charge tank at power-up, which for the MCU occurs at 1.8V. Once the MCU's CPU was up and running using the 8 MHz clock, its I/O pins were programmed as outputs and latched to a high or '1' state to prevent them from siphoning off any charge from the 100 µF charge tank. The GPIO pins that could be configured as analog input/outputs (I/O) were programmed as inputs since they offered the highest input impedance helping arrest the charge-tank leakage further. Starting the MCU with a slower 32 kHz clock causes all the incoming wireless power to be wasted through the PIC24F's I/Os toggling the CPU between a never-ending on and off state as shown in **Figure 96**. Once I/O leakages were plugged, the MCU was programmed to slow down its CPU clock speed from 8 MHz to a lower 32 kHz clock using software to minimize current consumption from 2.25mA to 8µA hence slowing down current discharge during power on [*101*]. Next, the external interrupt and RTCC module in the MCU were configured for charge tank voltage supervision and time

stamping of any sensed data. All of the remaining modules of the MCU were turned off in software, and the MCU was then programmed to put itself into an ultra-low power Sleep/Charge state to allow the charge tank to replenish itself for the losses incurred during initial power-up as shown by stage 'a' in **Figure 97**. The test shown in **Figure 97** was carried out using the E-WEHP v3 with a PIC24F MCU connected at its output interface as shown in **Figure 95**, and feeding the E-WEHP v3 with an input wireless channel power of -8.99 dBm that was observed in downtown Tokyo at a distance of 6.5 km from Tokyo TV tower.

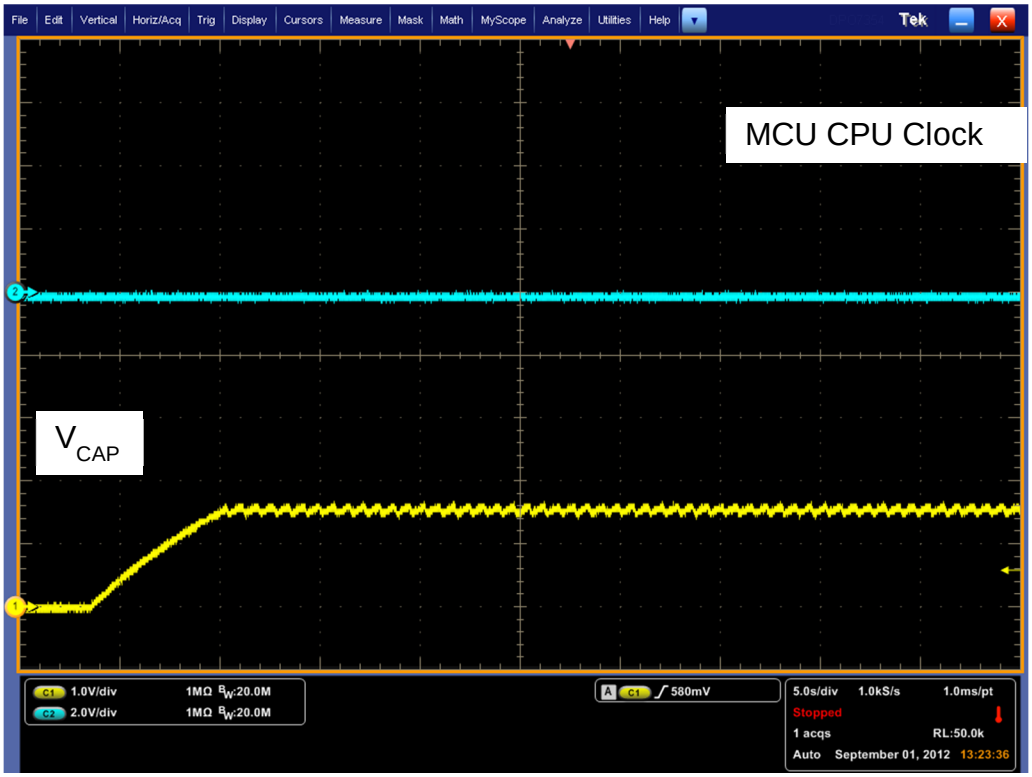

Figure 96. E-WEHP power-up using a 32 kHz CPU clock.

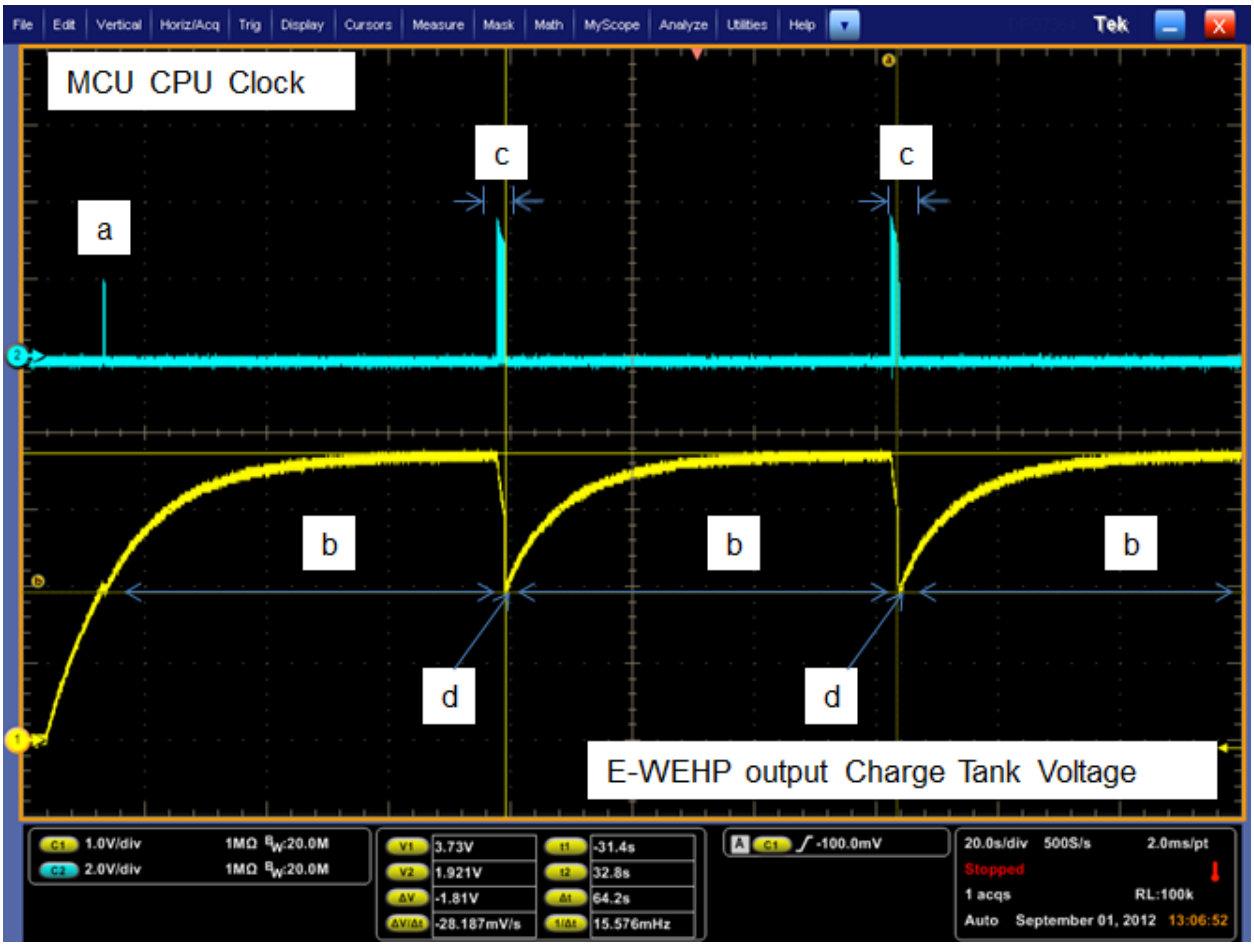

Figure 97. Self-sustaining E-WEHP embedded MCU operation powered with Input wireless channel power of -8.99dBm present in wireless TV signals in Tokyo.
(a) Power up Mode. CPU Clock=8 MHz
(b) Charge/Sleep Mode. RTCC On, CLK=32 kHz, 60 sec wakeup interval
(c) Active/Discharge Mode: 2sec duty cycle, RTCC,ADC, UART, LED, Ext INT On, CLK=32 kHz
(d) Transition from Active to Charge Mode triggered by external interrupt at Charge tank voltage of 1.9V.

5.7.2 Sleep/Charge Mode

Most sensing applications require the sensor to be sampled only at intervals of seconds to hours or longer depending on the sensing application. Between sensor readings, the interrogating microcontroller can be turned off or put in a hibernating state to conserve power. The PIC24F MCU in E-WEHP was programmed to go into a deep-sleep mode after power-up and in between sensor interrogations with its real-time-clock-calendar (RTCC) and external-interrupt module enabled. The RTCC allows the capability to time stamp any sensor reading while still consuming currents of between 490 and 800 nA, which along with the leakage through the oscilloscope probe leakage consumes a total of around 4.5µA, which still allows the E-WEHP v3's charge tank capacitor to charge up to around 3.75V from the ambient wireless power present in the field in Tokyo as per the E-WEHP v3's charge profile shown in **Figure 88** and **Figure 97**. The charge tank charge profile during Sleep/Charge mode is shown by stage 'b' in **Figure 97**. During field measurements, E-WEHPs v3 and v4 requires between 60 and 160 seconds to refill its charge tank from 1.8V to 3.75V and 3.2 V using the power in TV signals at 6.5 to 6.0 km from the TV broadcast sources in Tokyo and Atlanta, respectively. The PIC24F MCU is therefore programmed to wake itself up from deep sleep mode at chimed intervals of every 60 second after entering deep sleep mode using the RTCC clock at which point the MCU firmware was programmed to activate itself or any attached sensor to get into the active mode. The wake-up interval of the MCU from deep-sleep mode can be self-adjusted using embedded software based on the time for charge-build up across the charge tank, which would vary depending on the position of the E-WEHP within the TV broadcast network.

5.7.3 Active/Discharge Mode

In active mode, the MCU is programmed to turn on the CPU in order to activate its peripherals, namely the ADC and Universal asynchronous receive and transmit modules (UART) to carry out most kinds of analog sensor sampling and M2M communication with an interrogating PC, reader or low power radio for debugging or telemetry purposes. ADCs and UART modules in the PIC24F consume roughly between 4μA and 11mA each, larger than the current flow generated from the ambience by the E-WEHP in the field 6.0-6.5 km from the broadcast source as shown in **Figure 88** and **Figure 93**. This causes the E-WEHP's charge tank capacitor to supply the excess current from its charge stored in the previous sleep/charge mode cycle, and in the process discharging itself.

To determine the optimum operating speed of the PIC24F MCU in the Active/Discharge mode, the minimum operating voltage and current required to run the PIC24F MCU at difference clock speeds is shown in **Figure 98**. For battery-powered, limited duty-cycle operations, running the embedded operation at higher CPU clock speeds consumes more current but allows implementation of many more cycles within a shorter time, which lowers the average current consumption over the operating lifetime. However, CPUs running at higher clock speeds also require a higher DC supply voltage, which reduces the operating duty cycle of embedded operations powered from a discharging charge tank capacitor as in the E-WEHP. At maximum clock speeds of 8 and 32 MHz, the PIC24F MCU requires at least 3V DC, and consumes between 3 and 11 mA of current. However, at clock speeds of 32 kHz the PIC24F can run of only 1.8V of DC supply consuming only between 4 and 12 microamperes of current as shown in **Figure 98**.

The number of operating cycles or instructions that can be run on the PIC24F MCU, which is powered from a charge tank capacitor fed by wireless trickle charge in the Active/Discharge mode is a function of the wireless energy harvested in the Sleep/Charge mode and the PIC24F MCU's operating voltage and current, which is dependent on the MCU's clock speed ('f_{CLK}') as determined by (31). The energy harvested in Sleep/Charge mode that gets used in the Active/Discharge mode is a function of the charge tank capacitance (C_L), the RF-DC output voltage ($V_{RF\text{-}DC}$), the PIC24F's minimum operating voltage ($V_{MCU\text{-}OFF}$) and current (I_{MCU}) as plotted in **Figure 98**. The number of MCU operating instructions that the E-WEHP can run of the power in using wireless digital TV signals in Atlanta at different clock speeds determined using (31) is plotted in **Figure 99**. Based on E-WEHP v4's RF-DC power output in the field in Midtown Atlanta and PIC24F MCU's power consumption, between 38,000 and 211,000 instructions can be implemented between clock speeds of 32 MHz and 32 kHz, respectively. Based on the above analysis, the optimum clock speed at which maximum number of MCU instructions can be implemented using the ambient wireless power rectified by E-WEHP during the Active/Discharge mode is between 32 kHz and 1 MHz.

$$\#Operating\ Cycles = -\frac{1}{4} \cdot \ln\left(\frac{V_{MCU-OFF}}{V_{RF-DC}}\right) \cdot \frac{V_{MCU-OFF} + V_{RF-DC}}{I_{MCU}} \cdot C_L \cdot f_{CLK} \quad (31)$$

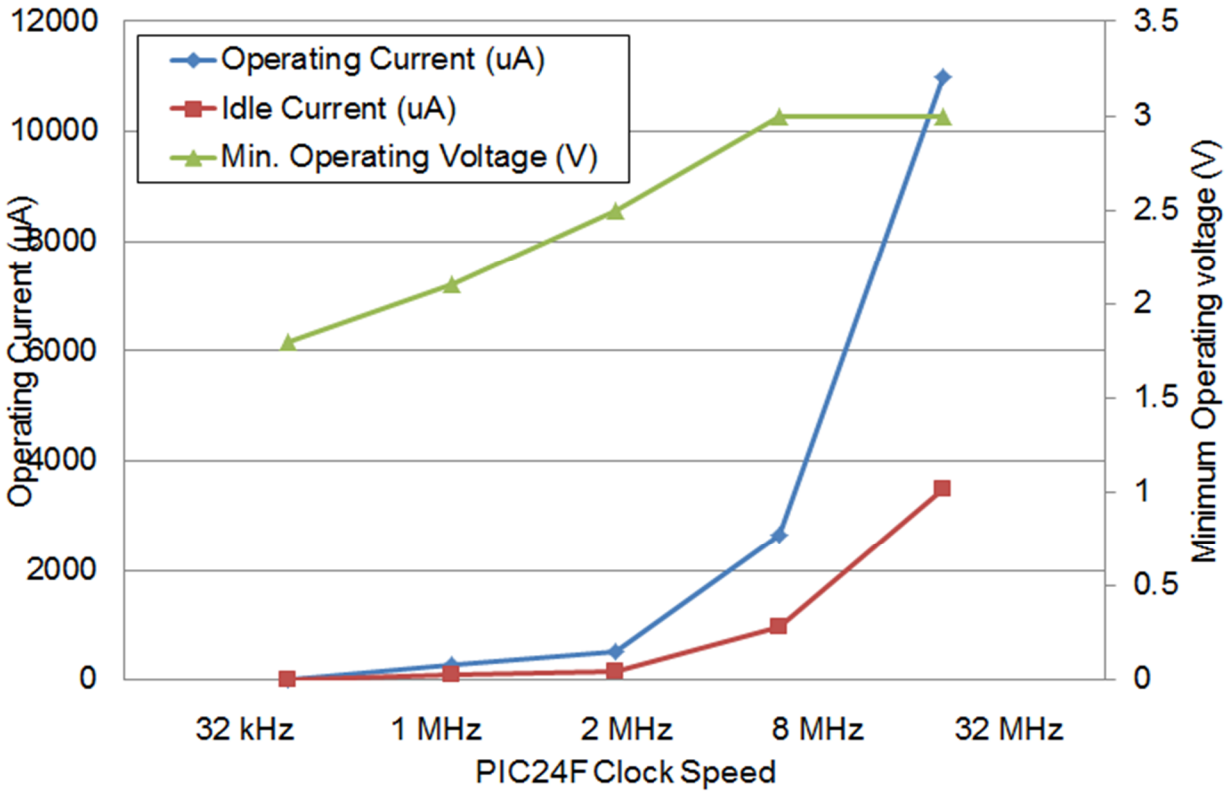

Figure 98. Minimum operating voltage and operating current of the PIC24F at different CPU clocks speeds.

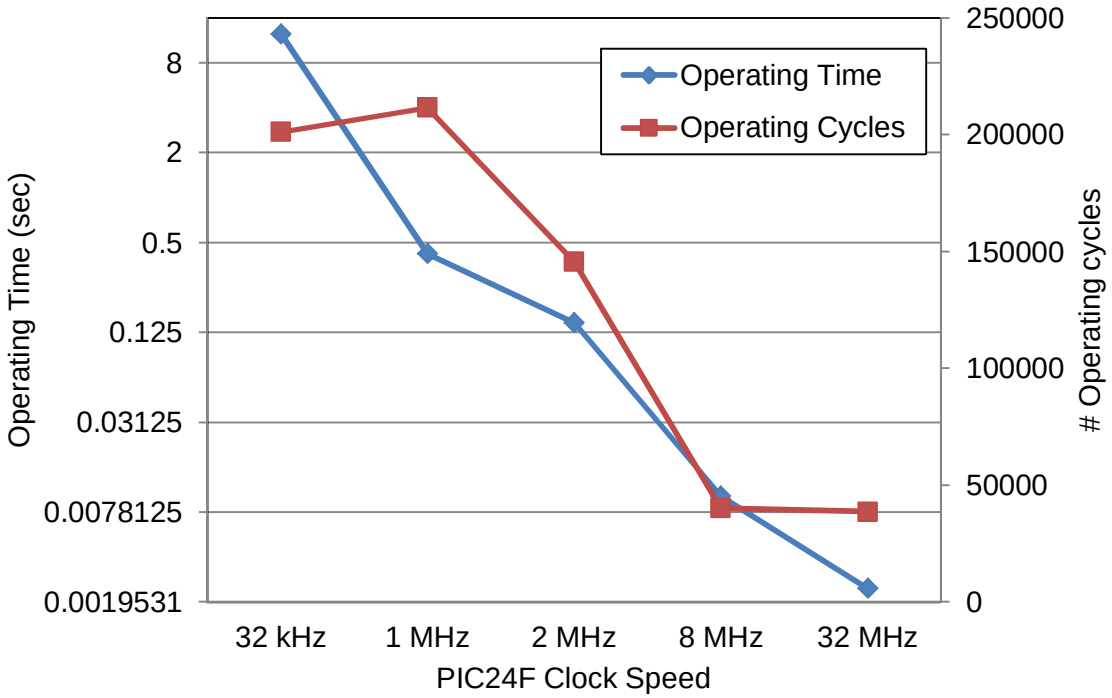

Figure 99. PIC24F operating time and cycles for different CPU clock speeds.

Once the MCU has been powered-up and in active mode, its firmware with very minimal hardware is used to prevent deep discharge of the charge-tank capacitor to below 1.8V where the PIC24F MCU gets latched into a never ending reset state similar to the state in **Figure 96**. Deep discharge of the charge tank is arrested through the use of resistors R1 and R2, diode D12 and the MCU's external interrupt module programmed at its INT0/RB7 input pin as shown in the schematic in **Figure 95**. Forty mega-ohm resistors were used for 'R1' and 'R2', which in parallel with the input impedance of the MCU's external interrupt input pin 'INT0/RB7', produces a voltage of 1.8V at the input pin when the charge tank capacitor discharges to 1.9V. A high to low transition at the INT0/RB7 input was programmed to interrupt the MCU's CPU from any ongoing active operation, power down the peripherals and I/Os, and put the MCU back into Sleep/Charge mode with only the RTCC module on as shown by stage 'd' in **Figure 97**. A Diode

'D12' with a high forward voltage is used to delay leakage of charge tank current through the resistors during its initial charge up. The current consumed by the interrupt scheme is 82.5 nA, which is much lower than 10s of microamperes consumed by power management ICs during initial charge-up. Embedded operations, including any external sensing function, can be carried out in the amount of time taken by E-WEHP's 100 µF charge tank to discharge from its maximum output voltage, which in the field is around 3.26 - 3.7V, down to 1.9V in the Active/Discharge mode as shown by stage 'c' in **Figure 97**. At this point the external interrupt is triggered putting CPU back in Sleep/Charge mode.

The operating time of the MCU in the Active/Discharge mode ('T_{ACTIVE}') is also a function of the amount of energy harvested and stored in charge tank during the Sleep/Charge mode, and the PIC24F MCU's voltage and current consumption as shown by the relationship in (32) [*109*].

$$T_{ACTIVE} = -\ln\left(\frac{V_{MCU-OFF}}{V_{RF-DC}}\right) \cdot \frac{V_{MCU-OFF} + V_{RF-DC}}{2 \cdot I_{MCU}} \cdot C_L \tag{32}$$

Based on the E-WEHP's RF-DC performance in the field in Atlanta and Tokyo covered in the preceding section and the PIC24F MCU's DC characteristics, the MCU's operating time in the Active/Discharge in the field is expected to be less than 12.57 sec and over 2.4 milliseconds depending on clock speed and number of peripherals operating in parallel as shown in **Figure 99**. The energy aware E-WEHP firmware was tested in the field in Midtown Atlanta by orienting the prototype in the direction of two known TV broadcast towers about 6.0 km away as shown in **Figure 100**. In this orientation, the E-WEHP v4 prototype generates 3.26V output primarily from

two TV channels, CBS and IND as shown in **Figure 91**. The E-WEHP v4 MCU's charge tank and CPU clock operation during field measurements in Atlanta are shown in **Figure 100** and **Figure 101**, and show E-WEHP's PIC24F MCU able to sustain itself perpetually from just the power present in ambient TV signals at 6.0km from the CBS and IND TV broadcast towers. The E-WEHP v4 could well-run UART and ADC operations along with blinking an LED for close to 1 sec run time in Active/Discharge mode at wake-up intervals of 10 sec in Sleep/Charge mode. This field test demonstrates the feasibility of running embedded sensor and M2M functions without batteries, and by using just the ambient wireless TV signals at terrestrial distances of over 6.0 km.

Figure 100. Self-sustaining E-WEHP embedded operation powered from power in wireless CBS and IND TV signals with combined channel power of -13.92dBm in Midtown Atlanta.

Figure 101. Self-sustaining E-WEHP v4 Microcontroller operation powered from ambient CBS and IND wireless TV signals in Midtown Atlanta.

Embedded operations carried out by the E-WEHP v4 in **Figure 100** and **Figure 101** include a real-time-clock-calendar module for time stamping sensor readings and external interrupt module that are operational in both Active/Discharge and Sleep/Charge modes. During the active/discharge mode, the E-WEHP also runs its 10-bit ADC module, a universal asynchronous receiver and transmitter (UART) and a SMT LED for durations of 1 sec at 10 second intervals for sampling and relaying any type of analog sensor senor information to the

end user. Serial UART communication by the E-WEHP was carried out at a baud rate of 300 bits per second using an MCU clock rate of 32 kHz with which fewer bit errors were observed during serial communication between E-WEHP and a Windows PC. Serial communication from the E-WEHP powered from ambient wireless TV signals was tested by orienting the E-WEHP towards the CBS and IND TV towers as shown in **Figure 91**, and reading the E-WEHP v4 PIC24F MCU's UART I/O pins RB0 and RB1 on a Real Term terminal program on a Windows PC through a Serial-to-USB adapter. The E-WEHP transmitted serial data captured on the Real-term terminal program on the Windows PC in the field in Atlanta is shown in **Figure 102**, and shows the E-WEHP relaying a pre-programmed time and date-stamped message "Gan=Hello GT" at regular intervals of 10 seconds using just the power harvested by its Log-periodic antenna and RF-DC charge pump circuit without the aid of batteries. The letters "RRRRM" denote flags that are used to denote a chime event by the RTCC module that is used to wake-up the E-WEHP from the deep Sleep/Charge mode in **Figure 102**. The periodic transition of the charge tank voltage from discharge to charge mode upon reaching 1.9V denoted by 'd' in **Figure 101** shows the proper functioning of the PIC24F MCU's external interrupt module in making the E-WEHP self-aware of its power consumption with respect to the wireless power coming in from the ambience.

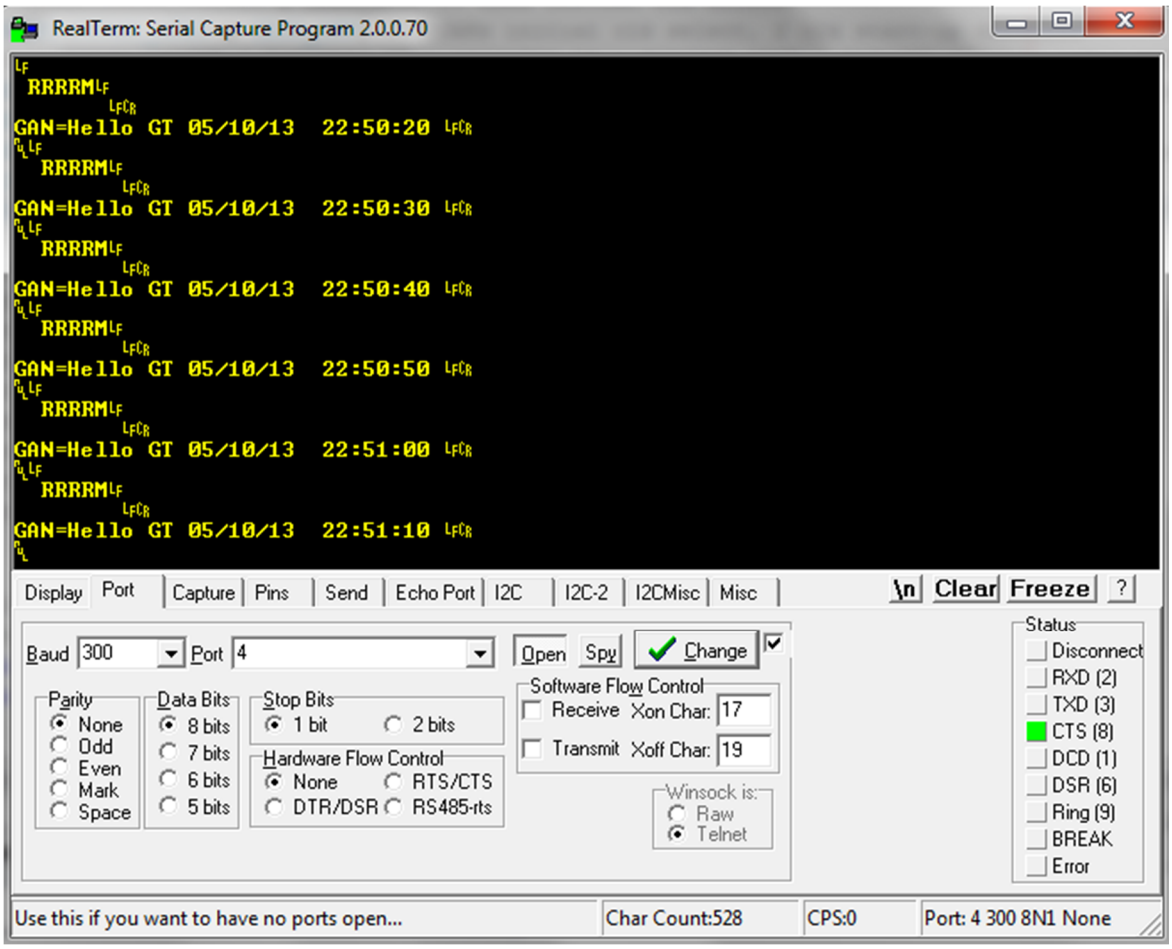

Figure 102. Self-sustaining UART communication between E-WEHP v4 and Windows PC powered from ambient CBS and IND Wireless TV signals in Midtown Atlanta.

A comparison of the E-WEHPs power harvesting capability with respect to other wireless energy harvesting systems is shown in **Table 10** below. Most of the wireless power harvesting work in the far-field has been in the UHF bands between 862 and 928 MHz for RFID-based sensors as shown in **Table 10**. Most of the new designs use sub-micron CMOS technology with RF input sensitivities down in the tens of microwatts with reported range of 9.25 meters. Most of the RFID-based, wireless power-harvesting designs are optimized for high sensitivities at a

single tone within the RFID operating bands between 862 and 928 MHz. This is primarily because RFIDs operate only within range of a conventional RFID reader that emits between 2 and 4W EIRP using a frequency hopping spread spectrum (FHSS) for power and communication. However by targeting the multi-carrier make-up of ambient digital TV signals, much longer range of wireless power harvesting is possible as demonstrated by the E-WEHP prototypes.

Table 10. Wireless Energy harvesting comparisons.

Project	RF Sensitivity/ DC output	RF Source	Load	Range/ Rx Antenna Gain	Process
Karalis [*29*]	NA	9.9 MHz, 60W near-field	Light bulb	2m	Coil
NXP UCode [*110*]	-12.6dBm single tone	RFID reader: 4W EIRP, 900MHz	Control logic, SRAM	-	CMOS
Karthaus [*94*]	-17.8dBm @ 1.5V, 1.5µA single tone	RFID reader: 4W EIRP, 900MHz	Control Logic, EEPROM	9.25m, -0.5dBi	0.5 µm CMOS
Reinisch [*111*]	-19.7dBm @ 1.1V, 158nA single tone	RFID reader: 4W EIRP, 900MHz	Temp sensor, Tx	-	0.13 µm CMOS
Yin [*112*]	-6dBm @ 1V, 2.4µW single tone	RFID reader: 4W EIRP, 900MHz	Temp Sensor	-	0.18 µm CMOS
Yeager [*113*]	-12 dBm @ 9µA	RFID reader: 4W, 900MHz	Temp Sensor	3m	0.13 µm CMOS & PCB
Power Cast P2110 [*37*]	-11.5dBm @ 1.2V	Transmitter 915 MHz	Battery	8m, 6dBi	CMOS
Dolgov [*107*]	-15.2 dBm @ 3V with battery-assisted MPPT	Ambient Cellular 1.96 GHz	Battery	50m	PCB
WISP [*34*]	-9.5dBm @1.9V, 0.7µA	RFID reader: 4W, 900MHz	TI MSP 430F1232 MCU	Theoretical 4.3m, 2dBi	PCB
WISP [*108*]	NA @ 0.7V, 87.5 µA	Ambient TV Signal 960kW ERP	Temp Sensor	4.1km, 5dBi	PCB
E-WEHP v3 [*101*]	-14.6dBm Single tone or -37dBm multi-tone over 2 TV channels @ 1.8V, 1.8 µA	Ambient Digital TV 512-566 MHz, 48kW ERP	16-bit PIC MCU	6.3km, 7.3 dBi	PCB
E-WEHP v4 [*100*]	-18.86dBm Single Tone @1.8V, 1.8 µA	Ambient Digital TV 512-566 MHz, 48kW ERP	16-bit PIC MCU	5.6km, 7.3 dBi	PCB

CHAPTER 6. CONTRIBUTIONS AND PUBLICATIONS

This work has proved the feasibility of using the orthogonal-frequency-division-multiplexed nature (OFDM) of wireless digital-TV signals as a pervasive power source to sustain embedded sensors without batteries over a range of 6.5 km. Demonstrating this feasibility involved development of novel, planar, wideband antenna-structures for transducing wireless radiation due to TV broadcasts into electrical RF signals along with new understanding of rectification properties of the transduced multi-carrier/tone and a multi-channel modern wireless digital TV signals using ISDB-T and ATSC standards. In addition, this work also includes the design and development of the first of its type inkjet-printed wireless sensors on a biodegradable substrate, and the first solar-powered RFID tag for a GPS-like localization application.

There have been many contributions both to the academic and commercial communities, mostly in helping better understand advantages and challenges brought by this technology. Perhaps the most substantial of these contributions are the following:

• The first inkjet-printed wireless sensor modules on paper-based substrate

- Acknowledged by *IEEE International Microwave Symposium 2008*

"Student Paper Finalist"

- Acknowledged by *IEEE International Symposium on Antennas and Propagation 2008*

"Honorable mention Award"

• The first solar-powered wireless tag for vehicle tracking and localization

- Acknowledged by *IEEE International Symposium on Antennas and Propagation 2009*

"Honorable mention Award"

• The longest-range wireless power harvesting prototypes exploiting OFDM-based wireless digital TV signals

- Acknowledged by *IEEE International Microwave Symposium 2012*

"Student Paper Finalist"

- Acknowledged by *Engadget, Gizmag, IEEE Institute, MSN News, Discovery, Times of India, New Energy and Fuel etc.*

This work and other related research carried out as a Ph.D. student and candidate has led to publications listed in the following section:

AUTHOR'S PUBLICATIONS

Journals

1. L. Yang, A. Rida, R. Vyas, M. Tentzeris, "RFID Tag and RF Structures on a Paper Substrate Using Inkjet-Printing Technology," *Microwave Theory and Techniques, IEEE Transactions on* , vol.55, no.12, pp.2894-2901, Dec. 2007.

2. R. Vyas, V. Lakafosis, A. Rida, N. Chaisilwattana, S. Travis, J. Pan, M. Tentzeris, "Paper-Based RFID-Enabled Wireless Platforms for Sensing Applications," *Microwave Theory and Techniques, IEEE Transactions on* , vol.57, no.5, pp.1370-1382, May 2009.

3. A. Rida, L. Yang, R. Vyas, M. Tentzeris, "Conductive Inkjet-Printed Antennas on Flexible Low-Cost Paper-Based Substrates for RFID and WSN Applications," *Antennas and Propagation Magazine, IEEE* , vol.51, no.3, pp.13-23, June 2009.

4. V. Lakafosis, A. Rida, R. Vyas, L. Yang, S. Nikolaou, M. Tentzeris, "Progress Towards the First Wireless Sensor Networks Consisting of Inkjet-Printed, Paper-Based RFID-Enabled Sensor Tags," *Proceedings of the IEEE* , vol.98, no.9, pp.1601-1609, Sept. 2010.

5. R. Vyas, V. Lakafosis, H. Lee, G.Shaker, L. Yang, G. Orecchini, A. Traille, M. Tentzeris, L. Roselli, "Inkjet Printed, Self Powered, Wireless Sensors for Environmental, Gas, and Authentication-Based Sensing," *Sensors Journal, IEEE* , vol.11, no.12, pp.3139-3152, Dec. 2011.

6. M. Tentzeris, R.Vyas, V.Lakafosis, T.Le, A.Rida, S.Kim, "Conformal 2D/3D Wireless Modules Utilizing Inkjet Printing and Nanotechnology." *Microwave Journal Magazine* 14 Feb. 2012. http://www.microwavejournal.com/articles/print/16914

7. Cook, B.; **Vyas, R.**; Kim, S.; Thai, T.; Le, T.; Traille, A.; Aubert, H.; Tentzeris, M., "RFID-Based Sensors for "Zero-Power" Autonomous Wireless Sensor Networks," *Sensors Journal, IEEE* , vol.PP, no.99, pp.1,1

8. Sangkil Kim; Cook, B.; Taoran Le; Cooper, J.; Hoseon Lee; Lakafosis, V.; **Vyas, R**.; Moro, R.; Bozzi, M.; Georgiadis, A.; Collado, A.; Tentzeris, M.M., "Inkjet-printed antennas, sensors and circuits on paper substrate," *Microwaves, Antennas & Propagation, IET* , vol.7, no.10, pp.858,868, July 16 2013

9. Shigeta, R.; Sasaki, T.; Duong Minh Quan; Kawahara, Y.; **Vyas, R.J.**; Tentzeris, M.M.; Asami, T., "Ambient RF Energy Harvesting Sensor Device With Capacitor-Leakage-Aware Duty Cycle Control," *Sensors Journal, IEEE* , vol.13, no.8, pp.2973,2983, Aug. 2013

Book Chapter

1. V. Lakafosis, R. Vyas and M. M. Tentzeris, “Localization Techniques in single and multi-hop wireless networks”, invited chapter in *Handbook of Smart Antennas for RFID Systems*, edited by N. C. Karmakar, Wiley-Interscience, 2010, ISBN-10: 0470387645

2. M. Tentzeris, **R.Vyas** et al. “Novel Antenna and Sensing Structures and Complete Wireless Modules for Biomedical Applications”, *Wiley IEEE Handbook of Biomedical Telemetry*, 2013.

Conferences

1. R. Vyas, A. Rida, S. Bhattacharya, M. Tentzeris, "Liquid Crystal Polymer (LCP): The ultimate solution for low-cost RF flexible electronics and antennas," *Antennas and Propagation Society International Symposium, 2007 IEEE* , vol., no., pp.1729-1732, 9-15 June2007.

2. A. Rida, R. Vyas, S. Basat, A. Ferrer-Vidal, L. Yang, S. Bhattacharya, M. Tentzeris, "Paper-Based Ultra-Low-Cost Integrated RFID Tags for Sensing and Tracking Applications," *Electronic Components and Technology Conference, 2007. ECTC '07. Proceedings. 57th* , vol., no., pp.1977-1980, May 29 2007-June 1 2007.

3. M. Tentzeris, L. Yang, A. Rida, A. Traille, R. Vyas, T. Wu, "RFID's on Paper using Inkjet-Printing Technology: Is it the first step for UHF Ubiquitous "Cognitive Intelligence" and "Global Tracking"?," *RFID Eurasia, 2007 1st Annual* , vol., no., pp.1-4, 5-6 Sept. 2007.

4. R. Vyas, A. Rida, L. Yang, M. Tentzeris, "Design and Development of a Novel Paper-based Inkjet-Printed RFID-Enabled UHF (433.9 MHz) Sensor Node," *Microwave Conference, 2007. APMC 2007. Asia-Pacific*, vol., no., pp.1-4, 11-14 Dec. 2007.

5. A. Rida, L. Yang, R. Vyas, S. Basat, S. Bhattacharya, M. Tentzeris, "Novel Manufacturing Processes for Ultra-Low-Cost Paper-Based RFID Tags with Enhanced "Wireless Intelligence"," *Electronic Components and Technology Conference, 2007. ECTC '07. Proceedings. 57th* , vol., no., pp.773-776, May 29 2007-June 1 2007.

6. M. Tentzeris, L. Yang, A. Rida, A. Traille, R. Vyas, T. Wu, "Inkjet-Printed RFID Tags on Paper-based Substrates for UHF "Cognitive Intelligence" Applications," *Personal, Indoor and Mobile Radio Communications, 2007. PIMRC 2007. IEEE 18th International Symposium on*, vol., no., pp.1-4, 3-7 Sept. 2007.

7. A. Rida, R. Vyas, T. Wu, R. Li, M. Tentzeris, "Development and Implementation of Novel UHF Paper-Based RFID Designs for Anti-counterfeiting and Security Applications," *Anti-counterfeiting, Security, Identification, 2007 IEEE International Workshop on* , vol., no., pp.52-56, 16-18 April 2007.

8. A. Rida, L. Yang, R. Vyas, S. Bhattacharya, M. Tentzeris, "Design and integration of inkjet-printed paper-based UHF components for RFID and ubiquitous sensing applications," *Microwave Conference, 2007. European* , vol., no., pp.724-727, 9-12 Oct. 2007.

9. A. Rida, R. Vyas, L. Yang, C. Kruesi, M. Tentzeris, "Low Cost Inkjet-printing Paper-Based Modules for RFID Sensing and Wireless Applications," *Microwave Conference, 2008. EuMC 2008. 38th European* , vol., no., pp.1715-1718, 27-31 Oct. 2008.

10. A. Rida, R. Vyas, L. Yang, C. Kruesi, M. Tentzeris, "Low cost inkjet-printing paper-based modules for RFID sensing and wireless applications," *Wireless Technology, 2008. EuWiT 2008. European Conference on* , vol., no., pp.294-297, 27-28 Oct. 2008.

11. L. Yang, R. Vyas, A. Rida, J. Pan, M. Tentzeris, "Wearable RFID-enabled sensor nodes for biomedical applications," *Electronic Components and Technology Conference, 2008. ECTC 2008. 58th* , vol., no., pp.2156-2159, 27-30 May 2008.

12. R. Vyas, V. Lakafosis, Z. Konstas, M. Tentzeris, "Design and characterization of a novel battery-less, solar powered wireless tag for enhanced-range remote tracking applications," *Microwave Conference, 2009. EuMC 2009. European* , vol., no., pp.169-172, Sept. 29 2009-Oct. 1 2009.

13. M. Tentzeris, A. Traille, L. Yang, V. Lakafossis, R. Vyas, A. Rida, A. Haque, D. Staiculescu, "RFID-enabled biosensing wireless modules," *Radio and Wireless Symposium, 2009. RWS '09. IEEE* , vol., no., pp.131-134, 18-22 Jan. 2009.

14. R. Vyas, V. Lakafosis, T. Wu, Y. Kawahara, M. Tentzeris, "Near-perpetual operated solar and RF powered autonomous sensing systems," *Microwave Conference, 2009. APMC 2009. Asia Pacific* , vol., no., pp.2240-2243, 7-10 Dec. 2009.

15. Z. Konstas, A. Rida, R. Vyas, K. Katsibas, N. Uzunoglu, M. Tentzeris, "A novel “Green” inkjet-printed Z-shaped monopole antenna for RFID applications," *Antennas and Propagation, 2009. EuCAP 2009. 3rd European Conference on* , vol., no., pp.2340-2343, 23-27 March 2009.

16. M. Tentzeris, A. Traille, H. Lee, A. Rida, V. Lakafosis, R. Vyas, "Inkjet-printed paper/polymer-based “green” RFID and Wireless Sensor Nodes: The final step to bridge cognitive intelligence, nanotechnology and RF?," *Microwave Conference Proceedings (APMC), 2010 Asia-Pacific* , vol., no., pp.291-294, 7-10 Dec. 2010.

17. M. Tentzeris, R. Vyas, V. Lakafosis, A. Traille, A. Rida, G. Shaker, "Inkjet-printed system-on-paper/polymer “green” RFID and wireless sensors," *Electronic Components and Technology Conference (ECTC), 2010 Proceedings 60th* , vol., no., pp.1552-1555, 1-4 June 2010.

18. M. Tentzeris, A. Traille, H. Lee, A. Rida, V. Lakafosis, R. Vyas, "Inkjet-printed paper/polymer-based “green” RFID and Wireless Sensor Nodes: The final step to bridge cognitive intelligence nanotechnology and RF?," *Sensors, 2010 IEEE* , vol., no., pp.1273-1276, 1-4Nov. 2010.

19. R. Vyas, V. Lakafosis, M. Tentzeris, "Enabling Localization in WSNs with Solar-Powered End Devices," *Sensor Networks, Ubiquitous, and Trustworthy Computing (SUTC), 2010 IEEE International Conference on* , vol., no., pp.155-160, 7-9 June 2010.

20. R. Vyas, V. Lakafosis, M. Tentzeris, "Wireless remote localization system utilizing ambient RF/solar power scavenging RFID tags," *Microwave Symposium Digest (MTT), 2010 IEEE MTT-S International* , vol., no., pp.1764-1767, 23-28 May 2010.

21. R. Vyas, V. Lakafosis, M. Tentzeris, H. Nishimoto, Y. Kawahara, "A battery-less, wireless mote for scavenging wireless power at UHF (470–570 MHz) frequencies," *Antennas and Propagation (APSURSI), 2011 IEEE International Symposium on* , vol., no., pp.1069-1072, 3-8 July 2011.

22. M. Tentzeris, A. Rida, A. Traille, H. Lee, V. Lakafosis, R. Vyas, "Inkjet-printed paper/polymer-based RFID and Wireless Sensor Nodes: The final step to bridge cognitive intelligence, nanotechnology and RF?," *General Assembly and Scientific Symposium, 2011 XXXth URSI* , vol., no., pp.1-4, 13-20 Aug. 2011.

23. A. Rida, V. Lakafosis, R. Vyas, M. Tentzeris, S. Nikolaou, "Review of technologies for low-cost integrated sensors," *RFID-Technologies and Applications (RFID-TA), 2011 IEEE International Conference on* , vol., no., pp.513-520, 15-16 Sept. 2011.

24. X. Yi, C. Cho, C. Fang, J. Cooper, V. Lakafosis, R. Vyas, Y. Wang, R. Leon, M. Tentzeris, "Wireless strain and crack sensing using a folded patch antenna," *Antennas and Propagation (EUCAP), 2012 6th European Conference on* , vol., no., pp.1678-1681, 26-30 March 2012.

25. F. Giuppi, A. Georgiadis, S. Via, A. Collado, R. Vyas, M. Tentzeris, M. Bozzi, "A 927 MHz solar powered active antenna oscillator beacon signal generator," *Wireless Sensors and Sensor Networks (WiSNet), 2012 IEEE Topical Conference on* , vol., no., pp.1-4, 15-18 Jan. 2012.

26. X. Yi, R. Vyas, C. Cho, C. Fang, J. Cooper, Y. Wang, R. Leon, M. Tentzeris, "Thermal effects on a passive wireless antenna sensor for strain and crack sensing," Proceedings of SPIE, Sensor and Smart Structures Technologies for Civil, Mechanical and Aerospace Systems, San Diego, CA, March 11-15, 2012.

27. V. Lakafosis, R. Vyas, V. Mukala, A. Traille, M. Tentzeris, "Wireless sensor network nodes for RTLS, biomonitoring, and authentication applications," *Antennas and Propagation (EUCAP), 2012 6th European Conference on* , vol., no., pp.62-63, 26-30 March 2012.

28. H. Lee, G. Shaker, V. Lakafosis, R. Vyas, T. Thai, S. Kim, X. Yi, Y. Wang, M. Tentzeris, "Antenna-based “smart skin” sensors for sustainable, wireless sensor networks," *Industrial Technology (ICIT), 2012 IEEE International Conference on* , vol., no., pp.189-193, 19-21 March 2012.

29. X. Yi, C. Fang, J. Cooper, C. Cho, R. Vyas, Y. Wang, R. Leon, M. Tentzeris, "Strain sensing through a passive wireless sensor array." Proceeding of the Structures 2012 Congress, Chicago, Illinois, USA, March 29-31, 2012.

30. M. Tentzeris, R. Vyas, V. Lakafosis, A. Traille, H. Lee, E. Gebara, M. Marroncelli, "Inkjet-printed RFIDs for wireless sensing and anti-counterfeiting," *Antennas and Propagation (EUCAP), 2012 6th European Conference on* , vol., no., pp.3481-3482,26-30 March2012.

31. R. Vyas, H. Nishimoto, M. Tentzeris, Y. Kawahara, T. Asami, "A battery-less, energy harvesting device for long range scavenging of wireless power from terrestrial TV broadcasts," *Microwave Symposium Digest (MTT), 2012 IEEE MTT-S International* , vol., no., pp.1-3, 17-22 June 2012.

32. R. Vyas, B. Cook, Y. Kawahara, M. Tentzeris, "A self-sustaining, autonomous, wireless-sensor beacon powered from long-range, ambient, RF energy," *Microwave Symposium Digest (IMS), 2013 IEEE MTT-S International* , vol., no., pp.1,3, 2-7 June 2013.

33. Yoshihiro Kawahara, Xiaoying Bian, Ryo Shigeta, Rushi Vyas, Manos M. Tentzeris, and Tohru Asami. 2013. Power harvesting from microwave oven electromagnetic leakage. In *Proceedings of the 2013 ACM international joint conference on Pervasive and ubiquitous computing* (UbiComp '13). ACM, New York, NY, USA, 373-382.

34. R.Vyas et al., “*Harvesting Wireless Signals from Two-way Talk-Radios to Power Smart Meters and Displays*”, accepted to the IEEE International Microwave Symposium, Tampa, USA, June 2014.

REFERENCES

[1] Chad Skelton, "Knee-Mounted Device Generates Electricity While You Walk," Vancouver, 7 Feb 2008.

[2] Bob Holmes, "The Power Within," New Scientist, 25 August, 2007.

[3] W. Dargie, C. Poellabauer,.: John Wiley and Sons, 2010, pp. 168-183.

[4] Environmental Protection Agency. (2007, April) FACTSHEET: MANAGEMENT OF ELECTRONIC WASTE IN THE UNITED STATES. [Online]. http://www.epa.gov/osw/conserve/materials/ecycling/docs/fact7-08.pdf

[5] CBC News. (2008, April) Making Sense of E-Waste. News Report.

[6] Charles A. Harper,.: Mc Graw-Hill, 2003.

[7] A. M. Bernardes, D. C. R. Espinosa, J. A. S. Tenorio, "Recycling of batteries: a review of current processes and technologies," *Journal of Power Sources*, vol. 130, no. 1-2, pp. 291-298, December 2003.

[8] EnviroCanada, "E-Waste Statistics," Technical Report 2008.

[9] L. Yang, A. Rida, R. Vyas, and M. Tentzeris, "RFID Tag and RF Structures on a Paper Substrate Using Inkjet-Printing Technology," *IEEE Transaction on Microwave Theory and Techniques*, pp. 2894-2901, Dec 2007.

[10] R. Vyas, V. Lakafosis, A. Rida, N. Chaisilwattana, S. Travis, J. Pan, M. Tentzeris, "Paper Based RFID-Enabled Wireless Platforms for Sensing Applications," *IEEE Transactions on Microwave Theory and Techniques*, vol. 57, no. 5, pp. 1370-1382, May 2009.

[11] A. Rida, M. Tentzeris, S. Nikolaou, "Design of low cost microstrip antenna arrays for mm-Wave applications," in *Antennas and Propagation (APSURSI), 2011 IEEE International Symposium on*, Spokane, USA, 2011, pp. 2071-2073.

[12] G.Shaker, A. Rida, S. Safavi-Naeini, M. Tentzeris, S. Nikolaou, "Inkjet printing of UWB antennas on paper based substrates," in *Antennas and Propagation (EUCAP), Proceedings of the 5th European Conference on*, Rome, Italy, 2011, pp. 3001-3004.

[13] A.G. Drachmann, "Heron's Windmill," *Centaurus*, vol. 7, pp. 145-151, 1961.

[14] Global Wind Energy Council, "Annual Installed Global Capacity 1996-2011," Technical Report 2011.

[15] D. Howey, A. Bansal, A. Holmes, "Design and performance of a cm-scale shrouded wind turbine for energy harvesting," *Smart Materials and Structures*, vol. 20, pp. 1-12, 2011.

[16] S. Ju, S. H. Chae, Y. Choi, S. Jun, S. M. Park, S. Lee, H. W. Lee, and C.-H. Ji, "Low Frequency Vibration Energy Harvester using MSMA/PZT Laminate Structure and Ball Magnet," in *PowerMEMS*, Atlanta, December 2012.

[17] D. Hoffmann, A. Willmann, B. Folkmer, Y. Manoli, "Energy Harvesting for High Speed Sensor Telemetry," in *IEEE PowerMEMS*, Atlanta, USA, 2012.

[18] L. Minh, M. Hara, H. Kuwano, "Miniaturized Multi-beam (K,Na)NbO3-based Energy Harvester," in *PowerMEMS*, Atlanta, December 2012.

[19] N. Besse, A. Quintero, D. Briand, P. Janphuang, R. Lockhart, J. Ruan, and N. Rooij, "PZT-based Energy Harvesters on Plastic Foil optimized though Theoretical Modeling and Fabrication

Improvements," in *IEEE PowerMEMS*, Atlanta, 2012.

[20] M. Tentzeris, L. Yang G. Orecchini and L. Roselli, "Smart Shoe": An autonomous inkjet-printed RFID system scavenging walking energy," in *IEEE International Symposium on Antennas and Propagation (APSURSI)*, Spokane, Washington, 3-8 July 2011, pp. 1417-1420.

[21] C. Kendall, J. Paradiso, N. Gershenfeld J. Kymissis, "Parasitic power harvesting in shoes," in *Second International Symposium on Wearable Computers*, 19-20 October 1998, pp. 132-139.

[22] S. Ravindran, M. Kroener, P. Woias, "A Standalone Pyroelectric Harvester for Thermal Energy Harvesting," in *PowerMEMS*, Atlanta, December 2012.

[23] M. Raju, M. Grazier, "ULP Meets Energy Harvesting: A game-changing combination for Designers," Texas Instruments, White Paper April 2010.

[24] K. Lin, J. Yu, J. Hsu, S. Zahedi, D. Lee, J. Friedman, A. Kansal, V. Raghunathan, M. Srivastava, "Heliomote: enabling long-lived sensor networks through solar energy harvesting," in *ACM Proceedings of the 3rd international conference on Embedded net*, San Diego, 2005, pp. 309-309.

[25] V. Raghunathan, A. Kansal, J. Hsu, J. Friedman, M. Srivastava, "Design considerations for solar energy harvesting wireless embedded systems," *Proceedings of the 4th international symposium on Information processing in sensor networks, IEEE Press*, vol. 64, 2007.

[26] M. Gorlatova, P. Kinget, I. Kymissis, D. Rubenstein, X. Wang, and G. Zussman, "Energy harvesting active networked tags (EnHANTs) for ubiquitous object networking," in *Wireless Communications, IEEE*, 2011, pp. 18-25.

[27] D. Schneider, "A Critical Look at Wireless Power ," IEEE Spectrum, 2010.

[28] NEC corporation, "Development of wireless power suply technology by magnetic induction from fluorescent tube," press release (In Japanese) 2006.

[29] A. Kurs, A. Karalis, R. Moffatt, J.D.Joannopoulos, P.Fisher, M. Soljacic, "Wireless power transfer via strongly coupled magnetic resonances," *Science*, vol. 317, no. 5384, pp. 83-86, 2007.

[30] A. Sample, D. Meyer, J. Smith, "Analysis, Experimental Results, and Range Adaptation of Magnetically Coupled Resonators for Wireless Power Transfer," in *IEEE Transactions on Industrial Electronics*, 2008, pp. 544-554.

[31] K. Finkenzeller, *RFID Handbook: Fundamentals and Applications in Contactless Smart Cards and Identification*.: John Wiley & Sons, Ltd., 2003.

[32] P. Glaser, "Power from the Sun: Its Future," *Science*, vol. 22, pp. 857-861, November 1968.

[33] U. Karthaus, M. Fischer, "Fully integrated passive UHF RFID transponder IC with 16.7-μW minimum RF input power," *Solid-State Circuits, IEEE Journal of*, vol. 32, no. 10, pp. 1602-1608, October 2003.

[34] A.P. Sample, D.J. Yeager, P.S. Powledge, and J.R. Smith, "Design of a Passively-Powered, Programmable Sensing Platform for UHF RFID Systems," in *IEEE International Conference on RFID*, March 2007, pp. 149-156.

[35] C. Occhiuzzi, A. Rida, G. Marrocco, and M. Tentzeris, "RFID Passive Gas Sensor Integrating Carbon Nanotubes," *Microwave Theory and Techniques, IEEE Transactions on*, vol. 59, no. 10, pp. 2674-2684, October 2011.

[36] C. Valenta, P. Graf, M. Trotter, G. Koo, and G. Durgin, "High-Voltage-Environment Backscatter-Channel Measurements at 5.8 GHz," *Antennas and Propagation Magazine, IEEE*, vol. 54, no. 4, pp. 231-240, August 2011.

[37] Powercast Corporation. (2012, April) RF Energy Harvesting and Wireless Power. [Online].

http://www.powercastco.com/PDF/powercast-overview.pdf

[38] R. Gutmann, J. Borrego, "Solar power satellite rectenna design study: Directional receiving elements and parallel-series combining analysis," Rensselaer Polytechnic Inst. Dept. of Electrical and Systems Engineering, Troy, NY (USA), Technical Report December 1978.

[39] A. Sample, J. Smith, "Experimental results with two wireless power transfer systems," in *Radio and Wireless Symposium,RWS '09. IEEE*, 2009, pp. 16-19.

[40] Rebecca Renner, "Do perfluoropolymers biodegrade into PFOA?," *Environmental Science and Technology*, pp. 648-650, February 2008.

[41] Asahi Glass Company Ltd., "Solution for RCC for High Frequency Circuit Board (Technical data)," Chiyoda, Japan, Technical report November 2005.

[42] G.Zou, H.Gronqvist, P.Starski, J.Liu, "Characterization of Liquid Crystal polymer for High Frequency System on a Package Applications," *IEEE Transaction Advanced Packaging*, pp. 503-508, 2002.

[43] A. Rida, R. Vyas, and M. Tentzeris L. Yang, "RFID Tag and RF Structures on a Paper Substrate Using Inkjet-Printing Technology," *IEEE Transaction on Microwave Theory and Techniques*, pp. 2894-2901, Dec 2007.

[44] H. Gronqvist, P. Starski, and J. Liu G. Zou, "Characterization of liquid crystal polymer for high frequency system-in-a-package applications," in *Proc. IEEE 8th International Advanced Packaging Material Symposium*, March 2002, pp. 337-341.

[45] H.Gronqvist, P.Starski, J.Liu G.Zou, "Characterization of Liquid Crystal polymer for High Frequency System on a Package Applications," *IEEE Transaction Advanced Packaging*, pp. 503-508, 2002.

[46] R. Vyas, V. Lakafosis, H. Lee, G. Shaker, L. Yang, G. Orecchini, A. Traille, M. Tentzeris, L. Roselli, "Inkjet Printed, Self Powered, Wireless Sensors for Environmental, Gas and Authentication Based Sensing," *IEEE Sensors Journal*, no. 99, 2011.

[47] LPKF Laser and Electronics. (1989) LPKF ProtoLaser S Datasheet. [Online]. http://www.lpkf.com/products/rapid-pcb-prototyping/laser-circuit-structuring/laser-structuring-printed-circuit-boards.htm

[48] Rogers Corp., "Ultralam 3000- Liquid Crystal Polymer Circuit Material," Datasheet 2003.

[49] Fujifilm USA Dimatix Inc., "Dimatix DMP 28XX Data Manual," Santa Clara, CA, 2008.

[50] A. Rida, L. Yang, R. Vyas, M. Tentzeris, "Conductive Inkjet-Printed Antennas on Flexible Low-Cost Paper-Based Substrates for RFID and WSN Applications," in *IEEE Antenna and Propagation Magazine*, 2009, pp. pg 13-23.

[51] A. Rida, L. Yang, R. Vyas, S. Bhattacharya, M. Tentzeris, "Design and Integration of inkjet-printed Paper-Based UHF Components for RFID and Ubiquitous Sensing Applications," in *IEEE European Union Microwave Conference*, 2007.

[52] L. Yang, A. Rida, R. Vyas, M. Tentzeris, "RFID Tag and RF Structures on a Paper Substrate Using Inkjet-Printing Technology," *IEEE Transactions on Microwave Theory and Techniques*, vol. 55, no. 12, pp. 2894-2901, December 2007.

[53] L. Yang, S. Basat, A. Rida, "Design and development of novel miniaturized UHF RFID tags on ultra-low-cost paper-based substrates," in *IEEE Asia Pacific Microwave Conference*, December 2006, pp. 1493-1496.

[54] R. Vyas, A. Rida, L. Yang, M.M Tentzeris, "Design, Integration and Characterization of a Novel Paper Based Wireless Sensor Module," in *IEEE International Microwave Symposium*, Atlanta, June 2008, pp. 1305-1308.

[55] A. Rida, R. Vyas, S. Basat,A. Ferrer-Vidal, L. Yang, S. Bhattacharya, M. Tentzeris , "Paper Based Ultra-Low-Integrated RFID Tags for Sensing and Tracking Applications," in *IEEE Electronic Components and Technology Conference (ECTC)*, Reno, 2007, pp. 1977-1980.

[56] M. Tentzeris, L. Yang, A. Rida, A. Traille, R. Vyas, T. Wu, "Inkjet-Printed RFID Tags on Paper-based Substrates for UHF "Cognitive Intelligence" Applications," in *IEEE Personal Indoor Mobile Radio Communication International Symposium*, September 2007, pp. 1-4.

[57] M. Tentzeris, L. Yang, A. Rida, A. Traille, R. Vyas, T. Wu, "RFID's on Paper using Inkjet-Printing Technology: Is it the first step for UHF Ubiquitous Cognitive Intelligence and Global Tracking?," in *RFID Eurasia Conference*, September 2007, pp. 1-4.

[58] M. Tentzeris, "Novel Paper-based Inkjet Printed Antennas and Wireless Sensor Modules," in *IEEE COMCAS*, May 2008, pp. 1-8.

[59] Microchip, "TC1047/TC1047A Temperature to Voltage Converter," Datasheet 2005.

[60] EPCglobal, "EPC radio-frequency identity protocols Class-1 Generation-2 UHF RFID air interface version 1.0.9," Standard 2005.

[61] R.B. Marks, "A multiline method of network analyzer calibration," *IEEE Trans. Microwave Theory Tech.*, vol. 39, no. 7, pp. 1205-1215, July 1991.

[62] Microchip, "RFPIC 12F675K/675F/675H Datasheet," Datasheet 2003.

[63] J. Peatman, *Embedded Design with the PIC18F452 Microcontroller*. Pearson, NJ: Upper Saddle River, 2003.

[64] K. Kurokawa, "Power Waves and the Scattering Matrix ," *IEEE Transactions on Microwave Theory and Techniques* , vol. MTT-13, no. 3, pp. 194-202, March 1965.

[65] S. Cripps,. Norwood, MA, USA: Artech House, 1999, pp. 1-32.

[66] Panasonic. (2005) CR2032 Panasonic Magnesium Lithium Coin Batteries Specifications. [Online]. http://www.panasonic.com/industrial/includes/pdf/Panasonic_Lithium_CR2032_CR2330.pdf

[67] S.Nikolaou, G.E.Ponchak, Y.-S.Kim, J.Papapolymerou and M.M.Tentzeris B.Kim, "A Curvature CPW-fed Ultra-wideband Monopole Antenna on Liquid Crystal Polymer Substrate Using Flexible Characteristics ," in *Antenna and Propagation Society International Symposium on* , Albuquerque, NM, July 2006, pp. 1667-1670.

[68] Jong K. Park, and Jung N. Lee Seong H. Lee, "BA novel CPW-fed ultra-wideband antenna design," *Microwave Optics Letters*, vol. 44, no. 5, pp. 393-396, March 2005.

[69] H.W.Ott, *Noise Reductaion Techniques in Electronic Systems*, 2nd ed. New York, USA: Wiley, 1988.

[70] inLogic. (2012) Passive vs. Active RFID Comparison. [Online]. http://www.inlogic.com/rfid/passive_vs_active.aspx

[71] Texas Instruments, "eZ430-RF2500-SEH Solar Energy Harvesting Development Tool," Texas Instruments, User Guide 2009.

[72] Cymbet Corporation. (2012) CBC-Eval-09 EP Universal Energy Harvester Evaluation Kit. [Online]. http://www.cymbet.com/pdfs/DS-72-13.pdf

[73] Texas Instruments, "CC1000 Single Chip Very Low Power RF Transceiver," Datasheet 2008.

[74] R. Vyas, V. Lakafosis, M. Tentzeris, "Wireless Remote Localization System Utilizing Ambient RF/Solar Power Scavenging RFID Tags," in *IEEE International Microwave Symposium*, Anaheim CA, USA, May 2010, pp. 1764-1767.

[75] R. Vyas, V. Lakafosis, M. Tentzeris, "Enabling Localization in WSNs with Solar-Powered End

Devices," in *IEEE conference on Sensor Networks, Ubiquitous and Trustworthy Computing (SUTC)*, San Francisco, 2010, pp. 155-160.

[76] R. Vyas, V. Lakafosis, M. Tentzeris, "Design and Characterization of a Novel Battery-less, Solar Powered Wireless Tag for Enhanced-range Remote Tracking applications," in *IEEE European Union Microwave Conference (EuMW)*, November 2009, pp. 169-172.

[77] Ixsys, "Clare CPC 1832 Solar Cel," Datasheet 2008.

[78] C.Balanis, *Antenna Theory*, 2nd ed.: Wiley, 1997, ch. 11, pp. 569-588.

[79] Mastech, "LX1330 B: Dr. Meter Digital Illuminance/Light Meter 0-20,000 Lux Meter," Datasheet 2008.

[80] Ecological Software Solutions LLC, "GTAthena Localization Version 1.11," Hegymagas, Hungary, 2008.

[81] J.Seybold,. Hoboken NJ: Wiley, 2005 , 2005, pp. 111-133, 163-179.

[82] T.Kvaksrud, "Range Measurements in an Open Field Environment.," Texas Instruments, Design Note DN018 2008.

[83] NARDA, "SRM 3000 Selective Radiation Meter Datasheet.," Datasheet 2012.

[84] David Sparano. What Exactly is 8-VSB Anyway?. [Online]. http://www.arrl.org/files/file/Technology/TV_Channels/8_Bit_VSB.pdf

[85] Agilent. (2005) DTV ISDB OFDM Project Example. [Online]. http://cp.literature.agilent.com/litweb/pdf/ads2005a/dtv/dtv124.html

[86] David Sparano. What Exactly is 8-VSB Anyway? [Online]. http://www.arrl.org/files/file/Technology/TV_Channels/8_Bit_VSB.pdf

[87] National Instruments. (2012, January) Spectral Measurements Part 1. [Online]. www.ni.com

[88] D. Pozar, *Microwave Engineering*.: Wiley, 2005.

[89] NHK Japan Bradcasting Corporation. (1999) Outline of the Specification for ISDB-T. [Online]. http://www.nhk.or.jp/strl/open99/de-2/shosai-e.html

[90] B. Pan, J. Laskar, M. M. Tentzeris RongLin Li, "A compact broadband planar antenna for GPS, DCS-1800, IMT-2000, and WLAN applications ," *IEEE Antennas and Wireless Propagation Letters*, vol. 6, pp. 25-27, 2007.

[91] D. Isbell R. Duhamel, "Broadband Logarithmically Periodic Antenna Structures," *IRE International Convention Record*, pp. 119-128, 1957.

[92] R.Carrel, "ANALYSIS AND DESIGN OF THE LOG-PERIODIC DIPOLE ANTENNA," Illinois Univrsity at Urbana Electrical Engineering Research Lab, Urbana, Technical 1961.

[93] C.Balanis, *Antenna Theory*.: Wiley, 1997, ch. 11, pp. 569-588.

[94] U. Karthaus and M. Fischer, "Fully integrated passive UHF RFID transponder IC with 16.7-μW minimum RF input power," *Solid-State Circuits, IEEE Journal of* , vol. 32, no. 10, pp. 1602-1608, October 2003.

[95] G. DeVita, G. Iannaccone, "Design criteria for the RF section of UHF and microwave passive RFID transponders," *Microwave Theory and Techniques, IEEE Transactions on*, vol. 53, no. 9, pp. 2978-2990, Sept. 2005.

[96] G. De Vita and G. Iannaccone, "Design criteria for the RF section of UHF and microwave passive RFID transponders," *Microwave Theory and Techniques, IEEE Transactions on*, vol. 53, no. 9, pp. 2978- 2990, , Sept. 2005.

[97] P. Pannier, J. Gaubert E. Bergeret, "Optimization of UHF voltage multiplier circuit for RFID application," in *IEEE Transactions on Circuits and Systems II*, Dec 2005, pp. 13-15.

[98] P. Pannier, J.Gaubert, J. Gaultier E. Bergeret, "Modeling and Design of CMOS UHF Voltage Multiplier for RFID in an EEPROM Compatible Process," *Circuits and Systems II: Express Briefs, IEEE Transactions on*, vol. 10, pp. 833-837, Oct 2007.

[99] R.Vyas, H.Nishimoto, Y.Kawahara, T.Asami, M. Tentzeris, "A battery-less, energy harvesting device for long range scavenging of wireless power from terrestrial TV broadcasts," in *IEEE MTT Microwave Symposium Digest (MTT)*, Montreal, Canada, July 2012, pp. 1-3.

[100] R.Vyas, B.Cook, B, Y.Kawahara, M. Tentzeris, "A self-sustaining, autonomous, wireless-sensor beacon powered from long-range, ambient, RF energy," in *IEEE MTT-S International Microwave Symposium Digest (IMS)*, Seattle, USA, 2-7 June 2013, pp. 1-3.

[101] B.Cook, Y. Kawahara, M.Tentzeris R.Vyas, "E-WEHP: A Batteryless Embedded Sensor-Platform Wirelessly Powered From Ambient Digital-TV Signals," *IEEE Transactions on Microwave Theory and Techniques*, vol. 61, no. 6, pp. 2491-2505, June 2013.

[102] Rohde and Schwarz, "ZVA-8 Vector Network Analyzer," User Guide 2006.

[103] H. Primer, "What exactly is ATSC," Technical Report 2009.

[104] Microchip Technologies Inc. (2009) PIC24F16KA102 Family Datasheet. [Online]. http://ww1.microchip.com/downloads/en/DeviceDoc/PIC24F16KA102_Family_datasheet_39927b.pdf

[105] Silicon Labs. (2012) SiM3C1xx High-Performance, Low-Power, 32-Bit Precision32™ MCU Family with up to 256 kB of Flash Datasheet. [Online]. http://www.silabs.com/Support%20Documents/TechnicalDocs/SiM3C1xx.pdf

[106] Texas Instruments. (2011, July) TI MSP430F2274 Mixed Signal Microcontroller Datasheet. [Online]. www.ti.com

[107] A. Dolgov, R. Zane, and Z. Popovic, "Power Management System for Online Low Power RF Energy Harvesting Optimization," *Circuits and Systems I: Regular Papers, IEEE Transactions on*, vol. 57, no. 7, pp. 1802-1811, July 2010.

[108] A.P. Sample, D.J. Yeager, P.S. Powledge, A.V. Mamishev, and J.R. Smith, "Design of an RFID-Based Battery-Free Programmable Sensing Platform," *Instrumentation and Measurement, IEEE Transactions on* , vol. 57, no. 11, pp. 2608-2615, Nov 2008.

[109] R. Vyas, V. Lakafosis, Z. Konstas, and M.M. Tentzeris, "Design and characterization of a novel battery-less, solar powered wireless tag for enhanced-range remote tracking applications," in *Microwave Conference, 2009. EuMC 2009. European*, 2009, pp. 169-172.

[110] K. V S Rao, R. Martinez, and S.F. Lam P.V. Nikitin, "Sensitivity and Impedance Measurements of UHF RFID Chips ," *IEEE Transactions on Microwave Theory and Techniques*, vol. 57, no. 5, pp. 1297-1302, May 2009.

[111] H. Reinisch et al., "An Electro-Magnetic Energy Harvesting System With 190 nW Idle Mode Power Consumption for a BAW Based Wireless Sensor Node," *IEEE Journal of Solid-State Circuits*, vol. 46, no. 7, pp. 1728-1741, July 2011.

[112] Jun Yin et al, "A System-on-Chip EPC Gen-2 Passive UHF RFID Tag With Embedded Temperature Sensor," *IEEE Journal of Solid-State Circuits*, vol. 45, no. 11, pp. 2404-2420, Nov 2010.

[113] D. Yeager et al, "A 9 uA, Addressable Gen2 Sensor Tag for Biosignal Acquisition," *IEEE Journal of Solid-State Circuits*, vol. 45, no. 10, pp. 2198-2209, October 2010.

[114] A.S. Boaventura, N.B. Carvalho, "Maximizing DC power in energy harvesting circuits using multisine

excitation," in *IEEE International Microwave Symposium Digest (MTT-S)*, 5-10 June, 2011, pp. 1-4.

[115] P. G. Steffes, A.J. Petrin, "Study of spectrum usage and potential interference to passive remote sensing activities in the 4.5 cm and 21 cm bands," in *International Proceedings of Geoscience and Remote Sensing Symposium IGARSS* , 2004, p. vol 3.

[116] Allen Petrin, "MAXIMIZING THE UTILITY OF RADIO SPECTRUM: BROADBAND SPECTRUM MEASUREMENTS AND OCCUPANCY MODEL FOR USE BY COGNITIVE RADIO," Georgia Institute of Technology, Atlanta, Ph.D. Thesis TK174.G45x P4465c, 1 Jan 2005.

[117] M.S. Trotter, J.D. Griffin, G.D Durgin, "Power-optimized waveforms for improving the range and reliability of RFID systems," in *IEEE International Conference on RFID*, 27-28 April 2009, pp. 80-87.

[118] Matsumoto, H., "Research on solar power satellites and microwave power transmission in Japan," *Microwave Magazine, IEEE*, vol. 3, no. 4, pp. 36-45, Dec 2022.

[119] Epoxy Technology, "H20E Epo-Tek Technical Datasheet," Datasheet February 2010.

[120] G. Zou, H. Gronqvist, P. Starski, and J. Liu, "Characterization of liquid crystal polymer for high frequency system-in-a-package applications," in *Proc. IEEE 8th International Advanced Packaging Material Symposium*, March 2002, pp. 337-341.

[121] R. Vyas, V. Lakafosis, T. Wu, Y. Kawahara, M. Tentzeris, "Near-perpetual operated solar and RF powered autonomous sensing systems," in *IEEE Asia Pacific Microwave Conference (APMC)*, November 2009, pp. 2241-2243.

[122] Z. Konstas, A. Rida, R. Vyas, K. Katsibas, Z. Uzunoglu, M. Tentzeris, "A novel “Green” inkjet-printed Z-shaped monopole antenna for RFID applications," in *IEEE Antennas and Propagation EuCAP*, Berlin, Germany, 2009, pp. 2340-2343.

[123] H. Reinisch et al., "An Electro-Magnetic Energy Harvesting System With 190 nW Idle Mode Power Consumption for a BAW Based Wireless Sensor Node," *IEEE Journal of Solid-State Circuits* , vol. 46, no. 7, pp. 1728-1741, July 2011.

[124] Jun Yin et al., "A System-on-Chip EPC Gen-2 Passive UHF RFID Tag With Embedded Temperature Sensor," *IEEE Journal of Solid-State Circuits*, vol. 45, no. 11, pp. 2404-2420, Nov 2010.

[125] D. Yeager et al., "A 9 uA, Addressable Gen2 Sensor Tag for Biosignal Acquisition," *IEEE Journal of Solid-State Circuits*, vol. 45, no. 10, pp. 2198-2209, October 2010.

[126] Powercast Corporation. (2012, April) RF Energy Harvesting and Wireless Power. [Online]. http://www.powercastco.com/PDF/powercast-overview.pdf

[127] K. Finkenzeller,.: John Wiley & Sons, Ltd., 2003, ch. 9, p. 271.

[128] EPC Global, "EPC Radio-Frequency Indentification Protocols Class-1 Generatio-2 UHF RFID EPC Protocol for Communications at 860-960 MHz," EPC Global Inc., version 1.2.0, 23 October, 2008.